



University Carlos III of Madrid  
Aerospace Engineering

## Characterization and improvement of a hybrid chemical rocket

Author: Lara Cristina Sánchez Hernández

Director: Mario Merino Martínez

Leganés, Madrid  
2017



# Abstract

The concerning project addresses a theoretical and practical analysis of an improved small hybrid rocket prototype. The main characteristics of the motor are: a fuel-oxidizer combination consisting of a hollow cylinder of PMMA and pure oxygen injected at high pressure (3-4 bar), and a pure convergent nozzle for which several values of the throat diameter were be tested.

The main goal of the project was to characterize the rocket performance. In order to do so, first it was necessary to perform some physical improvements such as the inclusion of a pressure transducer for the estimation of the oxygen flow rate, as well as the redesign of the supporting structure and the amelioration of the data acquisition system for the obtaining of meaningful thrust readings. Moreover, a theoretical one-dimensional model was develop to contrast the empirical data and ensure its validity. Finally, three parametric studies were performed for which several experiments with different combinations of nozzle throat diameter, fuel cartridge length and oxygen tank pressure setting were carried out.

The relevance of this project is significant given that this was the first phase of this prototype in which meaningful results were obtained. From the experimental phase, it was possible to conclude that the operation of the device was highly transient and that the feeding oxygen orifice did not reach sonic conditions during operation against the expectations. Additionally, the correlation between the theoretical model and the empirical data showed an acceptable fitting, and although the lack of chamber temperature measurement was an inconvenient, it was possible to estimate the said parameter from the previous results. Finally, with respect to the parametric studies, it was concluded that: the low oxygen pressure ultimately caused that the reduction of the fuel cartridge length had no effect on the rocket performance; the largest nozzle (6mm throat diameter) coincided with the critical pressure ratio, and consequently, the smallest nozzle (4mm throat diameter) was clearly choked, although the increase in the rocket thrust was not very significant; the increase of the tank pressure was the most efficient way to increase the performance of the motor. Ultimately, it was concluded that a considerably higher thrust force could be achieved by performing future physical improvements to the device.

**Keywords:** Hybrid rocket, theoretical analysis, experimental analysis, parametric study, performance, PMMA-Oxygen reaction.

# Acknowledgments

First of all, I would like to thank my family for their constant love and support. To my father, who always stood by my side and helped me to accomplish my goals. Thank you for all your affection and your understanding.

Special thanks to Mario Merino, for allowing me to carry out this project under his direction. I appreciate your guidance and your encouragement, it has been a pleasure to work with you.

Also, thanks to Carlos Cobos for his indispensable assistance in the project, as well as to Marco Raiola and Jaume Navarro for kindly offering their expert opinions when requested. Moreover, I would like to show my gratitude to the rest of professors of the Aerospace Engineering Department for transmitting their passion to the students, and also to the University Carlos III of Madrid for allowing me to make use of its facilities for this project.

Thanks to my friends of Aerospace Engineering, with whom I have shared moments of joy and satisfaction, but also moments of frustration and stress. Your help has been essential in more than one occasion, and I only hope to find mates like you in the future.

Finally, thanks to my closest friends, Diego and Alberto, for making me laugh and putting up with me. You are the best friends I can have and I wish you will be forever.



# Contents

<b>Abstract</b>	<b>i</b>
<b>Acknowledgments</b>	<b>ii</b>
<b>Table of Contents</b>	<b>iii</b>
<b>List of Figures</b>	<b>v</b>
<b>List of Tables</b>	<b>vii</b>
<b>1 Introduction</b>	<b>1</b>
1.1 Objectives of this project . . . . .	1
1.2 Structure of the report . . . . .	2
<b>2 State of the Art</b>	<b>3</b>
2.1 History and applications of hybrid rockets . . . . .	3
2.2 Types of rocket motors . . . . .	4
2.3 Chemical rockets . . . . .	5
2.4 Previous evolution of the UC3M hybrid rocket prototype . . . . .	7
2.5 Regulatory framework . . . . .	7
<b>3 Theoretical background</b>	<b>9</b>
3.1 Hybrid rocket performance: simplified regression rate model . . . . .	9
3.2 One-dimensional model . . . . .	10
3.2.1 Fuel mass flow rate . . . . .	10
3.2.2 Oxygen mass flow rate . . . . .	10
3.2.3 Total mass flow rate . . . . .	13
3.2.4 Theoretical thrust . . . . .	16
<b>4 Experimental setup</b>	<b>17</b>
4.1 Design requirements . . . . .	17
4.2 Description of the blocks and parts . . . . .	18
4.2.1 Cold block . . . . .	18
4.2.2 Propellant block . . . . .	20
4.2.3 Hot block . . . . .	21
4.2.4 Rocket assembly . . . . .	24
4.3 Nozzle design . . . . .	25
4.4 Machining of parts . . . . .	27
4.5 Support Structure . . . . .	28

4.6	Diagnosis system . . . . .	28
4.6.1	Thrust measurement: load cell . . . . .	29
4.6.2	Oxygen line pressure drop measurement: pressure transducer . . . . .	30
4.7	Electric and electronic systems . . . . .	32
4.7.1	Load cell and transducer electronic circuit. Analog Discovery 2 . . . . .	32
4.7.2	Electric circuit: glow plug . . . . .	34
<b>5</b>	<b>Experimental tests and results</b>	<b>35</b>
5.1	Sensors calibration and zero output voltage readings . . . . .	35
5.1.1	Sensors zero output voltage reading . . . . .	35
5.1.2	Load cell calibration . . . . .	37
5.2	First two trial firings . . . . .	37
5.3	Results of the subsequent monitored firings . . . . .	39
<b>6</b>	<b>Discussion of results</b>	<b>43</b>
6.1	Implementation procedure in Matlab software . . . . .	43
6.2	Correlation between experimental and theoretical results . . . . .	43
6.3	Parametric studies . . . . .	51
6.3.1	Fuel cartridge length . . . . .	51
6.3.2	Nozzle throat diameter . . . . .	52
6.3.3	Oxygen tank pressure setting . . . . .	53
6.4	Analysis of the regression rate . . . . .	53
<b>7</b>	<b>Conclusions and future work</b>	<b>55</b>
7.1	Conclusions . . . . .	55
7.2	Future work . . . . .	56
<b>8</b>	<b>Project budget and socioeconomic model</b>	<b>57</b>
8.1	Project budget . . . . .	57
8.2	Socioeconomic model . . . . .	57
	<b>Bibliography</b>	<b>60</b>
	<b>Appendices</b>	<b>a</b>
	Part plans . . . . .	a
	Check list . . . . .	l
	Load cell specifications . . . . .	n
	Pressure transducer specifications . . . . .	r

# List of Figures

2.1	Launch of Titan II carrying Gemini spacecraft . . . . .	3
2.2	VSS being carried by its mother ship, the VMS Eve . . . . .	4
2.3	Solid- and liquid-propellant rocket motors . . . . .	5
2.4	Hybrid rocket schematics . . . . .	6
2.5	UC3M prototype after the construction phase . . . . .	7
2.6	UC3M prototype after the first improvement phase . . . . .	8
3.1	Sketch of the combustion boundary layer . . . . .	9
3.2	T-pneumatic connexion . . . . .	11
3.3	Sketch of $\dot{m}_{ox}$ Vs. $P_c$ graph as given by the calibrated hole . . . . .	12
3.4	Sketch of $\dot{m}_{ox}$ Vs. $P_c$ graph as given by the nozzle throat . . . . .	15
4.1	Complete rocket system . . . . .	17
4.2	Thruster assembly CAD view: cold block, propellant block and hot block . . . . .	18
4.3	Exploded CAD view of the thruster assembly . . . . .	19
4.4	Piece 1, back view . . . . .	19
4.5	Piece 2 CAD views . . . . .	19
4.6	Real picture of Piece 1 . . . . .	20
4.7	Propellant block: combustion chamber and confined air . . . . .	20
4.8	Sets of propellant tubes . . . . .	21
4.9	Exploded view of the hot block subassembly . . . . .	21
4.10	Graphite piece relative position to Piece 3 . . . . .	22
4.11	Piece 3 back view . . . . .	22
4.12	Piece 4 CAD views . . . . .	22
4.13	Piece 5 CAD views . . . . .	23
4.14	Nozzle (6mm throat diameter) CAD views . . . . .	23
4.15	Comparison of nozzle throat diameters . . . . .	23
4.16	Piece 6 CAD views . . . . .	24
4.17	Real picture of the thruster stack . . . . .	24
4.18	Graphite gaskets . . . . .	24
4.19	$\dot{m}_T$ Vs. $D_t$ for minimum chamber pressure ( $P_{amb}$ ) . . . . .	26
4.20	$\dot{m}_T$ Vs. $D_t$ for 3bar chamber pressure . . . . .	27
4.21	Rear view of the battering ram structure . . . . .	28
4.22	Hooks, steel cables and aluminum profile arrangement . . . . .	29
4.23	Sensors location in the empty structure . . . . .	29
4.24	Load cell location relative to the thruster assembly . . . . .	30

4.25	Characteristic line of the load cell according to the datasheet specifications . . . . .	30
4.26	Gas flow regulation system . . . . .	31
4.27	Pressure transducer . . . . .	31
4.28	Characteristic line of the pressure transducer . . . . .	32
4.29	Sketch of the electronic connexions in the lab room side . . . . .	32
4.30	Real electronic connexions in the lab room side . . . . .	33
4.31	Waveforms workspace . . . . .	33
5.1	Setup of rocket position relative to the load cell . . . . .	36
5.2	Sketch of absolute force, contact force and actual (true) thrust . . . . .	36
5.3	Load cell calibration test voltage reading . . . . .	37
5.4	Comparison between the load cell characteristic lines from the calibration and from the specifications . . . . .	38
5.5	Transducer pressure readings and load cell thrust readings . . . . .	41
5.6	Burning time calculation . . . . .	42
6.1	Theoretical oxygen mass flow solution for Experiment 1 . . . . .	44
6.2	Theoretical and experimental thrust force for Experiment 1 . . . . .	45
6.3	Legend for the following graphs of the theoretical oxygen mass flow . . . . .	46
6.4	Experiment 2 results . . . . .	46
6.5	Experiment 3 results . . . . .	47
6.6	Experiment 4 results . . . . .	47
6.7	Experiment 5 results . . . . .	47
6.8	Experiment 6 results . . . . .	48
6.9	Experiment 7 results . . . . .	48
6.10	Experiment 8 results . . . . .	48
6.11	New and used propellant tubes . . . . .	51
6.12	Results of the regression model . . . . .	54

# List of Tables

4.1	PMMA tubes inner and outer diameter. . . . .	20
4.2	PMMA tubes length. . . . .	21
5.1	Configuration and atmospheric data for each experiment . . . . .	39
6.1	Results obtained from the $\dot{m}_{ox}$ Vs. $P_c$ graph . . . . .	49
6.2	Results obtained from the $F$ Vs. $P_c$ graph . . . . .	49
6.3	Fuel mass flow and O/F ratio. . . . .	51
6.4	Regression rate and oxygen flux. . . . .	54
8.1	Project budget . . . . .	57

# 1 Introduction

Hybrid rockets constitute a type of aerospace propulsion with great potential that shows multiple advantages over other, more common types of rocket motors. However, their complex modeling has prevented them to progress beyond the prototype project phase so far.

With the goal of achieving a better understanding of hybrid rockets, in the academic course of 2012-2013, the UC3M started the fabrication of a model, based on an similar project of Professor Emeritus Manuel Martínez Sánchez from Massachusetts Institute of Technology (MIT).

During the following courses, in Bachelor in Aerospace Engineering at UC3M, and in particular, in the Rocket Motors subject, a practical session addressing the rocket performance was introduced as part of the academic contents so that the students could obtain a closer insight of this type of motor.

A critical point in the evolution of this prototype took place in the past course, when a second project was developed for the improvement of some of the features of the device. However, up to this point, no successful characterization of the rocket could be obtained mainly due to difficulties associated to the collection of empirical data.

Therefore, the concerning project has arisen from the need of improving the actual device so as to obtain meaningful experimental figures and hence, finally achieve a basic understanding of hybrid rockets.

For the sake of clarification, before proceeding to the description of the individual objectives, a very brief introduction to the physical components of the rocket will be presented. The complete equipment of the rocket can be divided in several subsystems:

- Thruster stack: the rocket motor itself, divided in three blocks.
- Supporting structure.
- Diagnosis system: group of sensors in charge of providing empirical data.
- Pneumatic system: composed of three gas lines and pneumatic components to feed the rocket from the gas tanks.
- Electric and electronic system: in charge of the provision of power to the electrical components as well as the recording of the sensors output signal.

With this basic knowledge of the prototype, a proper definition of the individual objectives of the project can be presented.

## 1.1 Objectives of this project

In order to perform the aforementioned characterization of the rocket, it was essential to obtain the required experimental data. This was possible thanks to the introduction of some modifications in regard to the device itself, but also, its associated subsystems. On the other hand, a one-dimensional theoretical model was developed so as to contrast the practical data and ensure its validity. Finally, a parametric study of several aspects of the rocket motor was carried out with the aim of analyzing the rocket performance.

In regard to the physical modifications of the prototype with respect to the previous configuration, the objectives are:

- Design and construction of a new supporting structure to enable the measurement of thrust. The previous supporting structure, composed of a sliding platform, was thought to cause an excessive friction force that prevented the thruster stack from moving, and thus, obtaining any measurement of the thrust force.

- Installation of a diagnosis element (pressure transducer) in the oxygen gas line. The lessening of the existing uncertainty associated to the oxygen mass flow entering the motor was crucial for an accurate theoretical analysis.
- Installation of an upgraded data acquisition system given the need of recording the additional diagnostic. The multi-functional device Analog Discovery 2 would be used to this end.

With respect to the experimental procedure, the main goal is:

- Carrying out of several tests for different combinations of the three parameters involved in the parametric study: nozzle throat section, fuel cartridge length and oxygen tank pressure setting.

In relation to the theoretical model and the results discussion, the needs are:

- Definition of a theoretical expression for the rocket thrust force using the available empirical data and estimating the unknown parameters.
- Execution of a comparative analysis between the theoretical and empirical results to study how the characterization of the device adapts to the real prototype.

## 1.2 Structure of the report

The description of the development of this project has been structured in the following way.

After this introductory section, the State of the Art of hybrid rockets will be presented in Section 2. Apart from their motivation, characteristics, historical evolution and applications, this section will also enclose a brief insight of the transformation process of the prototype at the UC3M as well as the regulatory framework applied to experimental procedures in lab rooms.

Section 3 comprises the definition of the theoretical model that will be implemented numerically in Matlab software for the characterization of the device.

After that, an extensive description of the experimental set up will be explained in Section 4. The contents involve, among other minor topics, a description of: the pieces conforming thruster assembly, the configuration of the supporting structure, the nozzle design process, and the detailed electronic connexions of the diagnosis system.

Section 5, will follow with the explanation of the experimental procedure to run the tests, as well as the exhibition of the experimental results and their individual discussion.

In the next section, a brief narration of the numerical implementation of the problem will be included, followed by the juxtaposition of the theoretical and empirical results for each individual test. In the last part of this section, the parametric study will take place by means of a comparison of the experiments between them.

Section 7 will enclose the summary of the conclusions extracted from this project, as well as some suggestions for future work.

Finally, this report will end with the presentation of the project budget together with a brief socio-economical model of this hybrid rocket prototype in particular.

## 2 State of the Art

Rockets are based on the principle of jet propulsion, by which a reaction force, called thrust, is achieved from the ejection of matter, according to the Third Newton Law. Jet propulsion is further divided into air-breathing and rocket propulsion. In rocket motors, the reactants or gases used to produce the high-momentum-jet are stored inside the rocket, in contrast with air-breathing engines, in which the oxidizer is the atmospheric air. This characteristic allows rockets to be independent on the surrounding medium and therefore, be able to operate in outer space.

In the following section, a historical review of hybrid rockets will be introduced for a better understanding of the causes that lead to the invention of the different types of rockets.

### 2.1 History and applications of hybrid rockets

Preliminary forms of solid-propellant rockets are associated to the discovery of gunpowder around the year 2000 B.C, but it wasn't until the 13th century that the first use of a true solid rocket was reported. During the following centuries, these artifacts were mainly used in warfare and fireworks, with some remarkable improvements such as the invention of the first multi-staged rocket.

At the end of the 17th century, the scientific basis of rocketry were settled by Sir Isaac Newton (1642-1727) with the publication of his Three Laws of physical motion. The experiments with solid rockets for combat application continued during this period but controllability was still a pending subject of these devices.

The era of modern rocketry was marked by the work of Konstantin Tsiolkovsky (1857-1935), who in 1903, published his most famous work, "Research into Interplanetary Space by Means of Rocket Power". He wrote widely about human space travel, introducing the ideas of liquid propellant rocket engines, orbital space stations or colonization of the Solar System.

In 1915, the so called father of rocketry, Robert H. Goddard (1882-1945), began to perform multiple experiments on solid-propellant rockets, but he decided that liquid propellants would result in greater performances and safer fabrication and manipulation, so following the lead of Tsiolkovsky, in 1926, he achieved the first successful flight of a liquid-propellant rocket. For the next years, Goddard continued with his work on liquid rockets with great improvements such as a gyroscope system for flight control, payload compartments for instrumentation and parachute recovery systems.

At this point the first ideas of hybrid rockets started to take form. The first reporting of an hybrid rocket dates of 1933, when the use of liquid propellants was still in its initial phases. From this year to 1960 is considered the early history of hybrid rockets, characterized by a small number of research programs, focused on obtaining a basic understanding of their performance. Numerous fuel and oxidizer combinations were tested during this time, being the first successful flight a mixture of LOX (liquid oxygen) and rubber based fuel, achieved in 1951 by the Pacific Rocket Society's XDF-23 model. A major discovery of this and subsequent experiments was that the chamber pressure was proportional to the oxidizer flow rate but it was not dependent on the internal grain surface area exposed to the combustion, and hence, cracks in the grain did not involve serious risks (unlike in solid rockets).

Given the safer characteristics of hybrid rockets, during the 60's, the US Military forces and other US companies, such as United Technologies Corporation (UTC), started to show great interest in them. UTC, the developer of the Titan solid rocket booster, started to investigate the fundamentals of hybrid rockets.



Figure 2.1: Launch of Titan II carrying Gemini spacecraft [15]



Their design of the hybrid demonstrator in 1960 allowed to perform multiple experiments, which lead to important accomplishments such as the development of hybrid regression rate models, which in turn is what characterizes this period of time.

In the mid 60's a scaling process to reach large size rocket motors started to take place, with the most important projects being the UTC HTM series, the United Tech CSD and the LEX-02, all of them with dimensions of the order of 1m diameter and thrust forces of the order of 10 kN. Polybutadiene (PB) and nitrogen tetroxide ( $N_2O_4$ ) became of common use as solid fuel and oxidizer, respectively.

In 1981, the STARTSTRUCK company was created to develop the biggest hybrid sounding rocket at the time, the Dolphin, characterized by a length of 17m, a thrust of 155 kN and a PB-LOX fuel-oxidizer combination, which ended in a frustrated flight. Then, the company was renamed to AMROC, and continued with the design of large hybrid rockets ranging from 22kN to 1MN based on a LOX-HTPB(Hydroxyl-terminated polybutadiene) mixture. Several tests with a 333kN motor were successfully completed. Nonetheless, in the tests performed during 1993 and 1994, the 1MN motor constructed to be part of the AQUILA vehicle suffered from low-frequency instabilities and high-amplitude pressure oscillations as a result of an incomplete vaporization of the LOX at the entrance of the solid grain ports. This inconvenient ultimately led to the abandonment of the project.

In 1986, as a consequence of the Challenger disaster, NASA started to support hybrid rockets to replace the solid rocket boosters. Nevertheless, at this time the regression rate (radial velocity at which the fuel grain is consumed) was too low, and hence the needed thrust could not be achieved. Some experiments were performed trying to increase the regression rate by adding fuel additives (ammonium perchlorate ( $NH_4ClO_4$ ) and ammonium nitrate ( $NH_4NO_3$ )) or metallic particles (mainly Aluminum particles), and also by increasing the turbulence of the combustion through the strategical positioning of gas injectors. However, these measures did not prevent low-frequency instabilities from occurring either.



Figure 2.2: VSS being carried by its mother ship, the VMS Eve [16]

In the last years, the use of hybrid rockets has been oriented mainly towards space tourism. The first success was the SpaceShipOne(SS1), a suborbital spaceplane, air-launched by its jet mother ship, the White Knight. The SS1 motor used a  $HTPB - N_2O$  fuel-oxidizer rocket to reach a 100km height. In 2004, after achieving two consecutive successful flights, the project won the US\$10million prize contest organized by the Ansari brothers, the X-Prize.

That same year, the Virgin Galactic Company was founded by Richard Branson with the goal of being the first commercial spaceline carrying passengers into space. They continued to work with the SpaceShipTwo(SS2), also named Virgin Space Ship (VSS) Enterprise, and its mother ship the White Knight Two, also called Virgin Mother Ship (VMS) Eve. Several successful test flights were achieved before the fatal accident on 31st October, 2014 when the wings of the VSS separated from the main fuselage causing the death of one of the two pilots. Virgin Galactic then constructed a second SS2 called Virgin Space Ship (VSS) Unity which is currently immersed in a flight

test program.

Although large scale hybrid rockets are far from competing with liquid rockets performance, these latest accomplishments of Virgin Galactic lead to think that hybrid rockets have great potential towards space travel and that they will ultimately replace solid rocket motors. Nevertheless, scientific research is still needed to fully comprehend the internal ballistics and solve the existing problems to achieve high power hybrid rockets that may cover an even wider range of applications in the future.

## 2.2 Types of rocket motors

Although the previous section only covers the historical evolution of chemical rockets, it is worth mentioning the existence of a second type of rocket propulsion called non-chemical propulsion.

Chemical rockets are based on the combustion of a propellant so as to create a high-temperature, high-pressure exhaust gas which is subsequently expanded through a convergent-divergent nozzle, which essentially converts the internal energy of the jet into kinetic energy. This group can be further divided depending on the state of the propellant used in solid, liquid and hybrid rockets.

Non-chemical propulsion uses other sources of thrust rather than a chemical reaction. On one hand, Nuclear Thermal Propulsion (NTP) aims to increase the temperature of the expelled gas based on the principle of nuclear fission of heavy elements. On the other hand, the concept of electric propulsion is based on the use of electricity to increase the momentum of a gas. There are three main types of electric propulsion thrusters attending to the type of acceleration mechanism used: electro-thermal, electrostatic and electromagnetic thrusters.

However, both types of non-chemical propulsion are exposed to major drawbacks. Regarding Nuclear Thermal Propulsion, the engineering-related problems (high complexity) and the political and social concerns had led to the cancellation or failure of all the NTP projects up to now. With respect to electric motors, they provide a huge specific impulse, nonetheless, the thrust force is minimal and insufficient for lift-off. Therefore, this makes the chemical rockets the most common and most successful type of rocket.

## 2.3 Chemical rockets

Given their wide use, a further insight on chemical rockets, and specially on hybrid rockets will be provided in the following paragraphs.

Solid rockets are characterized by the fact that the propellant is presented in solid state in the form of a grain which is encapsulated inside the motor case. This grain is composed of reducer, oxidizer and binder, and therefore, combustions starts whenever an ignition source is applied. Then, the highly-energetic exhaust gases are expanded through a nozzle. Solid-propellant rockets rely on their great simplicity and density, which allows less voluminous devices. They also permit the use of metallic additives in the grain to increase the performance. Nevertheless, they offer a relatively low specific impulse, and the oxidant-fuel mixture is difficult to manufacture, highly explosive and produces toxic fumes.

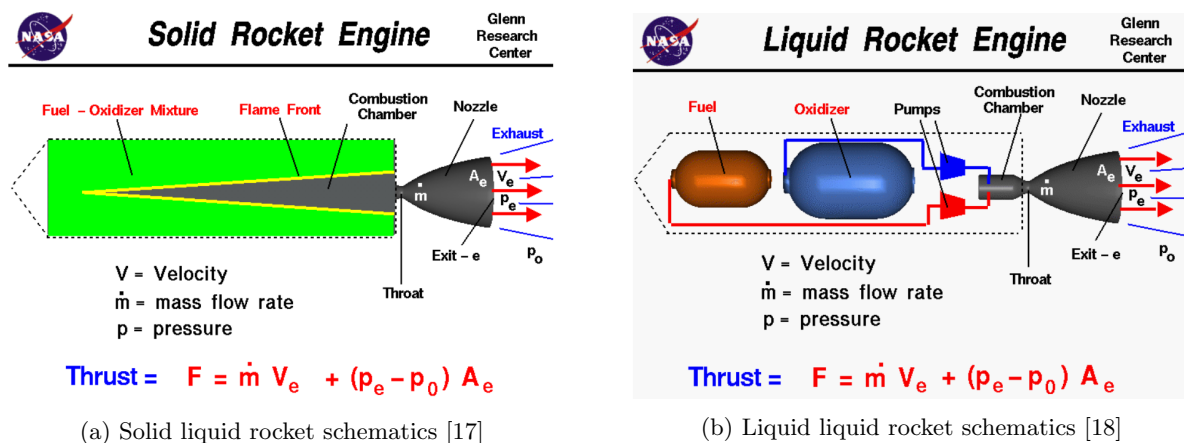


Figure 2.3: Solid- and liquid-propellant rocket motors

In liquid rockets, on the contrary, fuel and oxidizer, both in liquid state, are stored in separate tanks before being injected into the combustion chamber. Combustion occurs either spontaneously whenever the two liquids enter in contact (hypergolic reactants), or with the help of an igniter. This allows to stop and restart the rocket at will, as well as to provide throttling capabilities. Additionally, liquid rockets have a greater specific impulse than solid rockets, and they are safer given that the two reactants are stored separately. Nonetheless, they do not allow an enhancement of the combustion efficiency by the use of metallic additives, and they are far more voluminous and complex than solid rockets since they need to use pressurized tanks, pumping and injection systems, and even refrigeration system for the case of cryogenic propellants.

Finally, hybrid rockets result from a combination of the two previous types. In this type of motors, one

of the reactants, usually the fuel, remains in solid state in the form of a grain with cylindrical channels called ports encapsulated in the combustion chamber, whereas the other reactant is stored in a tank for its subsequent injection in the ports. Again, combustion can occur spontaneously or with the application of an ignition source.

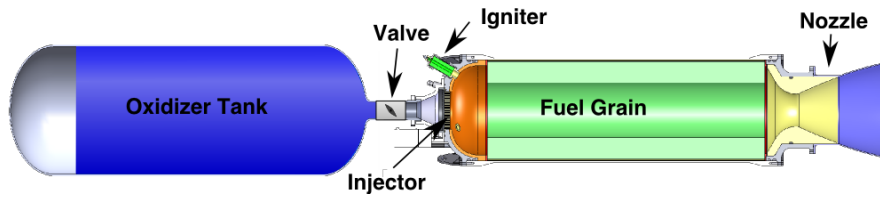


Figure 2.4: Hybrid rocket schematics [19]

This is an interesting fusion of some of the solid and liquid rockets characteristics which presents the following advantages:

- With respect to solid-propellant rockets, hybrid rockets offer a higher specific impulse, and also improve the controllability by allowing stop-restart and throttling capabilities. This allows to perform preliminary tests, and at the same time increase the safety since no self-ignition of the grain can occur. Moreover, hybrid rockets allow the addition of metallic particles to the grain so as to increase the combustion performance, as well as to modify the reactants combination with the same goal. Lastly, having a liquid oxidizer also opens the possibility to introduce a refrigerating system to diminish the temperature of the rocket nozzle walls.
- In comparison with liquid rockets, hybrid rockets present a lower specific impulse. Nevertheless, this is compensated by the significant reduction of the mechanical complexity, given that only one feeding, regulating and injection system are required. In regard to the use of cryogenic propellants with refrigerating purposes of the nozzle, a common practice in liquid rockets, the negative effect of the coupling between the propellant temperature and the motor power is reduced in hybrid rockets given that lower wall temperatures are reached, hence reducing the sensitivity of the system. Finally, the level of toxicity of the propellants used in hybrid rockets is usually smaller than in liquid rockets used for in-space propulsion, where hydrazine and its derivatives are very common.

Nevertheless, there are other important drawbacks unique to hybrid rockets:

- The modeling of the combustion process, known as internal ballistics, is extremely complex and it involves not only the combustion reaction but also fluid dynamics and heat transfer. This leads to a low and non-uniform grain vaporization, whose major disadvantage is a non-constant thrust, even in steady conditions.
- The low vaporization rate of the grain also implies a higher grain surface needed to achieve a given thrust. Therefore, more number of grain ports are necessary which ultimately leads to a more voluminous (and more expensive) motor.
- In relation with this grain configuration and its non-uniform vaporization, a substantial amount of grain remains unburned (slivers), implying lower combustion and economic performance than solid and liquid rockets.
- Finally, large scale hybrid rockets are prone to suffer from low-frequency instabilities that ultimately cause performance inefficiencies.

These are the issues that have prevented hybrid rockets to evolve as successfully as solid and liquid rockets. Hence, given all the advantages of hybrid rockets, investigation is crucial to understand and overcome those problems so as to achieve a more efficient and economic type of chemical rocket.

## 2.4 Previous evolution of the UC3M hybrid rocket prototype

Around the globe, there are numerous hybrid rocket prototypes used in undergraduate propulsion classes given their good performance and safety at a lower scale. This is also an important application of hybrid rockets since these experiments allow the students to perform small research projects, like the concerning case, which may lead to important conclusions.

For the particular case of the UC3M hybrid rocket, there were two main evolution phases prior to this project: the construction phase and a first improvement phase.

Regarding the first model of the prototype, carried out by C. Seisedos [3], it was based on the hybrid rocket of the Aeronautics and Aerospace Department of the Massachusetts Institute of Technology (MIT).



Figure 2.5: UC3M prototype after the construction phase [3]

The thruster stack was composed of: a cold block for the injection of the oxidizer (pure gaseous oxygen), a propellant block composing the combustion chamber, and a hot block containing a post combustion chamber and a convergent nozzle. The ignition was performed with the introduction of a lit match through the nozzle exit orifice. This thruster was supported by four vertical rods which were embedded into a fixed structure made of aluminum profiles.

The main objectives consisted in: fabricating the rocket from scratch, achieving a proper functioning and attempting to obtain a measurement of the thrust produced by the motor, which was expected to be of the order of 10 N. This thrust estimation was performed from the measurement of the displacement of the four supporting bars during the firing. Nevertheless, a poor calibration system and a small level of plastic deformation of the bars, led to inaccurate results.

In the second phase performed by S. Esteban [4], several improvements, mainly regarding safety were performed. Instead of a lit match, a new ignition system was installed consisting on a propane gas line and a glow plug connected to a pre-combustion chamber formed by the cold block. Additionally, a nitrogen gas line was introduced to help cleaning the combustion chamber and cooling down the thruster after each firing. These three gas lines (oxygen, propane and nitrogen) were adapted to be controlled remotely, improving therefore the safety. Also, a more accurate thrust measurement system by means of a load cell was included. This involved the construction of a sliding platform so as to allow the displacement of the rocket.

The major inconvenient found in this second phase was related to an excessive friction of the sliding platform that resulted in inconclusive readings of the load cell.

Therefore, the aim of the concerning project is to perform the necessary physical modifications of the prototype that allow a proper data collection, to be used in the subsequent the characterization of the rocket.

## 2.5 Regulatory framework

There are several perspectives with respect to the regulatory framework that could be applied to this project. Given that the prototype is far from meeting flight standards and with the main goal of ensuring risk prevention in future research, it was decided to restrict the regulatory framework to that applied to the conduction of experiments in laboratory rooms.

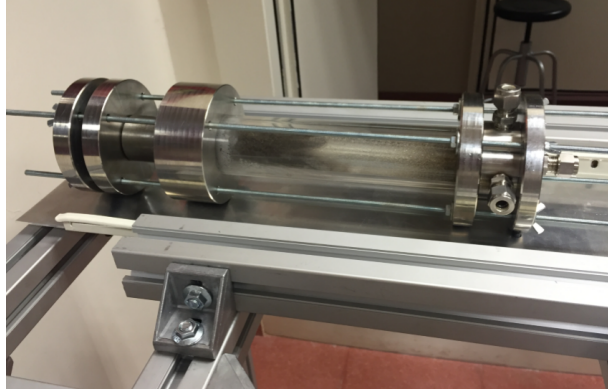


Figure 2.6: UC3M prototype after the first improvement phase [4]

The Directive 89/391/CEE is the European regulation that governs the regulatory framework of all the Member States in regard to the implementation of measures that promote the amelioration of the safety and health at work. This directive is transposed to the Spanish law by means of the Act 31/1995, of 8 November, on occupational risk prevention.

Under the action of this Law, the Royal Decree 39/1997, of 17 January, on the Regulation of Prevention Services, states the different types of preventive modalities to be applied to any company, organization or institution depending on their number of employees and characteristics. The preventive modality used in the UC3M consists of an internal prevention service, which is the agency in charge of determining both the existing labor risks in a given project and the preventive measures to be undertaken.

In the particular case of the hybrid rocket prototype at UC3M, a huge improvement in terms of risk prevention was implemented in the previous project with the remote control gas feeding system and remote ignition system. This, together with the fact that the device is enclosed in a confined space with toxic fumes concentration sensors, ensures the compliance of the project with the preventive measures. Therefore, if no significant modifications altering this configuration are undertaken, there is no need to implement further safety measures in the future.

# 3 Theoretical background

## 3.1 Hybrid rocket performance: simplified regression rate model

This section is intended to briefly address the existing theoretical knowledge of hybrid rockets focusing on the internal ballistics and the regression rate model. although this project is not focused on this regression rate analysis, a small calculation of this parameter will be provided.

As aforementioned the ignition in hybrid rockets may be initiated when the liquid reactant enters in contact with the solid grain (hypergolic reaction) or by means of an igniter.

Generally speaking, the combustion process requires the vaporization of the solid fuel in order to be burned. The heat of the initial flame will vaporize a small part of fuel that will enter in contact with the oxidizer. The resulting combustion will generate more heat, which in turn will vaporize more fuel until the whole internal surface of the grain port is covered by the diffusion flame. In fact, the reason why no successful large scale hybrid rocket has been achieved up to now is due to the fact that the polymeric fuels that are commonly used provide a very low rate of vaporization, and consequently insufficient thrust.

The specifics of the combustion process are far more complex than described above and they are still not fully understood. The modeling of this combustion process, called internal ballistics, is based in empirical data. It states that combustion takes place in a narrow zone within the boundary layer, as seen in Fig. 3.1, where stoichiometric conditions are fulfilled. Then, part of the heat flux is transmitted by convection and radiation back to the solid fuel, causing its sublimation towards the active combustion zone.

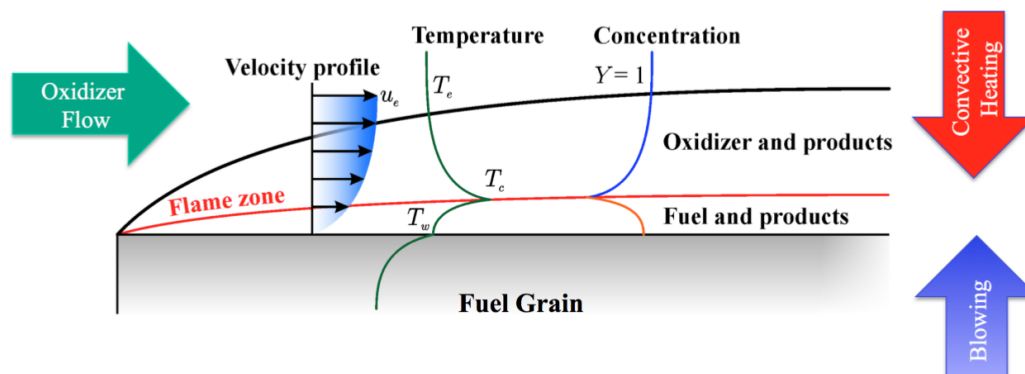


Figure 3.1: Sketch of the combustion boundary layer [2]

Nonetheless, the regression rate, i.e. speed at which the solid fuel is vaporized, is not only dependent on the heat transfer but also on the fluid dynamics problem that dictates the level of turbulence of the boundary layer. Consequently, the grain composition, the grain particles size, the geometry and thickness of the grain, the oxidizer mass flow rate or the level of turbulence, are some of the factors that have a great impact on the chamber pressure and temperature, which in turn affect the combustion process.

From these reasoning, the level of complexity of the hybrid rocket modeling is clearly visible. Research is still focused on the interdependencies of the previous factors, as well as on the prevention and control of the so called combustion instabilities that commonly appear in the process. These instabilities may be due either to the coupling between the pressure oscillations resulting from the combustion and the natural frequency of the chamber, or by the lack of stabilization of the combustion flame. In either case, the inefficiencies on the rocket performance are clear, and therefore further analysis is needed to determine the way of avoiding and controlling these instabilities.

Despite the complexity of the problem, it has been possible to develop a surface regression model. From



the literature based on said empirical studies is known that the regression rate is dependent on the (total) mass flow rate across the grain port. Obviously, the fuel mass flow increases with the axial distance along the port, which implies that the problem will be space dependent. Additionally, in general, time dependence should also be considered. Nevertheless, given that this project is not focused on the regression rate, for the sake of simplicity the time and space dependencies will be ignored, leading to the expression:

$$r = a_o G_{ox}^n = a_o \left( \frac{\dot{m}_{ox}}{\pi R^2} \right)^n \quad (3.1)$$

where  $r$  is the regression rate and  $R$  is the radius of the port. The coefficient  $n$  usually takes values between 0.3 and 0.8. It should be noticed that in the previous formula the regression rate is not proportional to the total mass flow but only to the oxidizer mass flow, which in turn is independent on the port axial coordinate. Nonetheless, this estimation can be quite accurate for values of the oxygen to fuel ratio which are sufficiently high (more than 5, in mass terms, according to Cantwell [2]). Additionally, one should be aware that the grain characteristics (geometry, particle size, additives, etc.) will affect the value of the constant  $a_o$ .

In the concerning project, the rocket performance will also be determined from the identification of the values of the previous coefficients ( $a_o$  and  $n$ ). In order to do so, the regression rate can be easily determined from the fuel mass flow rate:

$$\dot{m}_f = 2\pi R L r \rho_f \quad (3.2)$$

where  $L$  is the fuel cartridge length and  $\rho_f = 1190 \text{Kg}/\text{m}^3$  is the density of the fuel.

Therefore, once  $\dot{m}_f$  and  $\dot{m}_{ox}$  are known, the coefficients are directly calculated. Nevertheless, the estimation of  $\dot{m}_f$  and  $\dot{m}_{ox}$  requires a one-dimensional analysis of the prototype, presented in the following section, that is indeed one of the focal points of the concerning project.

## 3.2 One-dimensional model

The 1D model of the problem is based on mass conservation: the oxygen mass flow rate entering the system plus an estimated mean fuel mass flow rate consumed during the firing has to be the same as the total mass flow rate exiting the system through the nozzle.

After the simple calculation of the fuel mass flow, a solution of the oxygen mass flow will be obtained graphically, and subsequently, the calculation of the theoretical thrust force will be achieved.

### 3.2.1 Fuel mass flow rate

As seen previously, in the concerning hybrid rocket, the prototype propellant cartridge is a solid cylinder of polymethyl methacrylate (PMMA) inside of which the combustion reaction takes place.

For the estimation of the fuel mass flow rate, the PMMA cartridge is weighted before and after each firing. The difference in mass divided by the firing time will provide an average fuel mass flow rate:

$$\dot{m}_f = \frac{m_{f,ini} - m_{f,end}}{t_{burn}} \quad (3.3)$$

Unfortunately, the actual experiment is highly affected by the transient regime. Nonetheless, if the firing is sustained for a sufficient time, this transient effect can be neglected and the previous estimation could be adopted without much loss of accuracy. For this reason, the outcome of the concerning theoretical model will only be compared with the experimental data of the last instants of the firing, when the voltage readings of the two sensors of the system seem to stabilize. This data selection will be clarified in the Section 5.3.

### 3.2.2 Oxygen mass flow rate

With respect to the oxygen mass flow rate, this gas is stored in a tank placed outdoors and it is connected to the thruster assembly through a long line containing several pneumatic components, such as valves, regulators, etc. Then, the oxygen is injected in the thruster assembly through a calibrated orifice of 2.5mm diameter. Thus, the oxygen mass flow rate can be expressed in terms of the stagnation properties at the

orifice<sup>1</sup> according to the equation:

$$\dot{m}_{ox} = \rho_0 u_0 A_{hole} = \frac{P_0}{\sqrt{R_{g,ox} T_0}} \sqrt{\kappa_{ox}} M_h \left( \pi \frac{D_{hole}^2}{4} \right) \left( 1 + \frac{\kappa_{ox} - 1}{2} M_h^2 \right)^{-\frac{\kappa_{ox} + 1}{2(\kappa_{ox} - 1)}} \quad (3.4)$$

Where  $\kappa_{ox}$  is the ratio of specific heats ( $C_p/C_v$ ) and  $R_{g,ox}$  is the ideal gas constant for oxygen ( $R_u/MW_{ox}$ ).

Regarding the Mach number, since the inner diameter of the oxygen tube upstream is 5.7mm ( $> 2.5mm$ ), the calibrated orifice will be treated as the throat section of a convergent nozzle. Hence,  $M_h \leq 1$ .

On the other hand, assuming conservation of stagnation properties along the gas line, the stagnation pressure and temperature at the calibrated orifice section could be estimated a priori from the gas tank properties upstream. Thus,  $T_0$  is approximately the same as the static temperature of the tank, which in turn is equal to the ambient temperature ( $T_{amb}$ ), whereas  $P_0$  can be inferred from the tank pressure minus a total pressure drop caused by friction losses and concentrated losses along the line  $P_0 = P_{tank} - \Delta P$ . This approach was followed for the nozzle design process, as it will be discussed in detail in section 4.3.

Although this estimation was accurate enough for a preliminary nozzle design, the high uncertainty of the pressure drop ( $\Delta P$ ) has a direct impact on the uncertainty of the oxygen mass flow rate. Given the importance of the latter parameter for the rocket performance calculations, it was decided to include a pressure transducer in the oxygen line right before the calibrated orifice in order to obtain a more precise measurement.

The pressure transducer was introduced in the gas line by means of a T pneumatic connexion as shown in Fig. 3.2. From the characteristics of this type of connexion, it seems reasonable to approximate the pressure reading provided by the device as the static pressure of the line. Then, although it is expected that the tube Mach number is small enough to consider the stagnation and static properties to be equivalent, for a higher accuracy, the total pressure at this point will be estimated from the assumption that the calibrated orifice downstream is choked,  $M_h = 1$ . Then, applying equation 3.4 to both sections of the oxygen line (orifice and tube upstream):

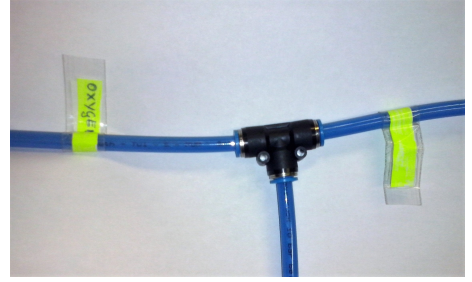


Figure 3.2: T-pneumatic connexion

$$M_{tube} \left( \pi \frac{D_{tube}^2}{4} \right) \left( 1 + \frac{\kappa_{ox} - 1}{2} M_{tube}^2 \right)^{-\frac{\kappa_{ox} + 1}{2(\kappa_{ox} - 1)}} = \left( \pi \frac{D_{hole}^2}{4} \right) \left( 1 + \frac{\kappa_{ox} - 1}{2} \right)^{-\frac{\kappa_{ox} + 1}{2(\kappa_{ox} - 1)}} \quad (3.5)$$

where:  $D_{tube} = 5.7mm$ ,  $D_{hole} = 2.5mm$  and  $\kappa_{ox} \left( = \frac{C_p}{C_v} = \frac{C_p}{C_p - R_u} \right)$  is calculated from the tabulated data of the oxygen specific heat at constant pressure ( $C_p$ ) as a function of the stagnation temperature ( $T_0 = T_{amb}$ ) [10]. Although the latter value is slightly different for each firing, the Mach number on the tube is approximately constant:  $M_{tube} = 0.112$ , which in turn is relatively small, as predicted.

Thus, the stagnation pressure of the oxygen line can be calculated from the static pressure provided by the transducer,  $P_{pt}$ , as:

$$P_0 = P_{pt} \left( 1 + \frac{\kappa_{ox} - 1}{2} M_{tube}^2 \right)^{\frac{\kappa_{ox}}{\kappa_{ox} - 1}} \quad (3.6)$$

At this point, it is also interesting to calculate the maximum oxygen mass flow rate for a given  $P_{pt}$  and  $T_0 (= T_{amb})$  by imposing choking conditions on the orifice section:

$$\dot{m}_{ox, choked} = \rho_0 u_0 A_{hole} = \frac{P_0}{\sqrt{R_{g,ox} T_0}} \sqrt{\kappa_{ox}} \left( \pi \frac{D_{hole}^2}{4} \right) \left( 1 + \frac{\kappa_{ox} - 1}{2} \right)^{-\frac{\kappa_{ox} + 1}{2(\kappa_{ox} - 1)}} \quad (3.7)$$

with  $P_0$  given by eq. 3.6.

<sup>1</sup>The orifice section is denoted with the sub-index  $h$  to avoid confusion of the sub-index  $0$  of the stagnation properties



Nevertheless, the case in which the calibrated hole is not choked also needs to be contemplated. This study is based on the assumption that the velocity of the flow in the combustion chamber is small in comparison with the velocity of the oxygen flow in the calibrated orifice (upstream the chamber) and with the velocity of the total mass flow in the nozzle (downstream the chamber). This assumption seems to be accurate since the diameters of the orifice and nozzle throat are of the order of 1mm, whereas the diameter of the combustion chamber is 20mm, which implies a cross section area, and consequently a flow rate, two orders of magnitude higher. Therefore, the static and stagnation properties at the combustion chamber will be assumed equivalent.

Then, the only unknown in equation 3.4,  $M_{hole}$ , will be given by the ratio of stagnation pressures upstream (oxygen line,  $P_0$ ) and downstream (chamber pressure,  $P_c$ ) of the orifice:

$$\frac{P_0}{P_c} = \left(1 + \frac{\kappa_{ox} - 1}{2} M_h^2\right)^{\frac{\kappa_{ox}}{\kappa_{ox} - 1}} \quad (3.8)$$

Although, the exact value of the chamber pressure is a priori unknown, it is bounded between upper and lower limits: on one hand,  $P_c \leq P_0$  (otherwise, the gases will flow from the combustion chamber towards the oxygen line) and in the other hand,  $P_c \geq P_{amb}$  (otherwise, the atmospheric air in the room will flow into the combustion chamber). Hence, the oxygen mass flow will be calculated for all the possible values of the chamber pressure:  $P_c \in [P_{amb}, P_0]$ .

In order to define properly the Mach number at the orifice,  $M_h$ , it is necessary to calculate the critical value of the chamber pressure that results in sonic conditions at this section,  $P_{c,crit-h}$ . From 3.8:

$$P_{c,crit-h} = \frac{P_0}{\left(1 + \frac{\kappa_{ox} - 1}{2}\right)^{\frac{\kappa_{ox}}{\kappa_{ox} - 1}}} \quad (3.9)$$

Then<sup>2</sup>:

$$M_h = \begin{cases} 1 & \text{if } P_c < P_{c,crit-h} \\ \sqrt{\frac{2}{\kappa_{ox} - 1} \left( \left( \frac{P_0}{P_c} \right)^{\frac{\kappa_{ox}}{\kappa_{ox} - 1}} - 1 \right)} & \text{if } P_c \geq P_{c,crit-h} \end{cases} \quad (3.10)$$

Finally, substituting  $M_h$  into eq. 3.4, the oxygen mass flow rate is determined for each of the values of  $P_c$ . With this information, it is possible to construct the interesting plot of  $\dot{m}_{ox}$  Vs.  $P_c$  which is expected to show that, for values of the chamber pressure higher than the critical (marked in red in 3.3), the oxygen mass flow rate diminishes as the chamber pressure increases, according to equations 3.10 and 3.4. A further discussion of this graph will be provided in the 6.2, although an illustrative example is provided in Fig. 3.3.

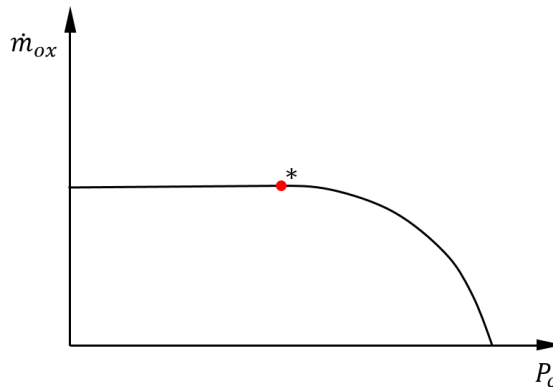


Figure 3.3: Sketch of  $\dot{m}_{ox}$  Vs.  $P_c$  graph as given by the calibrated hole

<sup>2</sup>Notice that in this case, the upstream pressure,  $P_0$ , is the fixed value, and therefore, the chamber pressure ( $P_c$ ) needs to be smaller than the critical value so that the pressure drop is high enough.

### 3.2.3 Total mass flow rate

On the other hand, the total mass flow rate can be obtained by performing an analogous calculation in the nozzle throat section, denoted with the sub-index  $t$ :

$$\dot{m}_T = \rho_C u_t A_t = \frac{P_c}{\sqrt{R_{g,m} T_c}} \sqrt{\kappa_{mixt}} M_t \left( \pi \frac{D_t^2}{4} \right) \left( 1 + \frac{\kappa_{mixt} - 1}{2} M_t^2 \right)^{-\frac{\kappa_{mixt} + 1}{2(\kappa_{mixt} - 1)}} \quad (3.11)$$

On one hand, following the same procedure as before, the chamber pressure will adopt different values in the range:  $P_c \in [P_{amb}, P_0]$ . Thus, from the previous section, it is possible to obtain the oxygen mass flow rate, which divided by the mean fuel mass flow rate from eq. 3.3 will provide the oxygen-to-fuel mass ratio of the combustion, needed to calculate the exhaust gases properties ( $\kappa_{mixt}$  and  $R_{g,m}$ ), as it will be discussed next:

$$(O/F)_{mass} = \frac{\dot{m}_{ox}}{\dot{m}_f} \quad (3.12)$$

Additionally, for each value of  $P_c$ , it is also possible to obtain the Mach number at the nozzle throat from the stagnation pressure ratio between the chamber pressure and the open atmosphere:

$$M_t = \begin{cases} 1 & \text{if } P_c \geq P_{c,crit-n} \\ \sqrt{\frac{2}{\kappa_{mixt} - 1} \left( \left( \frac{P_c}{P_{amb}} \right)^{\frac{\kappa_{mixt} - 1}{\kappa_{mixt}}} - 1 \right)} & \text{if } P_c < P_{c,crit-n} \end{cases} \quad (3.13)$$

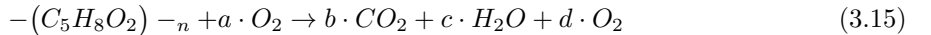
Where  $P_{c,crit-n}$  is the critical chamber pressure as given by the choking conditions **at the nozzle throat**<sup>3</sup>:

$$P_{c,crit-n} = P_{amb} \left( 1 + \frac{\kappa_{mixt} - 1}{2} \right)^{\frac{\kappa_{mixt}}{\kappa_{mixt} - 1}} \quad (3.14)$$

In regard to the calculation of the properties of the exhaust gases ( $\kappa_{mixt}$  and  $R_{g,m}$ ) needed for the previous calculations, it is necessary to perform a deeper analysis of the combustion reaction and chamber temperature addressed in the following subsection.

- **Study of the chemical reaction and chamber temperature**

Since the variation of the gases properties is expected to be small and for the sake of simplicity, the combustion reaction of oxygen and PMMA was considered to be complete and lean, neglecting the production of minor species:



The coefficient  $a$  (number of moles of  $O_2$ ) is then easily obtained from the previous oxygen-to-fuel mass ratio in eq. 3.12:

$$(O/F)_{molar} = \frac{a}{1} = a = (O/F)_{mass} \cdot \frac{MW_f}{MW_{ox}} = \frac{\dot{m}_{ox}}{\dot{m}_f} \cdot \frac{MW_f}{MW_{ox}} \quad (3.16)$$

The rest of coefficients in the reaction are then calculated from the individual balance of the different species involved in the reaction (C, H, O):  $b = 5mol$ ,  $c = 4mol$  and  $d = a + 1 - b - c/2$ .

Finally, the exhaust gases properties are given by:

$$\kappa_{mixt} = \frac{\bar{C}_{p,mixt}}{\bar{C}_{v,mixt}} = \frac{\bar{C}_{p,mixt}}{\bar{C}_{p,mixt} - R_u} \quad R_{g,m} = \frac{R_u}{MW_{mixt}} \quad (3.17)$$

<sup>3</sup>Do not confuse with  $P_{c,crit-h}$ , which is the critical chamber pressure as given by the choking conditions **at the calibrated orifice**.

Where the specific heat at constant pressure in molar basis (i.e.  $J/(molK)$ ) and the molecular weight of the mixture are given by the molar weighted average of all the products of the reaction:

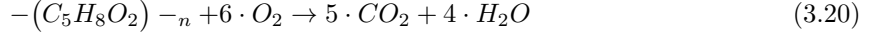
$$\bar{C}_{p,mixt} = \sum \frac{N_i}{N_{prod}} \bar{C}_{p,i} = \frac{b}{b+c+d} \bar{C}_{p,CO_2} + \frac{c}{b+c+d} \bar{C}_{p,H_2O} + \frac{d}{b+c+d} \bar{C}_{p,O_2} \quad (3.18)$$

$$MW_{mixt} = \sum \frac{N_i}{N_{prod}} MW_i = \frac{b}{b+c+d} MW_{CO_2} + \frac{c}{b+c+d} MW_{H_2O} + \frac{d}{b+c+d} MW_{O_2} \quad (3.19)$$

At this point,  $MW_{mixt}$  can be directly obtained, nevertheless, the values of  $\bar{C}_{p,i}$ , depend on the chamber temperature,  $T_c$  [10].

However, the main pending subject of this project may be the lack of a diagnosis system that allows to estimate the chamber temperature, which has led to the need of extending the theoretical analysis over a wide range of temperatures.

Initially, it was decided to estimate said range based on the value of the adiabatic temperature of PMMA and oxygen combustion reaction. A very preliminary estimation to know the order of magnitude was conducted assuming a complete stoichiometric combustion:



Then, the adiabatic temperature of the previous reaction can be obtained by equating the total enthalpy of reactants and products. As a first approach, in the following calculations, the sensible enthalpy will be approximated as:  $\Delta h_s = \int_{T_0}^{T_{ad}} C_p dT \approx C_{p,ave}(T_{ad} - T_0)$ , with the average  $C_p$  taken at 1000K. Once a first estimation of the adiabatic temperature is obtained, the calculation will be refined using directly the sensible enthalpy tabulated data ([10]) for a greater accuracy.

On one hand, the total enthalpy of the reactants is:

$$H_{react} = \sum N_i (\bar{h}_{f,i}(298K) + \bar{h}_{s,i}(T_{amb})) = \bar{h}_{f,PMMA} + 6 \cdot \bar{h}_{s,O_2}(T_{amb}) \quad (3.21)$$

where the bar denotes molar basis and  $N_i$  is the number of moles of each specie. According to the FAA (Federal Aviation Administration) [11], the heat of formation of PMMA is -184.48KJ/mol. Thus,  $H_{react}$  is fully determined.

On the other hand, the products' total enthalpy is given by:

$$H_{prod} = \sum N_i (\bar{h}_{f,i}(298K) + \bar{C}_{p-ave,i}(T_{ad} - 298K)) = 5 \cdot \bar{h}_{f,CO_2} + 4 \cdot \bar{h}_{f,H_2O} + (5\bar{C}_{p,CO_2} + 4\bar{C}_{p,H_2O}) \cdot (T_{ad} - 298K) \quad (3.22)$$

which is only dependent on  $T_{ad}$ . The, from the enthalpy balance:  $H_{react} = H_{prod}$ , with the values of  $\bar{h}_{f,i}$  and  $\bar{C}_{p,i}(@1000K)$  [10], the first approach of the adiabatic temperature is calculated to be around 6600K.

Of course this is not a realistic value given that at 6600K the metallic pieces of the thruster would have experienced serious deterioration during the firing.

If a lean combustion reaction with a molar O/F ratio of the order of 10 (common in hybrid rockets) was to be assumed, the adiabatic temperature would drop to around 5100K, but these value is still too large even to perform a refining process for the sensible enthalpy since tabulated data is only available up to 5000K. In any case, this refinement would only result in a still insufficient difference of the order of hundreds of Kelvin.

There are other sources of error which are not contemplated in this calculation that may explain such big difference between the expected and the calculated data:

- Lack of completion of the combustion reaction: PMMA may not be directly sublimated but broken down in small fragments that are not entirely combusted.
- Production of minor species from the combustion: such as carbon monoxide (CO) or hydroxy groups (OH), which would result in a lower  $T_{ad}$ .
- Heat transfer across the thruster pieces: the radiated heat flux in charge of sublimating the PMMA and the conduction heat transfer taking place across the metallic pieces of the hot block may cause a significant reduction of the calculated adiabatic temperature.

- Short duration of the firing: which may cause that the heat transfer does not reach a steady regime, hence leading to an overestimation of the temperature.<sup>4</sup>

Given the high complexity of the introduction of these aspects in the temperature calculation (this alone could be enough content for a new project), it was decided to estimate the chamber temperature based on similar experiments.

A wide research regarding PMMA combustion have been carried out. Nevertheless, most of the studies had nothing to do with hybrid rockets and in fact were focused on the spreading of the flame. Additionally, these experiments were usually performed at ambient conditions of temperature and oxygen concentration, therefore an estimation of the effect of high pressure and pure oxygen combustion will have to be assumed in the concerning case. In some of these analysis ([12], [13], [14]), the temperature of the flame was estimated to be around 1000 and 1200K at ambient conditions and 21% oxygen concentration (atmospheric air), but the most conclusive analysis was obtained from an interesting investigation performed by the Aix-Marseille Université [13]. This research was focused on the influence of oxygen concentration reduction over the flame temperature of PMMA, leading to the following approximated results for the flame temperature: 1025K(@18%O<sub>2</sub>) and 1100K(@21%O<sub>2</sub>). Doing a linear fitting, at 100%O<sub>2</sub>, the flame temperature will be near 3000K. This, of course, is a very rough approach, but it provides a good idea of the range in which the chamber temperature of our project is expected to be.

Therefore, according to the previous reasoning, taking into account that the combustion in the concerning project takes place at higher pressure than the ambient and in pure oxygen, the selected temperature range to evaluate the rocket performance is selected to be between 1400 and 2400 K.

Once the temperature range has been determined, for each pair of values assigned to  $P_c$  and  $T_c$ , it is possible to determine the remaining parameters in eq. 3.11 for the calculation of  $\dot{m}_T$ .

Furthermore, after  $\dot{m}_T$  is known, a second estimation of  $\dot{m}_{ox}$  can be obtained by simply applying:

$$\dot{m}_{ox} = \dot{m}_T - \dot{m}_f \quad (3.23)$$

Then, a different plot of  $\dot{m}_{ox}$  Vs.  $P_c$  will be constructed, containing as many curves as the values assigned to the chamber temperature. In this case, it is expected that the oxygen mass flow rate increases as the chamber pressure increases, according to equations 3.11, 3.13 and 3.23. Moreover, for values of the chamber pressure higher than the critical (marked in red in 3.4), the mass flow is proportional to the pressure. An sketch is provided in Fig. 3.4 for the sake of illustration.

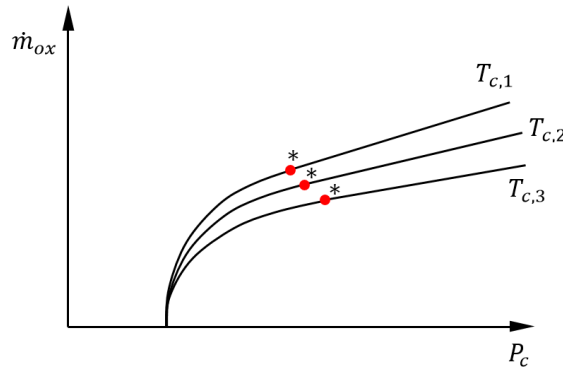


Figure 3.4: Sketch of  $\dot{m}_{ox}$  Vs.  $P_c$  graph as given by the nozzle throat

Finally, since  $\dot{m}_{ox}$  decreases with  $P_c$  as given by the calibrated orifice study (Fig. 3.3) and it increases according to the nozzle throat analysis (Fig. 3.4), it is expected that, for each of the assigned values to  $T_c$ , a solution for the oxygen mass flow rate will be obtained from the intersection of both curves. This idea will be developed deeply in the results section 6.2, once the necessary experimental data is obtained.

<sup>4</sup>When the metallic pieces are cold the conduction heat transfer is greater than when the steady operation is achieved at the pieces become hotter.

### 3.2.4 Theoretical thrust

After the oxygen mass flow is determined, the calculation of the thrust force is direct. Nevertheless, it is necessary to differentiate between choking and non-choking conditions at the nozzle throat:

$$F_{th} = \dot{m}_T v_e + (P_c - P_{amb}) A_t = \begin{cases} \dot{m}_T \sqrt{\kappa_{mixt} R_{g,m} \left( \frac{T_c}{1 + \frac{\kappa_{mixt}-1}{2}} \right)} + (P_c - P_{amb}) \left( \pi \frac{D_t^2}{4} \right) & \text{if } P_c \geq P_{c,crit-n} \\ \dot{m}_T M_t \sqrt{\kappa_{mixt} R_{g,m} \left( \frac{T_c}{1 + \frac{\kappa_{mixt}-1}{2} M_t^2} \right)} & \text{if } P_c < P_{c,crit-n} \end{cases} \quad (3.24)$$

At this point, it is interesting to notice that the dependence of the theoretical thrust force on the chamber temperature is very small: on one hand, from eq. 3.24,  $F_{th} \propto \dot{m}_T \sqrt{T_c}$ , but on the other hand, from eq. 3.11,  $\dot{m}_T \propto 1/\sqrt{T_c}$ . Thus, the dependence of  $F_{th}$  on  $T_c$  is given indirectly from the exhaust gas properties ( $\kappa_{mixt}$  and  $R_{g,m}$ ) involved in the two previous equations of  $F_{th}$  and  $\dot{m}_T$ .

This conclusion is very relevant since, in principle, it would be possible to obtain an estimation of the chamber temperature from the comparison of this theoretical thrust with the thrust measurement given by the load cell. A deeper analysis of this will be provided in the results section 6.2.

## 4 Experimental setup

Although a brief description of the thruster arrangement was introduced in the State of the Art chapter 2, a more exhaustive characterization of each of the components of the system is provided in this section.

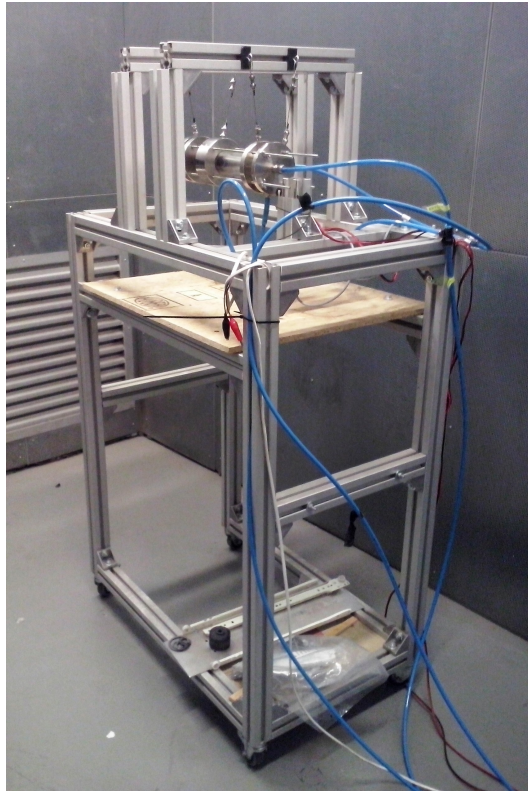


Figure 4.1: Complete rocket system

### 4.1 Design requirements

As mentioned before, one of the main objectives of this project was to upgrade the already existing rocket in order to develop a proper performance analysis. Given its overall good conditions prior to this project, and in order to avoid unnecessary manufacturing delays and costs, most of the pieces of the assembly were reused.

Nonetheless, a well known fact from previous experiments was that the nozzle throat diameter was too large to reach sonic conditions. For this reason, two new nozzles with smaller diameters were manufactured. A detailed explanation of the design process is provided in 4.3.

Additionally, another goal of this project was to perform a parametric study on how the fuel cartridge length affects the rocket thrust. Therefore, apart from the existing PMMA tubes length, a second shorter set of propellant tubes (inner and outer) was manufactured.

Moreover, the previous configuration of the sliding structure was thought to exert a friction force that was too large to be overcome by the thruster force, and therefore, it was not possible to obtain a precise measurement of the thrust force. Thus, with the objective of diminishing friction, a new supporting structure inspired in a battering ram was designed and constructed using aluminum profiles and steel cable.

Another important new element of this project was the pressure transducer of the oxygen line, which allowed to obtain a good estimation of the total pressure loss on the oxygen line.

The introduction of this transducer led to a modification in the data acquisition system: it was necessary to feed two sensors as well as obtaining their corresponding output signals.

Despite all these adaptations, it was essential to maintain the modular character of the rocket so as to being able of perform the required parametric studies and allow future upgrades of the design.

## 4.2 Description of the blocks and parts

As mentioned in the introduction, the total project of the rocket can be divided in several subsystems: thruster stack (the rocket itself), supporting structure, diagnosis system (load cell and pressure transducer), pneumatic system, and electric and electronic system.

The thruster assembly per se is divided in three blocks: cold block, propellant block and hot block as it can be seen in Fig. 4.2.

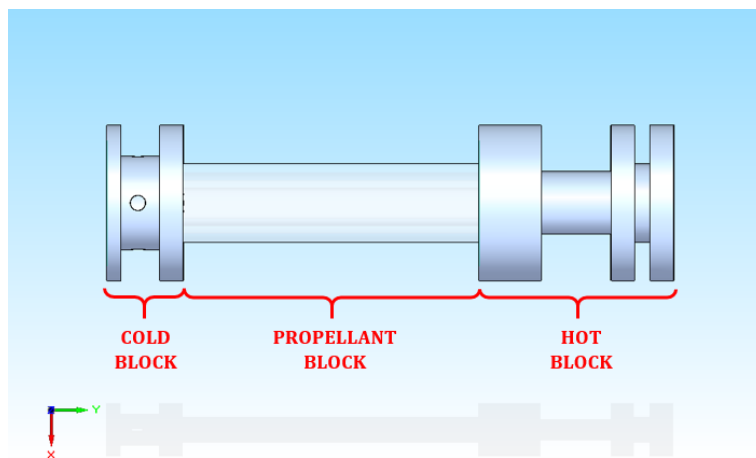


Figure 4.2: Thruster assembly CAD view: cold block, propellant block and hot block

In this section, a description of each block and the parts that compose them are provided, illustrated with CAD pictures performed in Solid Edge. Additionally, the arrangement used to join the three blocks is also included.

The nomenclature of the pieces (Fig. 4.3) follows the next criterion: stainless steel pieces are named with numbers from front to back, except for the nozzle, which will be referred as nozzle-XX, where XX denotes the value of the throat diameter in mm; propellant tubes will be named as inner and outer tubes; and finally, the only part of the rocket made of graphite will be named graphite part.

### 4.2.1 Cold block

As aforementioned, in the previous upgrade of the prototype, a new remote ignition system was installed, where the first flame was provided through the use of propane gas: once the oxygen valve is fully open and the gas is flowing along the thruster, a small flow of propane is gradually injected into the pre-combustion chamber (i.e. the cold block). When the oxygen-to-propane ratio is high enough, the glow plug produces a spark, which creates the first flame. This flame then travels downstream towards to the propellant block, and therefore, the PMMA cartridge starts to burn. At this point, the combustion process no longer takes place in the pre-combustion chamber but in the propellant block, and the propane flow is killed.

Hence, the function of the cold block is to compose said pre-combustion chamber where the reaction is initiated. For a simpler manufacturing of the chamber cavity, the cold block assembly was composed by two metal pieces: the first one contains all the orifices for the injection of each of the three gases (oxygen, propane and nitrogen), as well as for the fitting of the glow plug; and the second one closes the cavity and provides support for the propellant tubes of the next block.

In regard to *Piece 1*, three of the orifices are located in the perimeter and the last one, along the

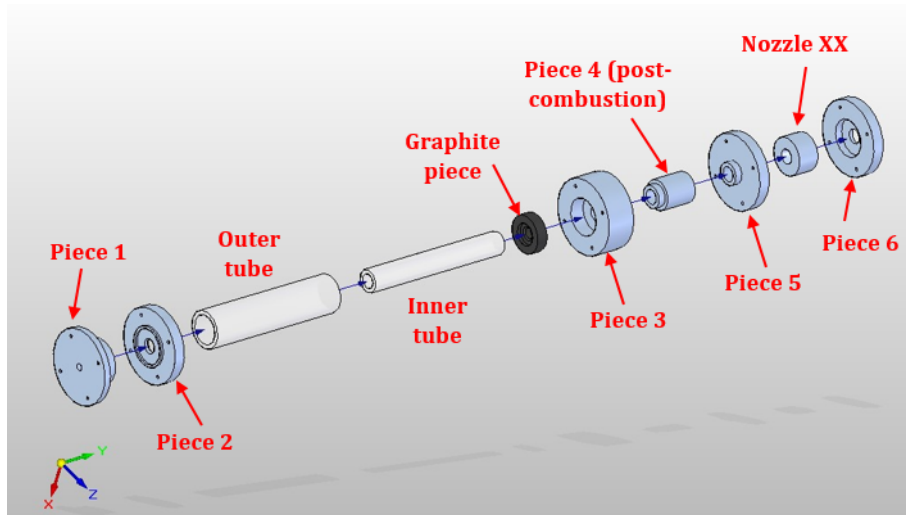


Figure 4.3: Exploded CAD view of the thruster assembly including the name of the parts

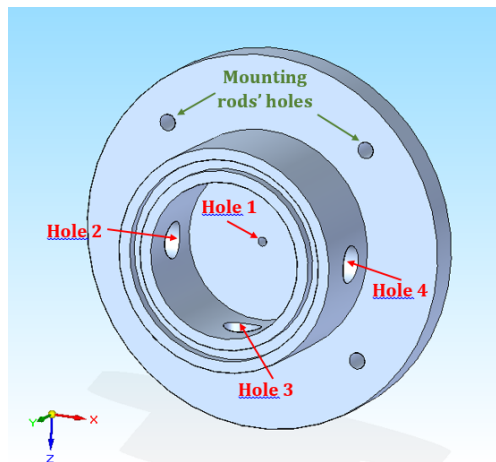


Figure 4.4: Piece 1, back view

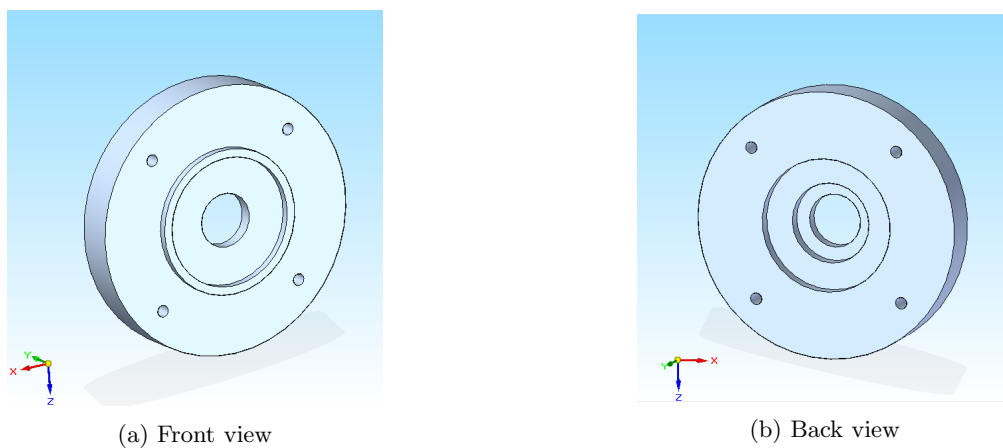


Figure 4.5: Piece 2 CAD views

longitudinal axis of the assembly. According to the orifices nomenclature in Fig. 4.4: *Hole 1* is connected to the oxygen line, which allows a longitudinal feeding of the gas towards the propellant tube; *Holes 2* and *3* are connected to the propane and nitrogen gas lines, respectively; and *Hole 4* corresponds to the location



of the glow plug.

The three gas lines are connected by means of compressions fittings to *Piece 1*, as seen in Fig. 4.6. The fuel line is fed laterally to provide a better mixing with the oxygen. Nitrogen is used to expel the exhaust gases out of the rocket once the firing has stopped and to help cooling down the assembly. As seen in the 1D model Section above, the oxygen orifice is calibrated with a diameter of 2.5mm, allowing a precise calculation of the oxygen mass flow entering the rocket. In regard to the glow plug, it is directly threaded into its corresponding hole.

With respect to *Piece 2*, it is pressed against the first one by means of an annular protrusion which guarantees a proper fitting. The other side of this part presents a big orifice which communicates with the propellant block.

Both pieces, as the rest of metallic pieces of the assembly, are made of stainless steel 304 given that they are in contact with pure oxygen and thus, need to be corrosion resistant. Another reason to use this material is that it is relatively easy to machine and that the necessary machinery to do so is available at the own campus facilities, which leads to a decrease of the cost. Additionally, stainless steel shows good performance at high temperatures. Nonetheless, it has a relatively high density ( $8000\text{kg}/\text{m}^3$ ), but since the scope of this project is to obtain measurements of the thrust in a test bench (i.e. flight is not intended at this point), the weight of the device has not been of the concerns of this project up to now.

## 4.2.2 Propellant block

The propellant block is where the combustion takes place, and thus, it will also be referred as combustion chamber. It is composed of two concentric PMMA (polymethyl methacrylate) tubes with a hollow space between them: the inner tube is the fuel cartridge per se, and the outer one is only used as a safety element, in case the inner tube melts, or explodes (very rare).

The assembly of both tubes between the cold and hot blocks is performed in such a way that the oxygen only flows through the interior of the inner cylinder, the port, being the combustion reaction confined to this space, whereas the volume between the inner and outer tubes contains only stagnant air as shown in Fig. 4.7

The values of the inner and outer diameters of each tube are presented in the table below:

PMMA tube	Inner	Outer
Inner diameter (mm)	20	40
Outer diameter (mm)	30	50

Table 4.1: PMMA tubes inner and outer diameter.

Regarding the cartridge length, as mentioned before, two set of tube have been produced for the parametric study whose lengths are shown in table ??.

In both cases, the outer tube is 1 cm shorter to ensure a proper fitting between the propellant block and the cold and hot blocks.

In this case, the reasons to use PMMA are: easy combustion, no production of toxic fumes (only small concentrations of  $CO$ ), easy machining process, and high transparency, which allows to have a clear view of

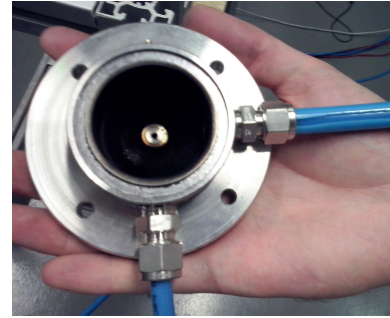


Figure 4.6: Real picture of Piece 1

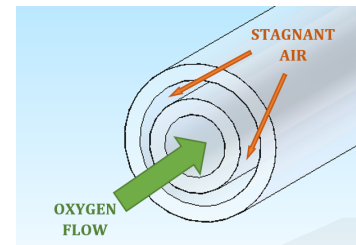


Figure 4.7: Propellant block: combustion chamber and confined air

PMMA tube	Inner	Outer
Length 1 (mm)	210	200
Length 2 (mm)	150	140

Table 4.2: PMMA tubes length.



Figure 4.8: Sets of propellant tubes: 210mm on the left and 150mm on the right

the flame and the deterioration of the fuel cartridge during the firing to stop the rocket if needed.

### 4.2.3 Hot block

The hot block is the most complex given that it is composed by 6 pieces. It has two main functions: on one hand, it contains a post-combustion chamber in order to optimize the degree of completeness of the reaction before reaching the nozzle; and on the other hand, the inclusion of the nozzle allows the exhaust gases to accelerate, and transforms their internal energy into kinetic energy, which ultimately will cause a thrust force on the rocket, according to eq. 3.24.

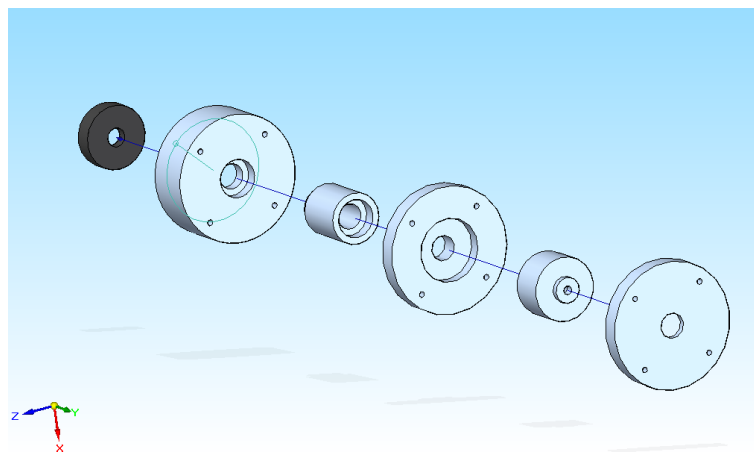


Figure 4.9: Exploded view of the hot block subassembly

In first place, right after the propellant block, as it can be seen in the previous picture, there is a graphite piece which is totally embedded into *Piece 3* (see Fig. 4.10). The function of this piece is to protect the latter from the high temperatures of the combustion gases due to the high melting point of graphite (around 3800K). Additionally, the smallest diameter of this piece protrudes into the gas duct (see Fig. 4.11) so as to introduce a source of turbulence and further facilitate the completion of the combustion reaction before reaching the nozzle.

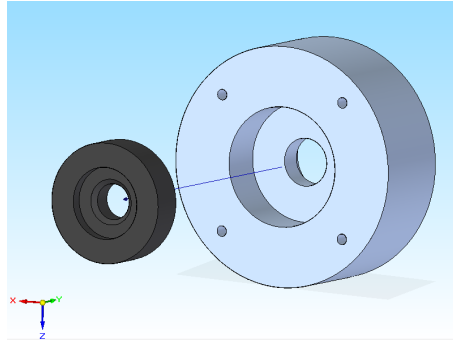


Figure 4.10: Graphite piece relative position to Piece 3

*Piece 3* is in charge of providing structural support: on one side, to the propellant block, and on the other side to the post-combustion chamber, i.e. *Piece 4*.

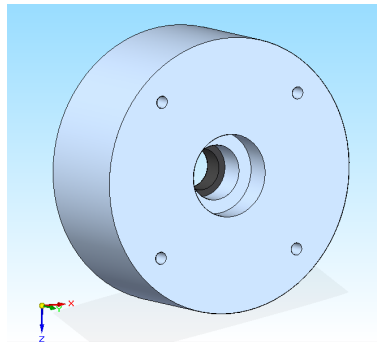


Figure 4.11: Piece 3 back view

*Piece 4* composes the so called post-combustion chamber, which as mentioned above, increases the degree of completion of the combustion. In this way, fuel efficiency, and consequently, thrust force will be maximized.

The post combustion chamber is the metallic part that reaches the highest temperature after each experiment, a fact that can be the cause of the corroded appearance of the piece that has been materializing over the years. The high temperature is explained by two unique aspects of this piece: on one hand, it is the longest piece of the hot block, which implies a greater surface area exposed to the hot gases; on the other hand, it is also the piece with the thinnest walls, which implies lower heat absorptivity, i.e. for the same amount of heat absorbed by the piece, there is less amount of mass to be distributed into, and thus, a higher temperature is reached.

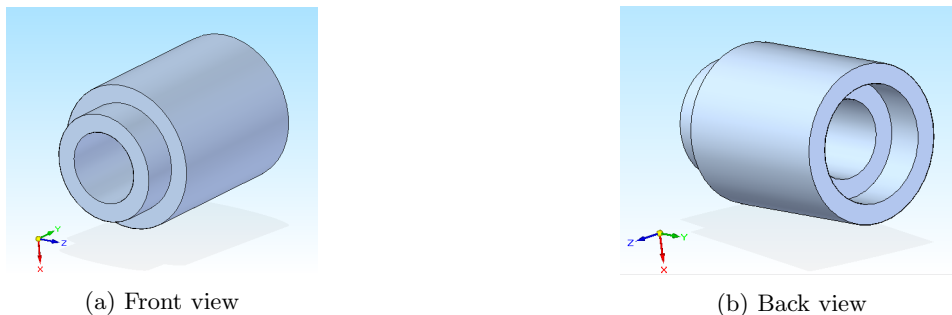


Figure 4.12: Piece 4 CAD views

*Piece 5* also provides support on one side, to the post-combustion chamber, and on the other side to the nozzle.

Regarding the nozzle, it has been one of the most important modifications of this project. In the past,

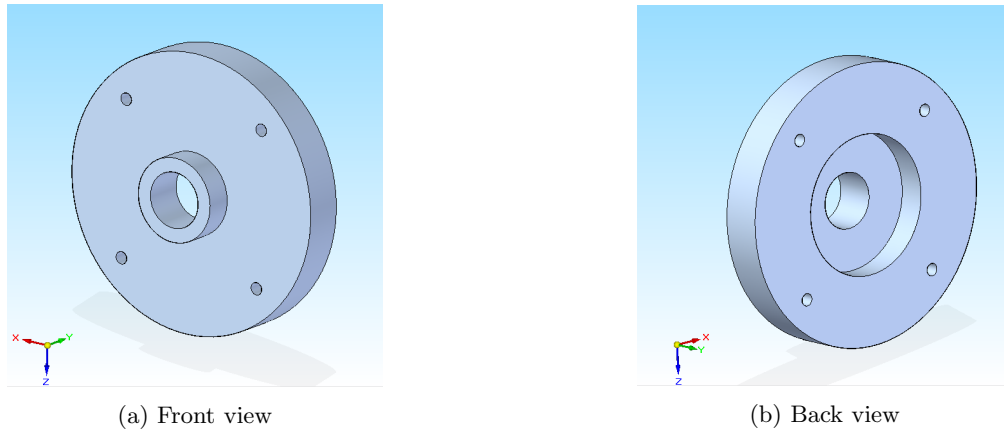


Figure 4.13: Piece 5 CAD views

this piece was made of graphite, in order to ensure that it will withstand the high temperatures. The convergent shape was selected with the aim of potentially reach sonic conditions at the throat and also to avoid the complexity of the convergent-divergent nozzles oblique shock waves. Nonetheless, the throat area was too high to become choked. Additionally, the relatively high velocities of the flow at this point were believed to cause a gradual erosion of the piece as experiments were performed. This would have led to a further increase of the throat area up the actual diameter of 9.5mm, which in turn would have resulted in an important decrease of the thrust.

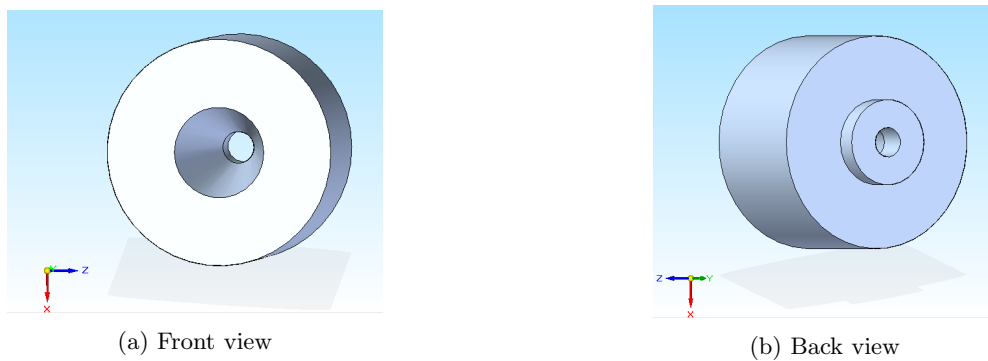


Figure 4.14: Nozzle (6mm throat diameter) CAD views



Figure 4.15: Comparison of nozzle throat diameters. From left to right: 4mm, 6mm and 9.5mm

This is why two new nozzles were designed with smaller throat diameters (6 and 4mm) in order to study their sonic state and their effect in the thrust force. Despite its lower thermal capabilities with respect to the graphite, they were made of stainless steel. This decision was based on the short duration of the rocket firing (insufficient to cause the melting of the pieces), and that in this way, they could be manufactured in the campus facilities, saving time and cost. The detailed design process of the nozzle is provided in Section 4.3.

Finally, in order to support to the nozzle and the total assembly, *Piece 6* is placed at the end of the thruster stack.

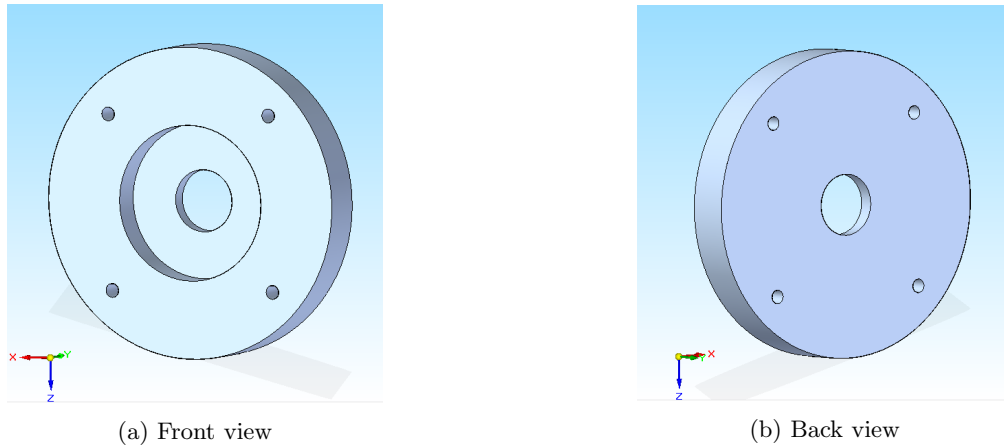


Figure 4.16: Piece 6 CAD views

#### 4.2.4 Rocket assembly

As seen in the picture below, the 10 parts composing the rocket are mounted along four guiding threaded rods and tighten by means of wing nuts at both ends of each rod.

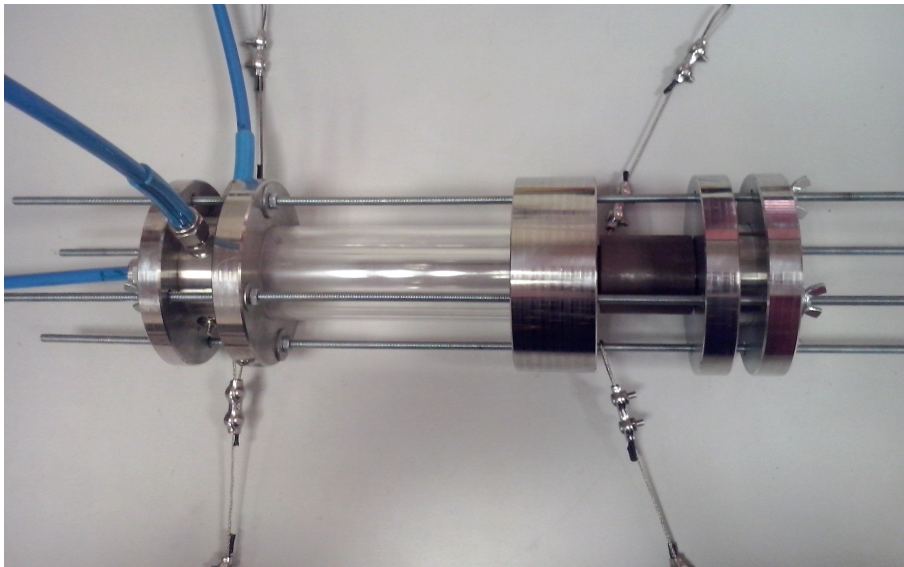


Figure 4.17: Real picture of the thruster stack

These wings nuts will be only finger-tight so as to avoid damaging the propellant block due to high structural stresses. Additionally, given that all the pieces will show some degree of thermal expansion during the firing, this will provide higher tightness to the whole assembly, reducing the risk of leakages.

Moreover, all the parts have been manufactured with proper clearance to fit perfectly between them. Nevertheless, to avoid any gas leakages that could lead to inefficiencies or even result in an explosion, graphite gaskets (available in two different sizes) are placed at both ends of the inner propellant tube and between every two metal pieces of the hot block.

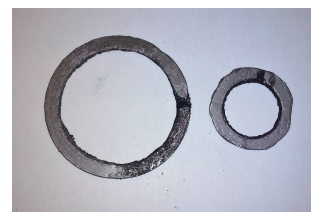


Figure 4.18: Graphite gaskets

## 4.3 Nozzle design

The nozzle may be one of the most important pieces of the rocket given that it is directly linked to the production of the required thrust: the reduction of the gas duct implies that a higher velocity is achieved. Then, since the thrust force is proportional to the exit velocity, a smaller nozzle throat section produces higher thrust.

As mentioned in Section 3, the design of the nozzle is also based on the 1D theoretical model. In fact, an analogous development of the subsection is going to be performed. Nevertheless, the objective of this section is not to calculate the theoretical thrust force, but to determine the nozzle throat diameter that results in choking conditions at this section.

### • Fuel mass flow rate

On one hand, the fuel mass flow rate is estimated according to eq. 3.3. The necessary data for this calculation was taken from the laboratory practice of the Bachelor subject of Rocket Motors performed in November, 2016 in which one rocket firing was successfully completed. In this lab session, the initial and final fuel mass were:  $m_{f,ini} = 93.6g$  and  $m_{f,end} = 78.9g$ . The burning time, estimated from the duration of a video recording performed during the firing, was:  $t_{burn} = 10s$ . Substituting these values into the previous equation, the steady fuel mass flow rate was estimated to be  $1.47g/s$ .

### • Oxygen mass flow rate

On the other hand, for the estimation of the oxygen mass flow rate, the calibrated orifice of the oxygen line is again modeled as a nozzle, according to eq. 3.4.

Given that, at the time when the lab session of Rocket motors was celebrated (Nov., 2016) the pressure transducer was not incorporated to the system yet, the following assumptions for the estimation of the oxygen mass flow were taken:

- The stagnation pressure is estimated from the oxygen tank pressure (6 bar of relative pressure) and assuming a pressure drop along the line of 1 bar:  $P_{0,rel} \approx 5bar$  (relative pressure). Then, the absolute pressure at the hole is:  $P_0 = P_{0,rel} + P_{amb} = 5.936bar$
- The stagnation temperature at the hole is assumed to be the same as the static temperature of the tank which is located outdoors (i.e.  $T_{tank} = T_{amb}$ ):  $T_0 \approx T_{amb} = 298K$ . In reality this value should be higher than the ambient due to friction with the walls of the line.
- Given the high values of the estimated stagnation pressure, it seemed very reasonable to think that the calibrated hole would be choked ( $M_{hole} = 1$ ), thus, this assumption was also included.

Then, knowing that the diameter of the calibrated hole is  $2.5mm$ , and taking the ratio of specific heats at  $T_{amb} = 298K$  ( $\kappa_{298} = 1.3959$ ), the oxygen mass flow was estimated to be:  $\dot{m}_{ox} = 7.16g/s$ .

### • Total mass flow rate

Following the reasoning of the 1D model, the total mass flow rate can be obtained from the analysis of the nozzle throat, as given by eq. 3.11. On one hand, from the previous solutions of  $\dot{m}_f$  and  $\dot{m}_{ox}$ , the total mass flow rate is:  $\dot{m}_T = \dot{m}_{ox} + \dot{m}_f = 8.63g/s$ ; and the oxygen-to-fuel ratio:  $(O/F)_{molar} = \frac{\dot{m}_{ox}}{\dot{m}_f} \cdot \frac{MW_f}{MW_{ox}} = 15.227mol$ .

According to the calculations of the lean combustion reaction performed in Section 3 for the obtaining of  $\kappa_{mixt}$  and  $R_{g,m}$ , knowing the O/F ratio, it is possible to get  $R_{g,m}$ . Nonetheless, the specific heat at constant pressure of each specie, used in the calculation of  $\kappa_{mixt}$ , depends on the temperature.

Therefore, the only two unknowns left in the previous equation are the chamber pressure and chamber temperature. Again, the lack of means to obtain a measure of these two parameters led to the analysis of several possible scenarios for different combinations of chamber pressure and temperature.

In the discussion of the 1D model, the chamber pressure was bounded between the atmospheric pressure and the stagnation pressure of the oxygen line. The upper is still given by the stagnation pressure on

the oxygen line, that is estimated to be  $5.936bar$ , as mentioned before. Nonetheless, since the aim of the concerning nozzle design process is to reach sonic conditions at the throat, in this case minimum chamber pressure is imposed to be higher than the critical pressure as given by the nozzle choking conditions, instead of the ambient pressure:

$$P_c \geq P_{c,crit-n} = P_{amb} \left( 1 + \frac{\kappa_{mixt} - 1}{2} \right)^{\frac{\kappa_{mixt}}{\kappa_{mixt} - 1}} \quad (4.1)$$

where the ambient pressure was obtained from the International Standard Atmosphere model for the corresponding altitude in Leganés (666 m above sea level):  $P_{amb} = 0.93576bar$ .

In regard to the chamber temperature, the parameter  $\kappa_{mixt}$  will be obtained for a wide range of temperature values (1200, 1500, 1800 and 2100K)<sup>1</sup>, which substituted into eq.(4.1) would lead to the corresponding critical values of the chamber pressure.

Then, the final solving procedure has been performed graphically in the following way: a plot (Fig. 4.19) of  $\dot{m}_T$  Vs. throat diameter of the nozzle is constructed according to eq. (??) showing 4 lines which correspond to each of the previous values of the temperature. In all 4 cases, the chamber pressure is selected to be the minimum one, i.e. the critical pressure (which will be different for each temperature value). Additionally, in the same plot, the value of  $\dot{m}_T = 8.63g/s$ , calculated as the sum of  $\dot{m}_{ox}$  and  $\dot{m}_f$ , will be represented.

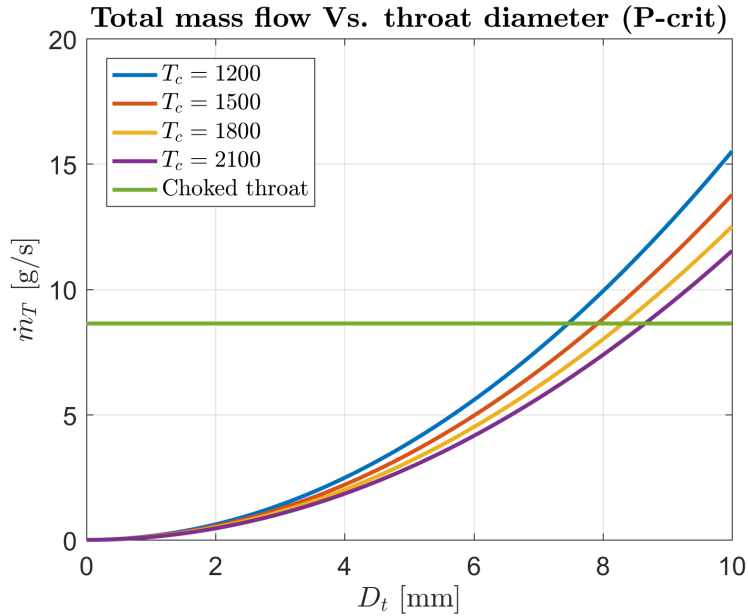


Figure 4.19:  $\dot{m}_T$  Vs.  $D_t$  for minimum chamber pressure ( $P_{amb}$ )

The intersection of each of the 4 previous curves with the horizontal line will provide the maximum value of the throat diameter that would result in choking conditions for that given value of the chamber temperature. Thus, for minimum chamber pressure ( $P_{c,crit}$ ) and  $T_c = 2100K$ , the throat diameter  $D_t$  should be smaller than  $\approx 8.6mm$  to ensure sonic conditions, whereas at  $T_c = 1200K$  the maximum value of  $D_t$  is  $\approx 7.5mm$ . Consequently, the smallest value should be chosen to ensure that the throat will be choked independently on the temperature value.

Nevertheless, it is important to recall the great number of assumptions and approximations that have been performed. Hence, it is very advisable to undertake a conservative approach when selecting the throat diameter of the piece to be manufactured. For this reason, although the graph shows a maximum value of  $D_t \approx 7.6mm$  (at 1200K), it was decided to reduce this number down to 6mm for the first nozzle.

Moreover, it is also convenient to analyze the case for which the chamber pressure is higher than the minimum, for example  $P_c = 3bar$ . Then, the previous graph is shifted to the left, as shown in Fig. 4.20.

This implies that for the throat diameter selected for the first nozzle (6mm), sonic conditions will only

<sup>1</sup>Notice that this calculation was performed prior to the previous study of the chamber temperature, and given that this is a conservative selection, it is perfectly valid.



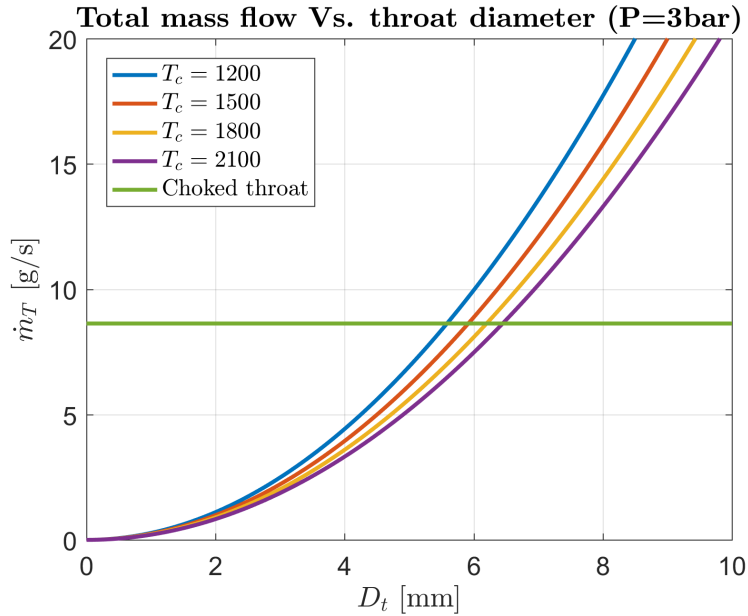


Figure 4.20:  $\dot{m}_T$  Vs.  $D_t$  for 3bar chamber pressure

be reached for a chamber temperature  $\geq 1600K$ . This is easily explained from eq.(??): for the same value of  $T_c$  and  $\dot{m}_T$ , if the chamber pressure increases,  $D_t$  needs to decrease.

Hence, to ensure that choking conditions are achieved at higher chamber pressures, it was decided to manufacture a second nozzle with a very conservative selection of 4mm throat diameter.

In this way, having two nozzles of different throat sections will allow to perform a parametric study of the effect of this factor on the rocket thrust. Additionally, the difference of 2mm between them is high enough to expect clearly differentiated results.

## 4.4 Machining of parts

The rocket is composed of parts made of three different materials: stainless steel (Pieces 1 to 6 and the nozzle), PMMA (inner and outer tubes) and graphite (graphite piece).

With respect to the graphite part, the manufacturing process is uncertain, given that it was ordered to an external company, although most likely it will consist in a 3D printed piece.

With respect to the PMMA tubes, since the hollow tubes are already purchased with the required diameter dimensions, the only machining necessary is the cutting process of the cylinders to obtain the selected length values.

Finally, the machining process of the stainless steel parts is the most complex and time consuming one. All pieces are manufactured from a 100 mm diameter bar of stainless steel AISI 304L. Again one of the reasons to choose this material was that it was easily machined.

The process was analogous for all the stainless steel pieces:

1. A piece 2 mm longer than the length of the piece to be manufactured is cut off from the steel bar using a industrial belt saw.
2. The piece of steel is clamped in the lathe and it is faced to reduce the length to the final value.
3. The external profiling is performed (if required).
4. In the own lathe, all the drilling processes necessary to define the internal profile of the piece are carried out.



5. Also in the lathe, the piece is chamfered so as to eliminate any possible burrs.
6. Finally, for pieces 1, 2, 3, 5 and 6, four holes, equidistant from the center, are performed at  $\pm 45^\circ$  and  $\pm 135^\circ$  with respect to the horizontal so as to introduce the guiding rods that join the three blocks of the rocket stack together.

## 4.5 Support Structure

As mentioned before, the main difficulty of the previous rocket configuration was the excessive friction force produced in the sliding structure that prevented the assembly to start the motion, and as a consequence, no measure of the thrust could be obtained.

With the aim of minimizing the friction, a new supporting structure resembling a medieval battering ram was designed, as shown in Fig. 4.21. In this way, the thruster remains suspended from steel cables and thus, the friction force is almost canceled.

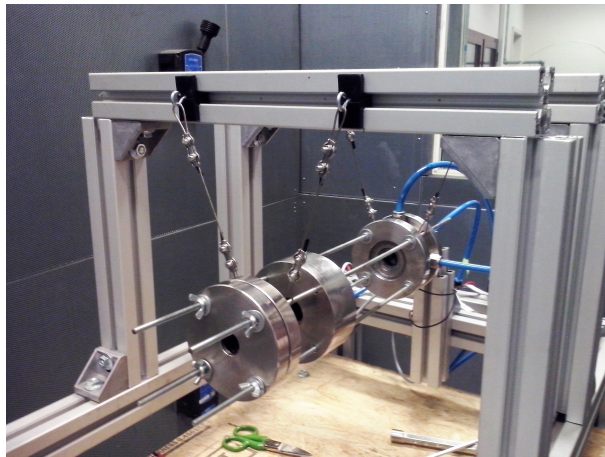


Figure 4.21: Rear view of the battering ram structure

The four vertical aluminum profiles need to be manufactured, but the two horizontal profiles, as well as the two profiles used for the proper allocation of the load cell, were recycled from the previous sliding structure.

Regarding the steel cables, 4 cable runs of 10 cm each were cut. The ends were bended and fixed with the help of slings. On one of the extremes of the cable, the loop was introduced along the rods of the thruster assembly: two in the front part and the other two in the rear part. In order to do this, it was necessary to completely disassemble the thruster and introduce the cable in the rod in between the two desired consecutive parts before re-assembling again. In the other extreme, the other loop was introduced into a hook fitted into the horizontal aluminum profiles as shown in Fig. 4.22. The black plastic piece used for this goal was not completely fixed to the aluminum profile so as to allow small adjustments of the hooks longitudinal position if needed.

In principle, the idea of including hooks was thought to make the assembling and disassembling process between experiments easier and faster by unhooking and hooking the thruster from the structure. Nonetheless, the close location of the cell load and the rigidity of the three gas tubes in the cold block, led to conclude that it was indeed simpler and faster to perform the assembling and disassembling on the thruster while hooked, always taking care of avoiding hitting the load cell in the process.

## 4.6 Diagnosis system

The main objective of this project is to achieve a further understanding of the hybrid rocket performance from the comparison between the experimental data and the theoretical 1D model results. For both aspects,



Figure 4.22: Hooks, steel cables and aluminum profile arrangement

it is essential to gather information by means of a proper diagnosis system.

On one hand, a load cell will measure the actual thrust force produced by the rocket. This element was already introduced in the previous configuration, but due to the excessive friction force of the sliding structure, the rocket was unable to move and reach said device.

On the other hand, as aforementioned, a very significant improvement of this project is the introduction of a pressure transducer in the oxygen line in order to provide a more accurate measure of the pressure drop in the gas line, and consequently obtain a better estimation of the oxygen mass flow rate.

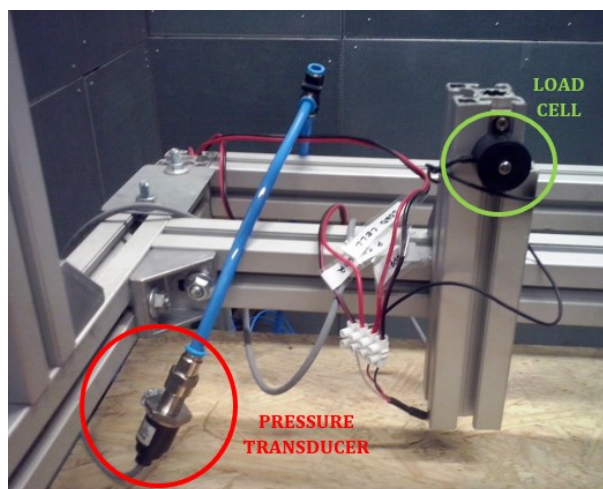
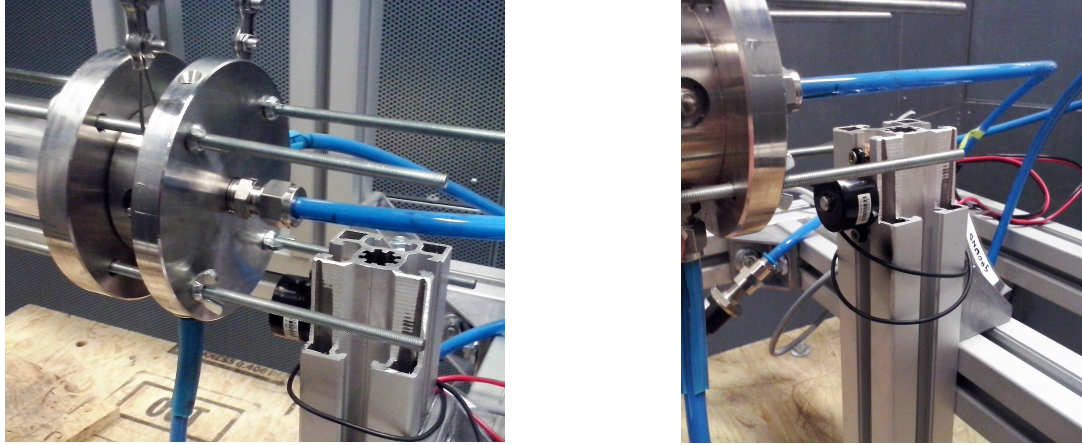


Figure 4.23: Sensors location in the empty structure

#### 4.6.1 Thrust measurement: load cell

As mentioned above, the load cell was already an element of the rocket in the previous project. In the concerning model, the device was mounted fore of the rocket assembly by means of two aluminum profiles (recycled from the previous arrangement), as it can be seen in figures 4.23 and 4.24. When the rocket presses the load cell, the output voltage reading of the device reflects that force.

According to the datasheet provided in Appendix, the device is able to measure a force up to 10 lbf (4.536 kgf) when fed with a supply of 5 Volts. It is a ratiometric sensor, therefore, the voltage of the output signal is proportional to the input voltage, with a zero output voltage value of 0.5 V and a maximum output voltage of 4.5. Therefore, with these two data points it is possible to build the characteristic line of the load cell, exhibited in Fig. 4.25.



(a) Front view

(b) Back view

Figure 4.24: Load cell location relative to the thruster assembly

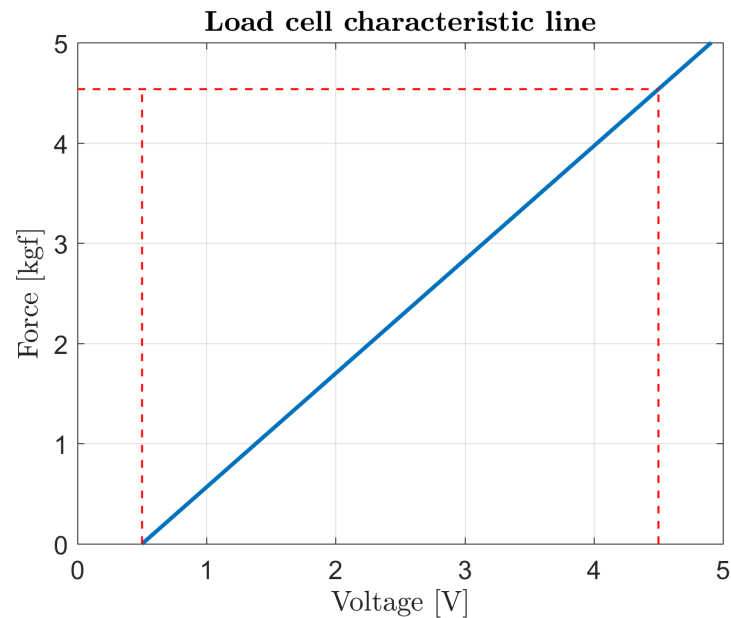


Figure 4.25: Characteristic line of the load cell according to the datasheet specifications

However, a calibration test was performed to check the validity of said line. This procedure will be described in detail in section 5.1.

Finally, the detailed electronic connexions of the cell will be presented in the following section.

#### 4.6.2 Oxygen line pressure drop measurement: pressure transducer

In the past, one of the major uncertainties to be determined was the pressure drop along the oxygen line. The lines of the three gases (oxygen, propane and nitrogen) are almost the same, but only the pressure drop of the oxygen line is of interest for the mass flow rate calculation.

The gas lines start in the tanks, placed outside the building, which count with a pressure regulator. Nonetheless, inside the lab room there is another regulation system shown in Fig. 4.26 so as to remotely control the ignition and operation of the rocket. It counts with a second regulator, a butterfly valve, and only for propane and oxygen, an additional flame extinguisher valve. These three elements produce a significant pressure drop that turned out to be underestimated in the calculation of the nozzle design, as it will be discussed in subsequent sections.



Figure 4.26: Gas flow regulation system. From left to right: propane, nitrogen and oxygen lines

The tanks are connected to the regulation system in the lab room by several meters of stainless steel tube, whereas from this point to the rocket in the test room the gas is conducted by polyurethane tubes. Apart from the friction pressure drop, the line also counts with several elbows and bends that produce additional concentrated losses.

From this description of the gas lines, it can be concluded that, given the lines length (8 to 10m approximately) and the numerous pneumatic components, the pressure drop along the oxygen line is difficult to be estimated, and therefore, a pressure transducer was installed.

As seen in Fig. 4.27 the sensor counts with a pressure port on one side and with the electrical connexion on the other. The pressure port is connected to the oxygen tube through a raccord. With regard to the pneumatic installation of the pressure transducer, as it was already explained in the theoretical section, it was required to introduce a T-joint in the oxygen line. Regarding the electronics, the sensor counted with a 1m cable containing the three connexions of the sensor: voltage supply, output signal and ground. The detailed connexions will be explained in the next section.

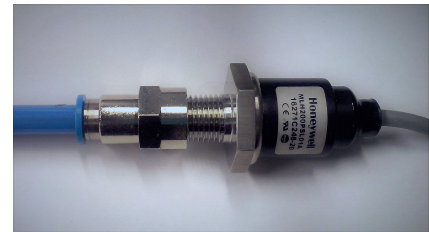


Figure 4.27: Pressure transducer

In accordance to the datasheet (provided in annex Appendix), the reading of the pressure transducer is analogous to that of the load cell: a ratiometric output signal between 0.5 and 4.5 V (for null and maximum relative pressure respectively) when the device is fed with a 5 V supply. Thus, given that the maximum relative pressure allowed by the transducer is 200psi (13.79 bar), its characteristic line is represented according to the graph in fig. 4.28.

An important remark is that the pressure transducer is a sealed gauge. Therefore, by definition, the output provided by the transducer is referenced to the value of the atmospheric pressure in which the transducer was hermetically sealed. Therefore, for a correct estimation of the total pressure, it will be required to measure the zero output value in order to take that reference pressure into account. The detailed process is provided in section 5.1.



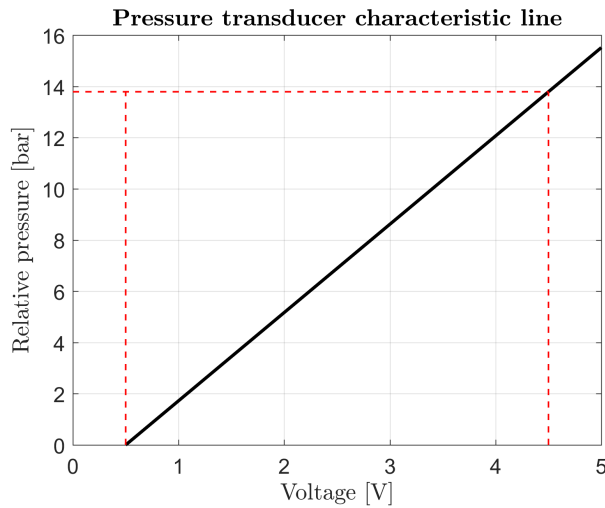


Figure 4.28: Characteristic line of the pressure transducer

## 4.7 Electric and electronic systems

### 4.7.1 Load cell and transducer electronic circuit. Analog Discovery 2

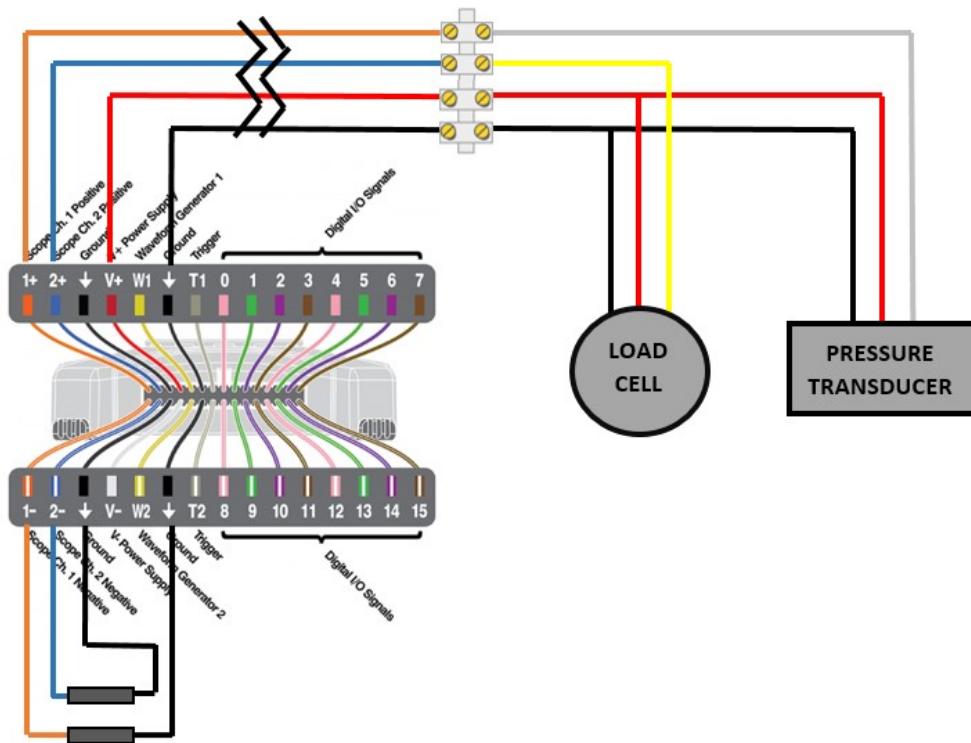


Figure 4.29: Sketch of the electronic connexions in the lab room side

In the previous project, in order to analyze the output signal of the load cell, the multi-function device Analog Discovery 2 (from now on AD2) was introduced as part of the electronic system. This is a very interesting tool that counts with two oscilloscope channels, a power supply of  $\pm 5V$ , a 16-channel digital logic analyzer, two-channel function generator and a two input/output digital trigger signals, among many other features. The potential use of this component is huge, but for the concerning case only the oscilloscope and

the power supply functions will be used. Moreover, one of the big advantages of this device is that it is USB-powered, although an external power supply can be connected so as to enhance its capabilities <sup>2</sup>.

First, let us exhibit the layout of the electronic connexions between the two sensors and the AD2, sketched in Fig. 4.29, and then, the software used by the device for the data acquisition, WaveForms 2015, will be briefly introduced.

One of the main requirements for the selection of the pressure transducer was that the power supply needed to be 5 V in order to be able to be fed by the AD2. Then, the load cell and the transducer will be connected to the same power line, as seen in Fig. 4.29, given that the total current of both sensors (of the order of 10mA) was lower than the maximum provided by the AD2 (700 mA).

The AD2, fed by the computer (located in the lab room), is connected to the rocket (located in the test room) by 4 cables: 5V power supply (shared by both sensors), ground connection (shared by both sensors), load cell output signal, and pressure transducer output signal. On the side of rocket, the electronic connexions are divided between both sensors by means of a screw terminal, as seen in Fig. 4.29.

Analogously, on the side of the AD2, the electronic connexions are made according to the pinout diagram in Fig. 4.29, taking care of closing the two oscilloscope circuits by connecting the negative terminal to ground. A picture of the real layout is shown in Fig. 4.30.

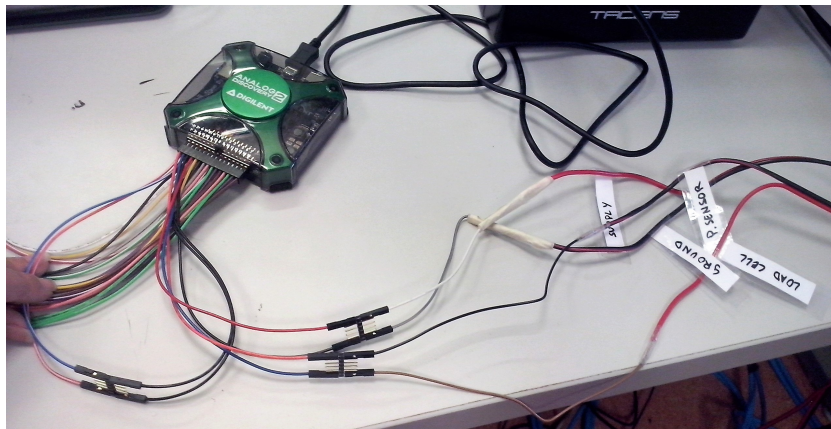


Figure 4.30: Real electronic connexions in the lab room side

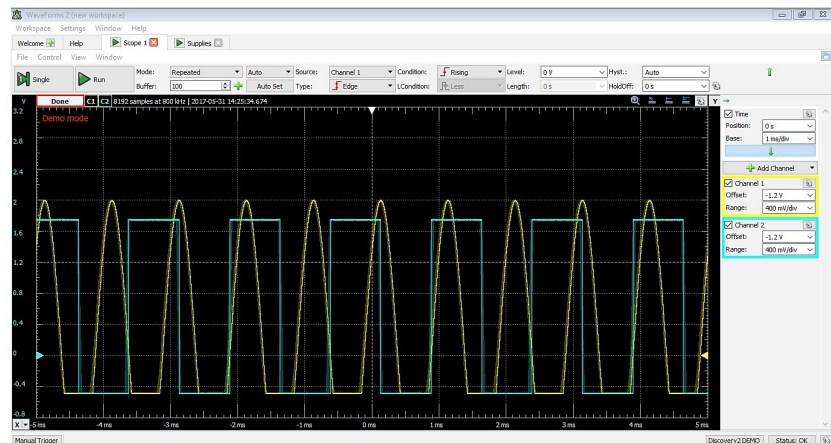


Figure 4.31: Waveforms workspace

Once the connexions layout is clear, the data acquisition software, WaveForms 2015, and the acquisition procedure will be described. This software allows to display, record and analyze the data acquired by any

<sup>2</sup>Analog Discovery 2 Datasheet is available on-line in the Digilent website:  
<https://reference.digilentinc.com/reference/instrumentation/analog-discovery-2/reference-manual>

of the input channels of the AD2. For the concerning application though, only the "Scope" and "Supplies" tools will be needed: in the "Supplies" window, one can select the desired value of the voltage supply from 0 to 5 V and switch on and off said supply; on the other hand, the "Scope" window shows and records the output signal of both oscilloscope channels, as shown in the example in fig. 4.31<sup>3</sup>:

Furthermore, it is possible to save the workspace of Waveforms to avoid having to set all the parameters on each experiment, and it is also possible to export the data file in Excel format for its subsequent treatment with other numerical or graphic softwares.

#### 4.7.2 Electric circuit: glow plug

Finally, in order to complete the description of the electrical and electronic system, it is necessary to clarify that the glow plug needs an external more powerful power supply than AD2 given that its excitation current is near 3 A.

The connections of said power supply to the glow plug in the rocket are as follows: supply terminal (red) is directly connected to the glow plug pin, and the ground terminal (black) is connected to any of the metallic parts of the rocket (preferably the guiding rods) in order to close the electric circuit.

---

<sup>3</sup>The lines represented in the screen are created by the demo mode of the AD2 just for the sake of illustration. They do not correspond to the actual reading of the load cell and pressure transducer.

# 5 Experimental tests and results

In this section, first a description of the sensors data handling regarding calibration test and zero output calculations will be provided. Afterwards, the experience and lessons learned from the two first trial firings will be discussed. Finally, in the last subsection, the experimental results from each of the 8 firings analyzed in this project will be discussed.

Nonetheless, for the sake of clarity, a brief description of the experimental procedure of the rocket firing is provided in first place.

In order to obtain a measure of the fuel mass flow rate, it is necessary to weight the PMMA cartridge before and after each firing, which implies that the thruster must be assembled and disassembled on each test. Having this in mind, and assuming that the electronic circuit of the Analog Discovery is already set up as explained in Section 4.7, the steps of the experimental procedure are listed below:

1. Weight the inner PMMA tube.
2. Assemble the selected configuration (propellant block length and nozzle diameter) of thruster.
3. Put the thruster in contact with the load cell.
4. Connect the power source terminals to the glow plug.
5. Once in the lab room, switch on the glow plug power source and the Analog discovery Voltage source.
6. Start recording the sensors readings using Waveforms software, and set up a video camera as well.
7. Start the rocket firing. Using the pneumatic regulation system on the lab room, open fully the oxygen valve. Then allow some propane flow, and when the gas mixture has ignited and the PMMA tube starts to burn, kill the propane flow and switch off the glow plug.
8. After a few seconds (8 to 10 sec), kill the oxygen flow to stop the firing, and open fully the nitrogen valve to expel the exhaust gases and cool down the thruster.
9. Stop the video recording, and regarding Waveforms, save and export the data of the sensors readings.
10. Wait until the rocket has cooled down and disassemble it.
11. Weight again the inner PMMA tube.

## 5.1 Sensors calibration and zero output voltage readings

### 5.1.1 Sensors zero output voltage reading

According to the previous sequence of steps, the sensors signal recording starts before the oxygen valve is open. Thus, the data acquired in this time lapse of a few seconds will allow to measure the zero output voltage of both sensors.

In regard to the load cell, as mentioned above and as it can be seen in Fig. 5.1, the thruster is put in contact with this device before the firing. This is done to obtain a true and precise reading of the thrust force and to avoid any possible impact damage of the load cell during the test. Therefore, the force caused by this initial contact must be discounted from the rest of the measurements.

Said contact force ( $F_{contact}$ ) is simply obtained by taking an average value of the zero output voltage obtained during those initial seconds and translating that reading into a force measure using the characteristic line of the device in Fig. 4.25.

Then, at any moment during the firing, the (absolute) force acting on the load cell ( $F_{abs}$ ) will be obtained from the characteristic line in the same way as before. However, the true measure of the thrust force provided



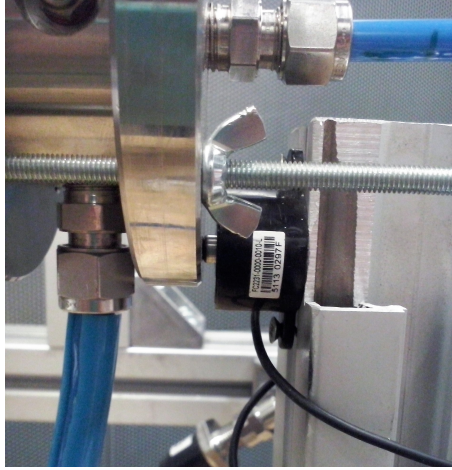


Figure 5.1: Setup of rocket position relative to the load cell

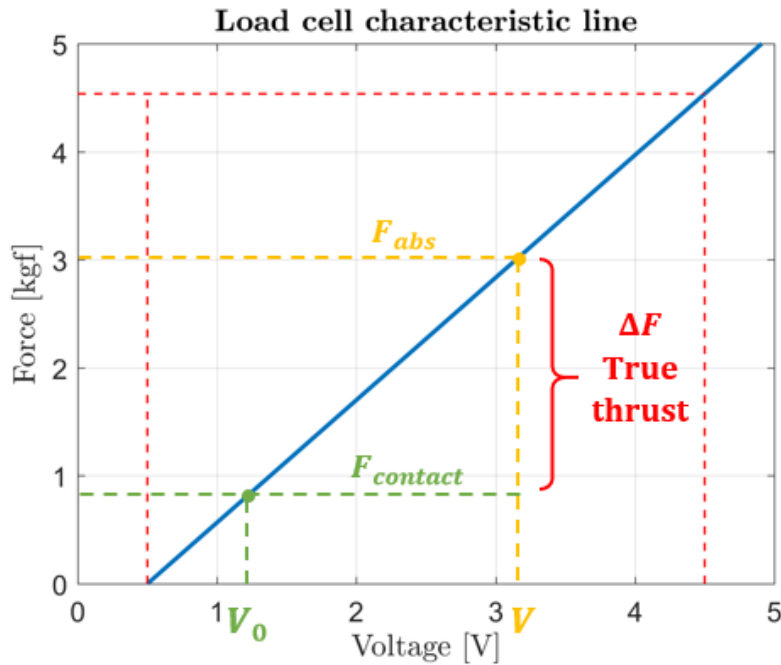


Figure 5.2: Sketch of absolute force, contact force and actual (true) thrust

by the rocket is calculated by subtracting the contact force to said absolute force, as illustrated in the sketch of Fig. 5.2:  $\Delta F_{thrust} = F_{abs} - F_{contact}$ .

With respect to the pressure transducer, since it is a sealed gauge, the zero output voltage will be 0.5 V only when the atmospheric pressure coincides with the reference atmospheric pressure in which the device was sealed, which is usually close to 1bar. Therefore, the true measured zero output voltage will allow to determine that reference pressure ( $P_{ref}$ ) from the ambient local pressure ( $P_{amb}$ ).

Analogously to the load cell calculation, an average value of the transducer voltage reading during the initial seconds of the recording is used as the input to the device characteristic line (Fig. 4.28) so as to obtain the corresponding value of the relative pressure ( $\Delta P_{rel,ini}$ ). Before opening the oxygen valve to start the firing, the reading of the transducer will correspond to the ambient atmospheric pressure. Then, the reference atmospheric pressure of the sealed gauge is obtained as:  $P_{ref} = P_{amb} - \Delta P_{rel,ini}$ , where  $\Delta P_{rel,ini}$  is positive when  $P_{amb} \geq P_{ref}$  and negative when  $P_{amb} \leq P_{ref}$ . In the concerning case, the reference pressure was found to be 0.9973bar.

Finally, once  $P_{ref}$  is determined, to obtain the absolute pressure at any instant of the firing,  $t$ , one only needs to obtain the corresponding relative pressure from the characteristic line and add up the value of the reference pressure:  $P_{abs} = \Delta P_{rel,t} + P_{ref}$ . An important remark is that, since the transducer is hermetically sealed, the reference pressure is fixed and therefore, the previous calculation process for  $P_{ref}$  is only needed to be performed once.

### 5.1.2 Load cell calibration

Although it was not necessary, in order to corroborate the load cell characteristic line given by the specifications, a calibration test was carried out.

With the assembly already in contact with the load cell, the calibration procedure consisted in applying a force to the rocket against the sensor and measure it by means of an analog dynamometer. This test was performed for several values of force (0, 0.5, 1, 1.5 and 2 kgf), which were maintained during a few seconds. The resulting voltage reading from the load cell is presented in Fig. 5.3.

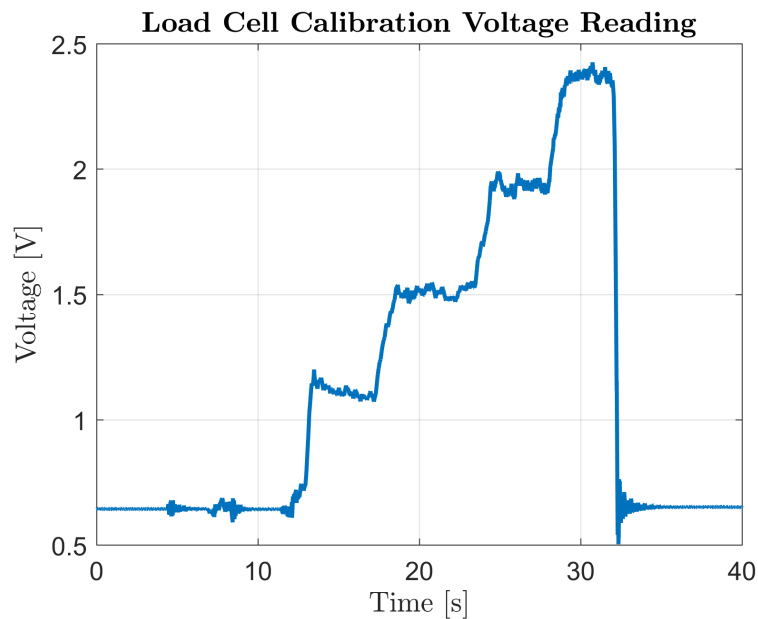


Figure 5.3: Load cell calibration test voltage reading

Since the calibration was performed manually, as it is clear from the previous plot, the voltage reading reflects some degree of oscillation of the force. For this reason, an average voltage value was calculated for each of the time intervals in which the signal was more or less stabilized.

Then, five average voltage values for each of the previous force magnitudes were obtained: 0.64, 1.11, 1.51, 1.93 and 2.37 V. From this 5 data points an average slope was calculated, represented in Fig. 5.4 together with the original characteristic line for the load cell specifications.

From the graph it is visible that the difference between the two lines is minimal, and since the calibration procedure implied a significant human factor, it was decided to select the specifications characteristic line as the true one, to be used for the rest of the firings.

## 5.2 First two trial firings

Since there were several new components and modifications introduced in this project, it was decided to perform a couple of trial firings in order to check that all the elements were functioning correctly. The analysis of these two tests was merely qualitative, however, a few relevant conclusions were obtained.

In both cases the selected configuration of the thruster assembly was the 4mm diameter nozzle and the

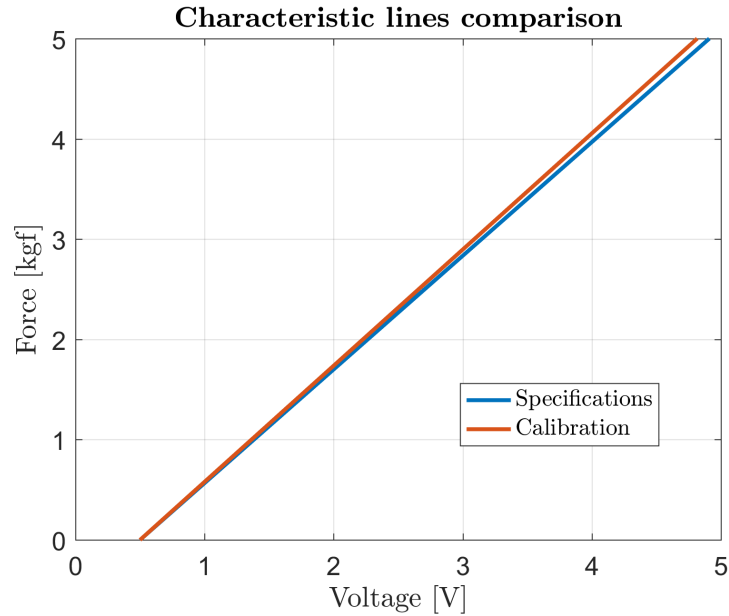


Figure 5.4: Comparison between the load cell characteristic lines from the calibration and from the specifications

long propellant block (210 and 200 mm for the inner and outer tubes, respectively).

On the bright side, successful readings from the two sensors were obtained. This fact was of extreme importance given that they were crucial for a proper analysis of the rocket performance. In particular, regarding the pressure transducer, it was concluded that the pneumatic installation and the electronic connections were carried out correctly and that the new device itself was operating properly. With respect to the successful load cell reading, it is of extreme relevance given that this was the first time that an actual measure of the load cell was acquired. From this data collection, one could state that the new structure of battering ram configuration was fulfilling its mission since no friction force was appreciated, and also that the sensor was providing correct measurements.

Nevertheless, some problems were encountered in this process. On one hand, it was noticed that both sensors' readings were fairly low, against previous expectations. However, since that information was not recorded at the time, no further analysis could be performed in this regard.

On the other hand, and most importantly, some serious problems were encountered regarding the integrity of the nitrogen gas connection to the cold block. In both trials, after a few seconds of operation, the polyurethane tube of the nitrogen gas melted down very close to the stainless steel compression fitting that joined the tube to the Piece 1 of the cold block (see Fig. 4.6 for reference). This failure also took place in some of the subsequent monitored experiments as it will be detailed in the next subsection.

The ultimate cause of this problem is still uncertain, nonetheless the best speculative reasoning achieved is based on the combined action of the combustion reaction initiation in the cold block and the high pressure reached in the combustion chamber during the firing: the nitrogen orifice was located in the top part of Piece 1, therefore this could provoke that the first flame created in the cold block traveled momentarily upstream the nitrogen gas line weakening the tube walls and making it more prone to bursting; then, the high pressure achieved in the chamber pressure due to the small nozzle throat area could finally cause the failure of said component.

Finally, another important outcome of these two tests was the creation of a check list. Given the numerous steps needed for the rocket setup, data acquisition and the rocket firing itself, it was decided to comprise all of them in a check list so as to avoid skipping any step. Said check list, which is mostly an extended and detailed version of the experimental process description provided at the beginning of this section, is available in the Appendix.

### 5.3 Results of the subsequent monitored firings

Apart from the two trials, 8 experiments were monitored and analyzed for different combinations of PMMA tubes length and nozzle throat diameter, as well as the pressure of the oxygen gas tank. This data together with the ambient conditions<sup>1</sup> and fuel cartridge initial and final mass, are represented in table 5.1.

EXPERIMENT	1	2	3	4	5	6	7	8
Inner tube L (mm)	210	210	210	210	210	210	150	150
Nozzle throat D (mm)	9.5	6	4	6	6	4	6	4
Oxygen tank P (bar)	6	6	6	9	9	9	6	6
Ambient T (°C)	17	17	17	28	28	28	23	23
Ambient P (bar)	0.948	0.948	0.948	0.943	0.943	0.943	0.947	0.947
Initial fuel mass (g)	89.7	79.2	70.2	91.4	82.9	69.1	68.1	60.4
Final fuel mass (g)	79.2	70.2	64.5	82.9	69.1	63.2	60.4	50.9

Table 5.1: Configuration and atmospheric data for each experiment

First of all, it is important to mention the overall outcome of each experiment: the tests 1, 2, 5, 7 and 8 were successfully completed; test 3 was also successful but the firing time was rather short and the rocket did not reach steady conditions; finally, in tests 4 and 6, the nitrogen tube melted down as in the two trial experiments, and consequently, steady conditions could not be reached either. Additionally, in case 6, the fuel line also melted down and the glow plug fused (for the first and only time).

A deeper analysis of each experiment was then achieved from the sensors data. The two voltage readings from the pressure transducer and the load cell were translated, respectively, into a measure of **absolute** oxygen pressure<sup>2</sup> ( $P_{abs} = \Delta P_{rel,t} + P_{ref}$ ) and **true** thrust ( $\Delta F_{thrust} = F_{abs} - F_{contact}$ ). The corresponding graphs are presented in Fig. 5.5, where the complete series of samples have been reduced to the time interval of interest.

In order to comment the behavior of the curves in these plots, they will be split in three intervals: 1) from the beginning to the abrupt peak that indicates the initiation of the combustion in the cold block, 2) from that peak to the following maximum point of the curves, just before the rocket is stopped, and 3) from that point to the end of the data series.

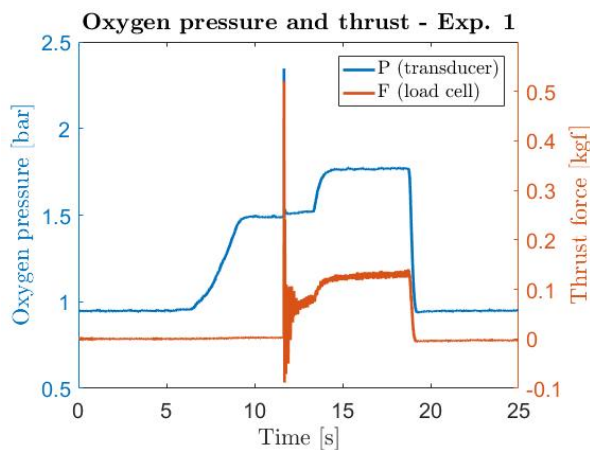
1. As it can be seen in Fig. 5.5, up to the initiation of the combustion, all the graphs are alike: the pressure reading starts to increase as the oxygen valve is open. In some cases (Exp. 2, 4 and 7), this increment is performed in two steps due to the fact the the oxygen valve is opened in two movements.

On the other hand, the only action of the oxygen flow through the nozzle provokes certain thrust force as the gas is accelerated, which can be noticed from the slight raise of the force signal coincident with said pressure increase. This fact is clearly visible in cases 3 and 6, in which the nozzle with the smallest throat was used, but it can also be observed at a minor scale in the rest of experiments, except for case 1, in which the extremely large nozzle throat barely restricts the oxygen flow, and case 5 for which the axis scale is too large to be able to notice this aspect.

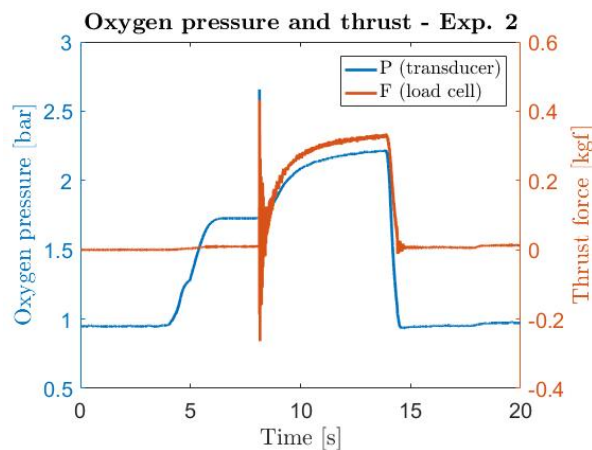
Regarding the pressure reading magnitude, in experiments 4, 5 and 6 the calibrated oxygen hole is clearly choked ( $P_0 > P_{crit} \approx 1.8bar$ ) given that the oxygen tank pressure was raised to 9 bar, and in the experiment 1 is clearly below sonic conditions due to the large diameter of the nozzle. The rest of the cases are very near to this critical pressure. Nonetheless, the values are so close that any uncertainty on the atmospheric pressure and any error in the approximation between static and stagnation pressure can signify the difference between reaching or not sonic conditions.

<sup>1</sup>Atmospheric temperature and pressure data obtained from: <https://www.worldmeteo.info/es/europa/espana/leganes/tiempo-104754/>

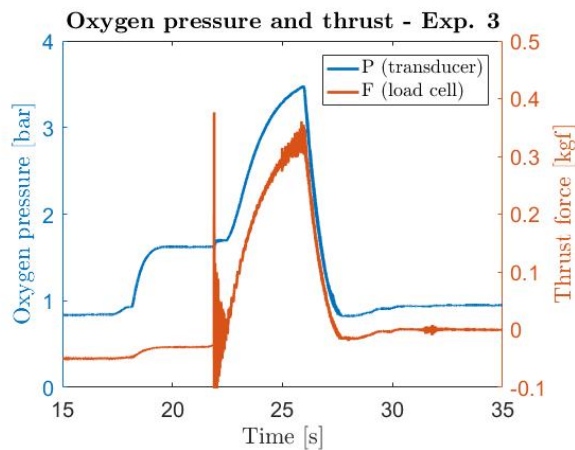
<sup>2</sup>"Absolute" here must be understood as "not relative to the local atmospheric pressure". However, this is a measure of the static oxygen pressure in the tube upstream of the calibrated hole. The transformation to stagnation pressure is not relevant at this point since the difference is very small and the concerning analysis aims to compare the different experiments between them. In the next section though, said transformation would be performed so as to achieve a more truthful comparison with the theoretical 1D model.



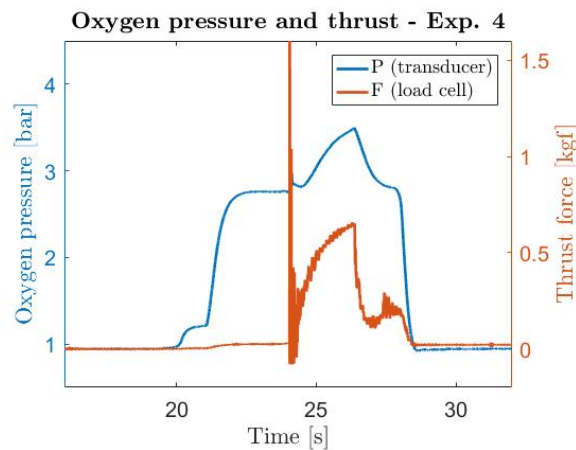
(a) Experiment 1



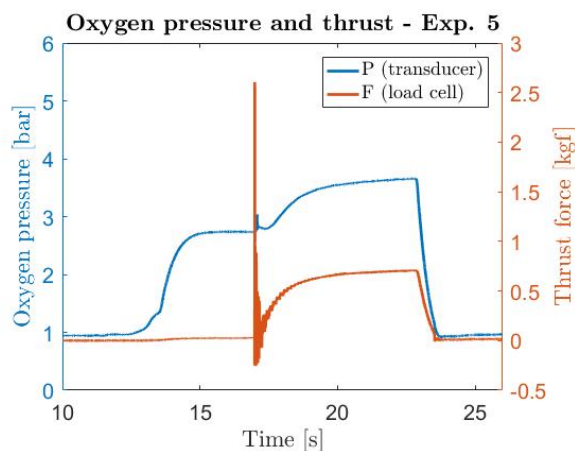
(b) Experiment 2



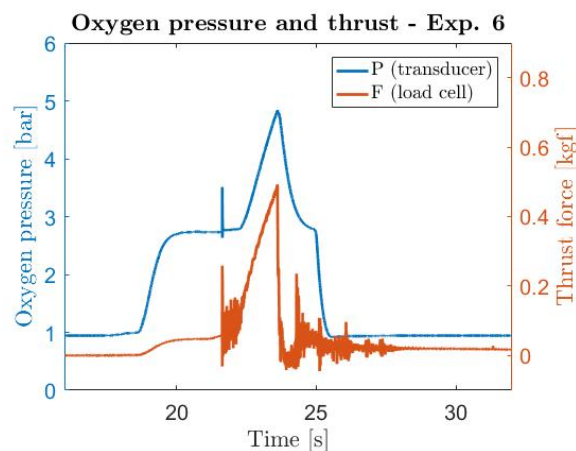
(c) Experiment 3



(d) Experiment 4



(e) Experiment 5



(f) Experiment 6

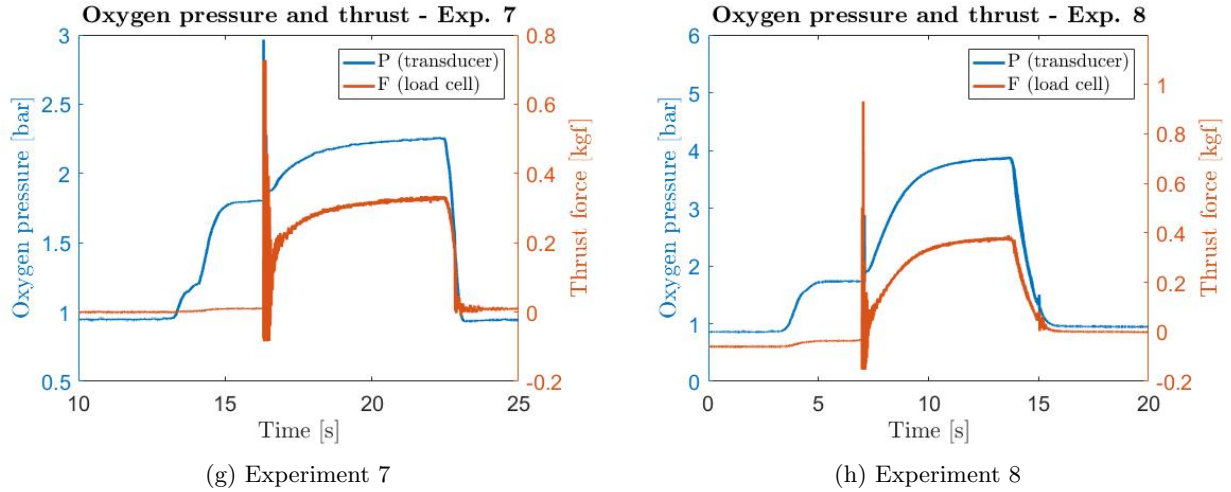


Figure 5.5: Transducer pressure readings and load cell thrust readings

- In the second interval, which coincides with the duration of the firing itself, the first aspect to notice is that the operation regime is highly transient given that it takes a long time for the signals to stabilize. In fact, it was expected that the transient interval was shorter for higher chamber pressure, nonetheless, from the mutual comparison of the two last tests, it is clear that it is not fulfilled. This complex behavior could be explained through the ballistics of the rocket: maybe the fact of reaching a higher pressure implies a complex transitional fluid field or heat transfer that hampers the combustion reaction during this transitional regime.

From the comparison of the previous tests, the resemblance between the cases 1, 2, 5, 7 and 8 can be easily appreciated, given that in all of them a fairly steady operation is reached.

The significant peak produced by the first flame is followed by a very brief oscillatory behavior of both signals, as it can be expected. This seems to be caused by the long thermal characteristic time of the system: a long time interval is necessary for the assembly to warm up and work in an approximated steady regime.

An interesting fact though, is that during the firing, the pressure reading raises as the thrust reading does so. This implies that the increment in the chamber pressure is affecting the oxygen flow. Hence, one can deduce that the calibrated orifice of the oxygen is not choked during the firing, even in cases 4, 5 and 6 in which the hole was clearly choked before ignition.

Case 3 is also quite similar to the previous, but due to fear regarding a potential failure of the nitrogen line, as it happened in the two trials, the firing was cut out before reaching steady conditions.

In the cases of experiments 4 and 6, they did not reach the steady conditions due to said failure of the nitrogen line. Nonetheless, their graphs (up to second 27 in case 4 and up to second 24 in case 6) show a raise of both sensors readings similar to the rest of the cases. The failure in case 4 was due to the previous severe deterioration of the tube (it was swollen) produced in the third test. In the test 6, the failure was believed to be caused by the significantly high pressure reached in the combustion chamber from the combined action of the high tank pressure at 9 bar and the smallest nozzle throat area available.

- Finally for the stopping phase, tests 1, 2, 3, 5, 7 and 8 show a steep decay of both signals, provoked by the closing of the oxygen valve. Nevertheless, in cases 4 and 6, this fall is produced in 2 steps. The first step represents the reaction time between the failure of the nitrogen line (maximum point) and the closing of the oxygen valve (corner point), time during which the exhaust gases of the combustion reaction (still ongoing) escaped through the orifice of the melted tube. Then, once the oxygen valve is closed, the signals show a steep fall analogous to the rest of experiments.

It must be noticed that, in cases 3 and 8 the load cell reading before and after the firing do not coincide (the latter is slightly higher). A valid explanation for this is that there was some displacement of the hooks that sustained the assembly along the aluminum profile in which they were embedded. Therefore, in the future it may be convenient to drill the hooks to the profile. To counteract this fact, in this two cases

the calculation of the zero voltage output of both sensors will be performed taking the last seconds of the recording instead of the initial ones<sup>3</sup>.

Finally, some remarks will be pointed out regarding the handling of this experimental data for its subsequent comparison with the theoretical model in the next section:

- On one hand, in order to calculate the fuel mass flow rate, it is necessary to determine a meaningful burning time for which a more or less steady fuel consumption is expected. Hence, the few instants between the combustion initiation peak and the raise of the sensor signals are discarded.

In fact the criterion used for the calculation of the burning time is the following: for the pressure transducer signal (given that the one of the load cell shows more degree of oscillation), the minimum and maximum pressure values inside the firing interval are selected (in red); then, the average value between those two is calculated (in orange); finally, the time instant corresponding to that average pressure value will be taken as the beginning of the burning process (in green), and the last instant will simply correspond to the higher point of the curve before the steep fall. For a clearer explanation refer to Fig.5.6.

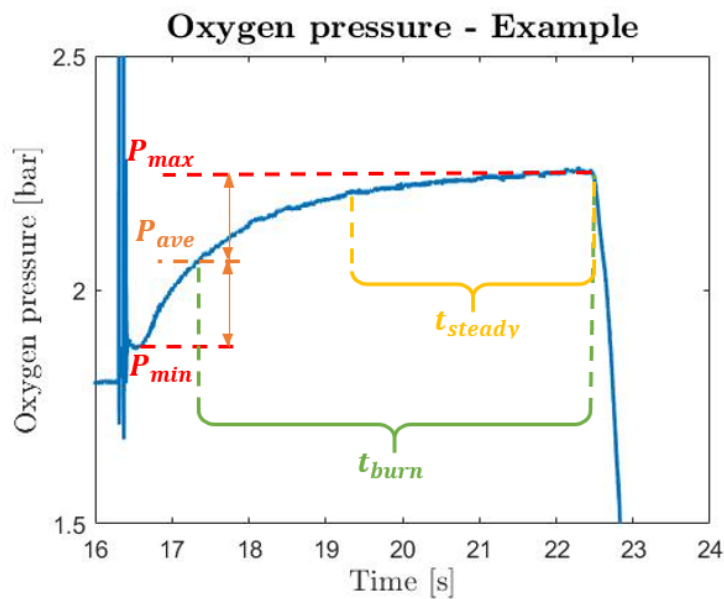


Figure 5.6: Burning time calculation

- Nevertheless, for the readings comparison with the theoretical model, one is only interested in the steady part of the burning, since the steady operation is one of the most important assumptions of the 1D model. Therefore, this time interval (in yellow in Fig.5.6) is selected based of the curvature of the line, being always shorter than the burning time of before.

Moreover, given that the operation is assumed steady, for the sake of simplicity, an average value of pressure and thrust within these 2-3 seconds of steady burn will be computed. Nevertheless, for cases 3, 4 and 6 in which the steady conditions are not achieved, only the last instants (several tenths of seconds to reduce the impact of the signals oscillations) will be averaged.

<sup>3</sup>Measure already implemented in fig. 5.5

## 6 Discussion of results

First of all, it must be mentioned that this is the first project of the UC3M hybrid rocket in which meaningful theoretical and experimental results have been reached thanks to the obtaining of a feasible measure of the thrust force.

### 6.1 Implementation procedure in Matlab software

The numerical resolution of the problem has been performed using Matlab software. A single script was built for the analysis of all the 8 experiments: the user was asked to input the number of the experiment to be analyzed, and then, the computations were performed for that individual case.

Said script can be divided in six main parts:

1. **Data input:** the common data to all the experiments was simply introduced as variables. Nonetheless, the individual data of each experiment was arranged in a data matrix.
2. **Experiment number selection:** once the user has input the number of the experiment, the corresponding data is obtained from the previous matrix. Additionally, the name of the computer file that contains the series of voltage readings obtained from Waveforms is specified.
3. **Importation of the sensors readings:** the data from Waveforms is imported using a separate Matlab function. At this point, the zero output voltage values for relative oxygen pressure and rocket contact force are calculated according to Section 5.1. Additionally, the burning time calculation is performed.
4. **Creation of a plot with the sensors outcome:** the graphs included in Fig. 5.5 are constructed according to the explanation provided in the previous section.
5. **Calculation of the theoretical thrust:** first, the average of the values for the steady interval is calculated and then, the theoretical study is performed graphically according to the process described in section 3. The oxygen mass flow graph is also constructed in this part.
6. **Comparison between the experimental and theoretical thrust:** creation of a comparative plot including the previous results of the theoretical thrust, as well as the outcome from the load cell reading.

Finally, it must be mentioned that two additional Matlab functions were created: one for the calculation of  $\kappa_{ox}$  from the ambient temperature, and the second one to calculate the properties of the exhaust combustion gases from the chamber temperature and O/F ratio. Additionally, other two separate scripts were used for the nozzle design calculation and the sensors calibration procedure.

### 6.2 Correlation between experimental and theoretical results

This section is divided in four subsections: in the first one, a detailed analysis of the theoretical solution as well as its comparison with the empirical data will be performed for experiment 1, to serve as a guide for the rest of experiments; in the second section, an analogous more general discussion will be performed for each of the remaining tests individually; in the third subsection a parametric analysis will be performed to compare the results of the experiments between them; finally, in the fourth section the calculation of the regression rate of the rocket according to eq. 3.1 would be briefly included.



• **Juxtaposition of theoretical vs. empirical results for Test 1**

The most important conclusion from the theoretical 1D model Section is that a higher chamber pressure, on one hand, restricts the oxygen flow of the calibrated orifice, and on the other hand, instigates the mass flow of the exhaust gases through the nozzle. Therefore, the steady solution will be reached when both mass flows are compatible with the equation:  $\dot{m}_T = \dot{m}_{ox} + \dot{m}_f$ .

According to this, the theoretical solution of the oxygen mass flow rate can be found graphically as the intersection between the curve of  $\dot{m}_{ox,h}$  as given by the analysis of the calibrated orifice (represented in blue in the following graphs) and the curve of  $\dot{m}_{ox,n}$  as given by the analysis of the nozzle throat (represented in orange).

Another important conclusion from the theoretical section is that, whereas the calculation of  $\dot{m}_{ox}$  as given by the calibrated orifice is completely defined as a function of the chamber pressure,  $\dot{m}_{ox}$  as given by the nozzle analysis incorporates the uncertainty of the chamber temperature.

Having this in mind, a comparison between the theoretical model and the empirical data will be performed at a deep level for Experiment 1, given that it was the most steady case. For this test, the graph showing the theoretical solution of  $\dot{m}_{ox}$  is represented in Fig. 6.1.

It is important to notice that, for all the tests, the curves are represented only for values of the chamber pressure contained in the range between the ambient pressure and the oxygen line stagnation pressure:  $P_c \in [P_{amb}, P_0]$ . As an example, these two limits will be represented (purple vertical dashed lines) for Experiment 1 only (Fig. 6.1).

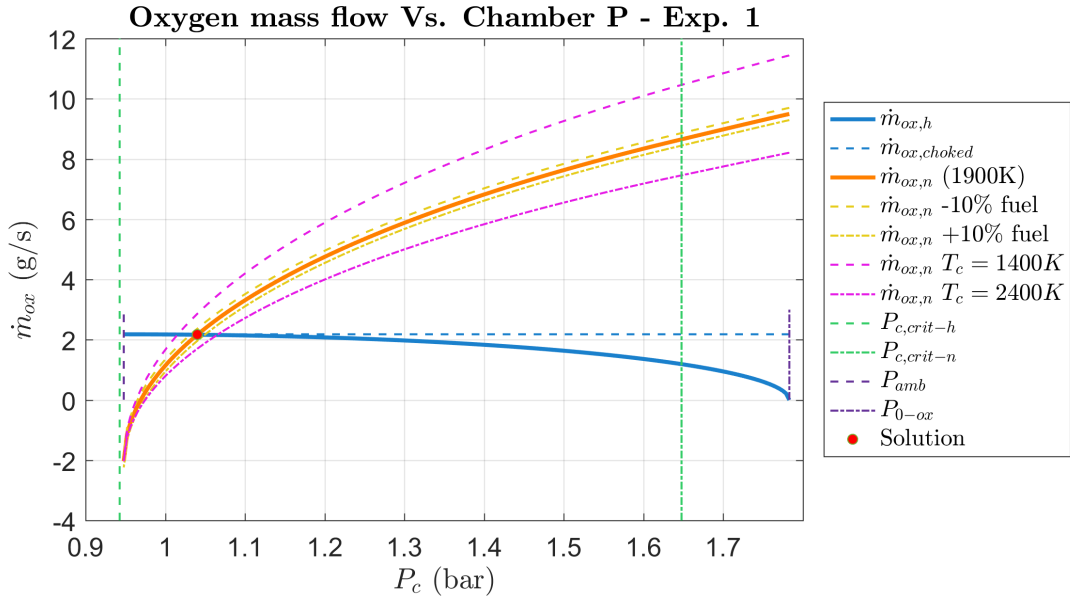


Figure 6.1: Theoretical oxygen mass flow solution for Experiment 1

As it can be seen in the graph, as  $P_c$  increases, the  $\dot{m}_{ox,h}$  as given by the calibrated orifice (blue solid line) decreases, reaching the zero value when there is no pressure difference between upstream and downstream the orifice, as expected from eq. 3.4 and Fig. 3.3.

Regarding choking conditions at the calibrated orifice, they are only reached when the chamber pressure is small enough to achieve the critical pressure ratio. Although the proximity between the solid and dashed blue lines may be confusing, the calibrated orifice is never choked in this case since the hypothetical critical pressure ( $P_{c,crit-h} \approx 0.95bar$ , represented in green) is smaller than the minimum possible value of the chamber pressure ( $P_{c,min} = P_{amb} > 0.95bar$ ), and this is not physically possible.

On the other hand, with respect to  $\dot{m}_{ox,n}$  as given by the nozzle (orange line), initially there is no mass flow since there is no pressure difference between the chamber and the ambient. Theoretically, for  $P_c = P_{amb}$ ,  $\dot{m}_{ox,N}$  should be zero, but not negative as shown in the graph. This incongruence is due to the inaccurate estimation of the fuel mass flow rate as  $\dot{m}_f = (m_{f,ini} - m_{f,end})/t_{burn}$ , which implies that the fuel

consumption is independent on the chamber conditions. Consequently, only the values of  $\dot{m}_{ox,n} \geq 0$  have a physical meaning.

Then, as the chamber pressure raises,  $\dot{m}_{ox,N}$  also increases, as predicted in the sketch 3.4. Once the critical chamber pressure is reached ( $P_{c,crit-n} \approx 1.65bar$ , also in green), the behavior of  $\dot{m}_{ox,N}$  is proportional to  $P_c$ . This is easily explained from eq. 3.11: for choking conditions,  $M_t = 1$  and therefore, the slope of the line becomes constant for a fixed value of the chamber temperature.

In regard to the chamber temperature, given that this is the only parameter for which no empirical data was available, several trial values have been assigned based on the PMMA flame temperature at ambient conditions, as mentioned in the theoretical section of this report. For the sake of clarity, only three values of the temperature (1400K and 2400K as the extremes of the range, and 1900K as the mean temperature) will be represented in the graphs of this section. From their analysis in Fig. 6.1 (pink dashed lines), it can be concluded that a higher  $T_c$  leads to a smaller  $\dot{m}_{ox,N}$ . This is again explained from eq. 3.11, from which one reads that  $\dot{m}_{ox,N} \propto 1/\sqrt{T_c}$ . Hence, a higher temperature implies a lower slope of the curve:  $\dot{m}_{ox,N}Vs.P_c$  (curve shifted down and to the right), and consequently, the solution for  $\dot{m}_{ox}$  (i.e. intersection point between the blue and orange lines) takes place at a higher chamber pressure. This is meaningful since the combustion reaction at higher pressure leads to a higher adiabatic temperature, which in turn further raises the chamber pressure, restricting the oxygen flow in the orifice.

Moreover, being aware of the uncertainty of the fuel mass flow rate estimation, two additional lines have been represented accounting for a deviation of a  $\pm 10\%$  of  $\dot{m}_f$  (represented in yellow). This difference in  $\dot{m}_f$  implies a vertical shift of the  $\dot{m}_{ox,N}$  curve: if  $\dot{m}_f$  increases, for a fixed  $\dot{m}_T (= \dot{m}_{ox} + \dot{m}_f)$ ,  $\dot{m}_{ox,N}$  has to be smaller (curve shifted down), and vice versa. As a consequence of this vertical shift, the solution for  $\dot{m}_{ox,N}$  (i.e. intersection point between the blue and orange lines) is different: if the curve is shifted downwards, the intersection point takes place at a higher chamber temperature. This agrees with the logic, since a higher chamber pressure would ultimately result in a higher fuel consumption.

Finally, on the last part of this subsection, the comparison between the experimental and theoretical results of the rocket thrust force will be analyzed.

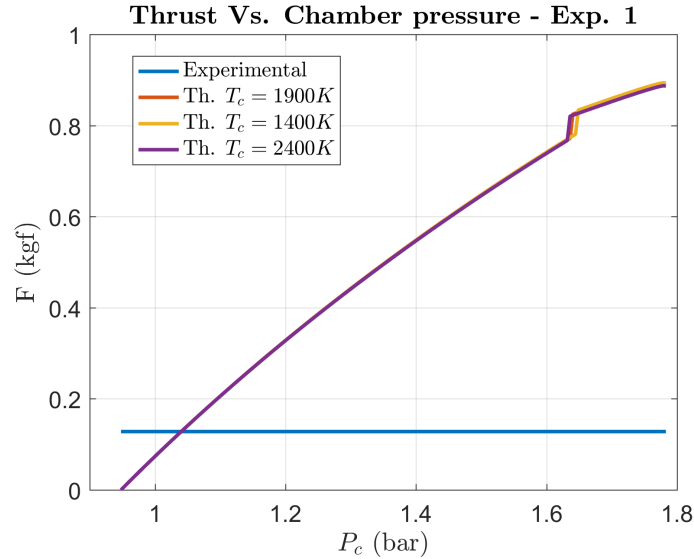


Figure 6.2: Theoretical and experimental thrust force for Experiment 1

Regarding the theoretical calculation, according to eq. 3.24, the only uncertainty in this case is given by the temperature. Nevertheless, as aforementioned in Section 3:  $F_{th} \propto \dot{m}_T \sqrt{T_c} \propto 1/\sqrt{T_c} \cdot \sqrt{T_c}$ , so one concluded that the only dependence of  $F_{th}$  on the temperature was indirectly given by the properties of the exhaust gases of the combustion. This fact is corroborated by Fig. 6.2, in which the three curves for 1400, 1900 and 2400 K are almost coincident. In fact, for the rest of experiments only the thrust case correspondent to the mean temperature of 1900 K will be represented.

Another interesting fact from the curve of the theoretical thrust is the point in which the nozzle throat becomes choked, correspondent to the abrupt step of the line at  $P_{c,crit-n} \approx 1.64bar$ . For values of  $P_c >$

$P_{c,crit-n}$ , the theoretical thrust becomes proportional to the chamber pressure given that:  $F_{th} \propto \dot{m}_T$  (and for choking conditions:  $\dot{m}_T \propto P_c$ ), and also due to the additional term of the thrust  $((P_c - P_{amb})A_t)$  which is proportional to the chamber pressure as well.

Regarding the line of the load cell thrust force, given that steady operation was assumed, a unique value of the force was obtained as the average of the steady time interval. Therefore, the cutting point between the two lines will provide a measure of the steady chamber pressure.

This fact has an big significance since, consequently, one can further determine the uncertainty of the chamber temperature<sup>1</sup> in the previous graph of  $\dot{m}_{ox}$ : the intersection between the curve of  $\dot{m}_{ox,H}$  as given by the orifice (blue line) and the value of  $P_c$  obtained from the thrust plot, lies within the uncertainty range of  $T_c$ , and results in a value of approximately 1900K, which is indeed within the nominal temperature range.

For this case of test 1, this good agreement between the theoretical and the experimental results was indeed expected given that the steady conditions are completely reached. This may not be the case for the rest of experiments, nevertheless, this previous analysis will be repeated in an identical manner to study how the theoretical model adjusts to the real data.

### • Juxtaposition of theoretical vs. empirical results for the rest of experiments

For the study of the remaining cases, their corresponding graphs for the oxygen mass flow rate and the thrust force will be discussed next. For the sake of clarity, the legend of the oxygen mass flow graphs, which is common to all the experiments, will be provided separately in Fig. 6.3.

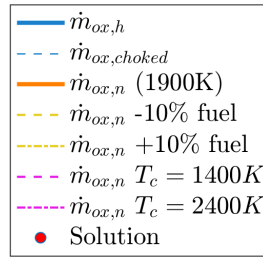


Figure 6.3: Legend for the following graphs of the theoretical oxygen mass flow

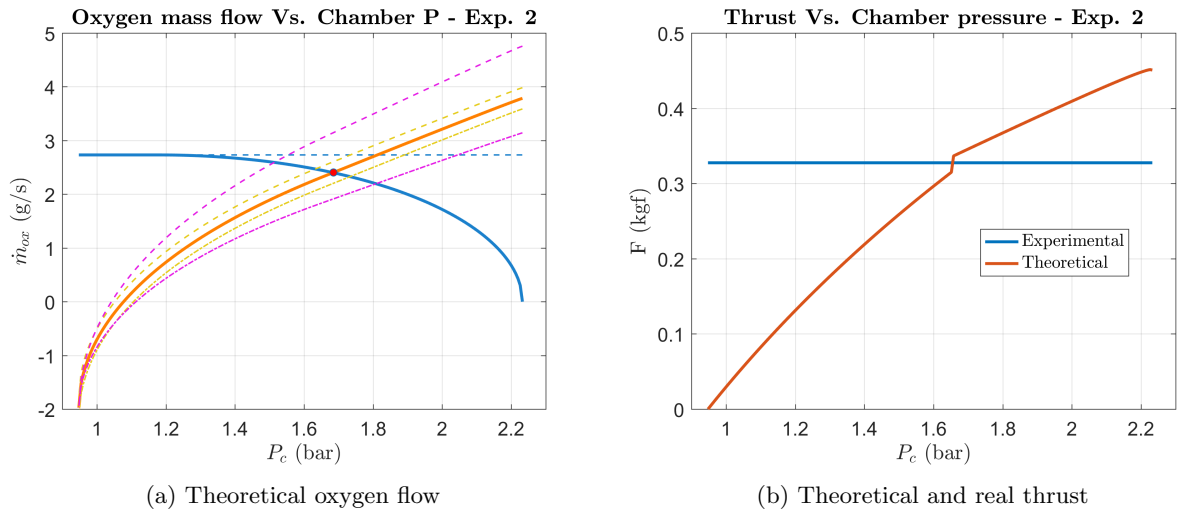
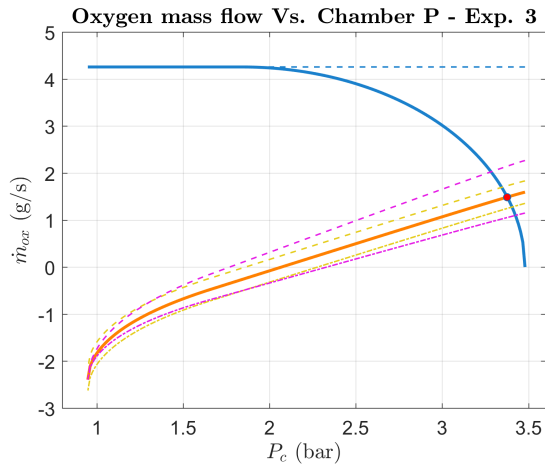


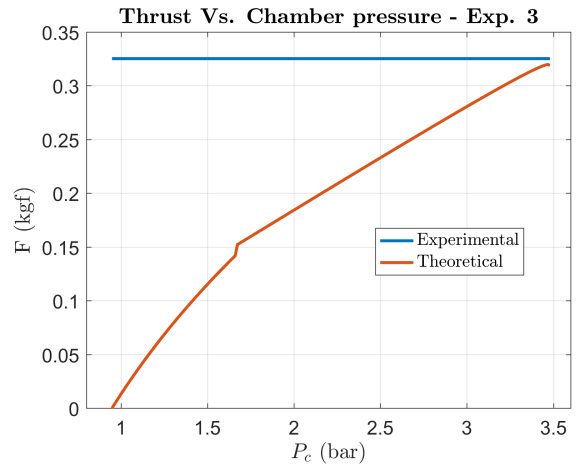
Figure 6.4: Experiment 2 results

Following the same procedure as for case 1, the results found for the theoretical oxygen mass flow for each test (i.e. mass flow graph only) are summarized in the table 6.1.

<sup>1</sup>For nominal fuel mass flow rate.

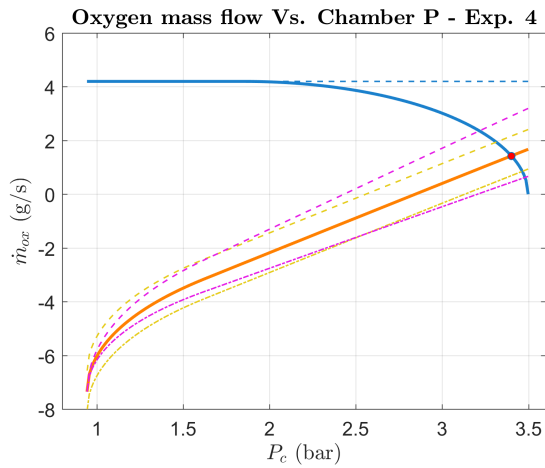


(a) Theoretical oxygen flow

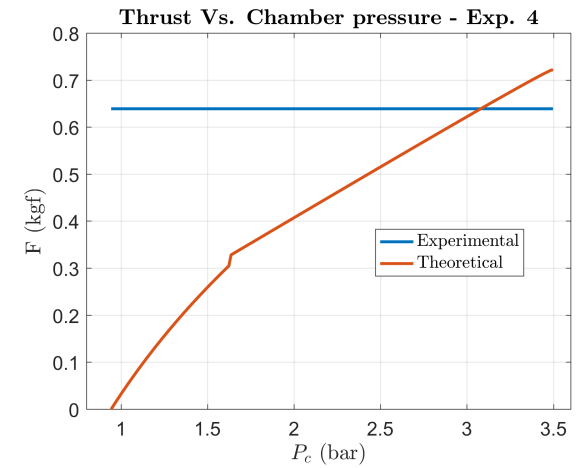


(b) Theoretical and real thrust

Figure 6.5: Experiment 3 results

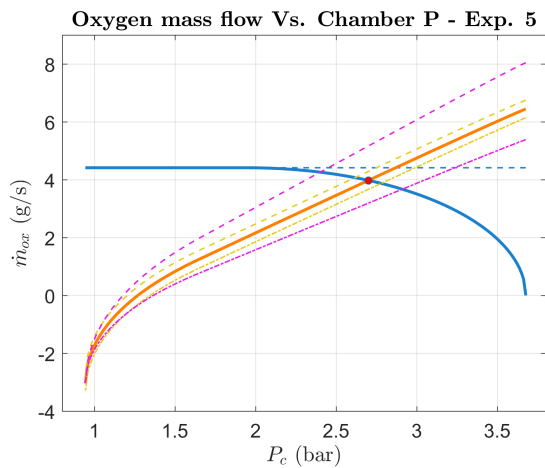


(a) Theoretical oxygen flow

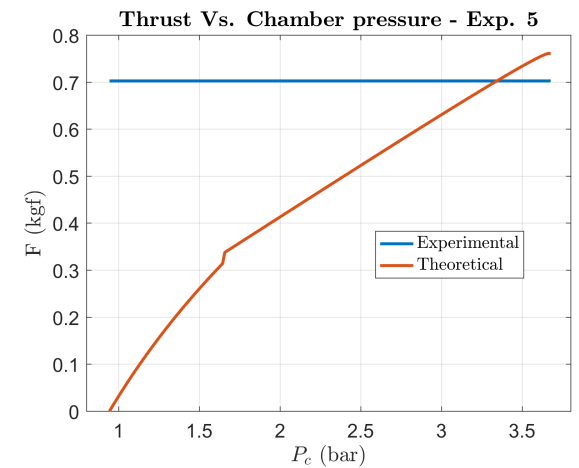


(b) Theoretical and real thrust

Figure 6.6: Experiment 4 results

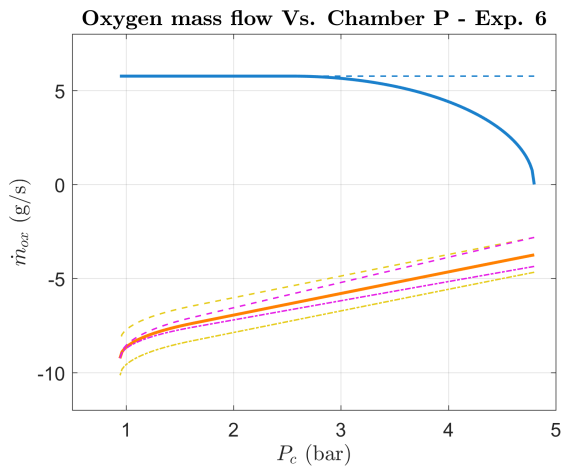


(a) Theoretical oxygen flow

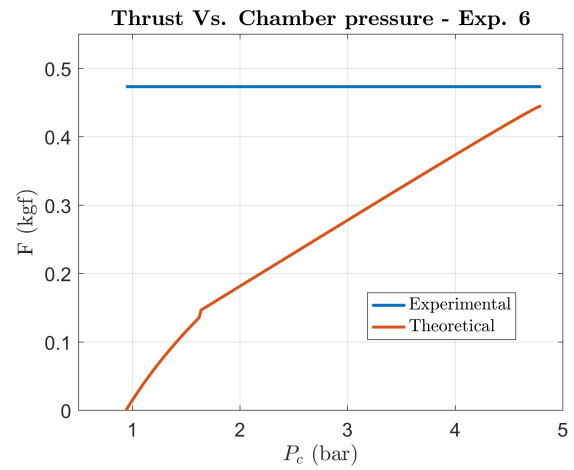


(b) Theoretical and real thrust

Figure 6.7: Experiment 5 results

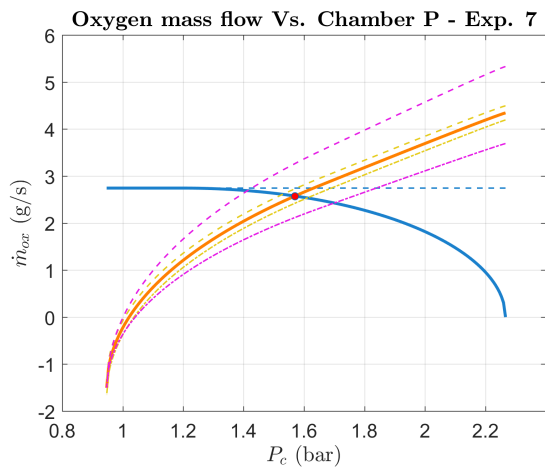


(a) Theoretical oxygen flow

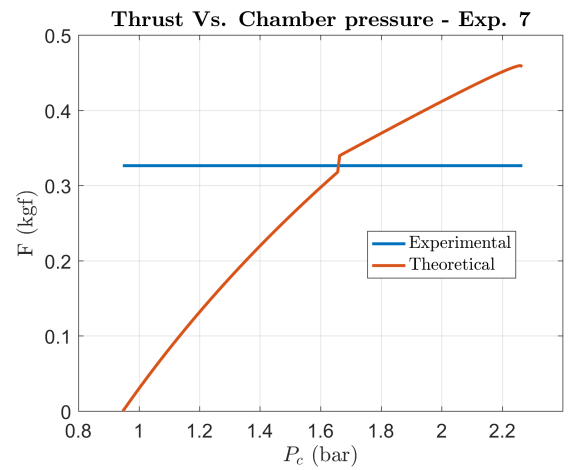


(b) Theoretical and real thrust

Figure 6.8: Experiment 6 results

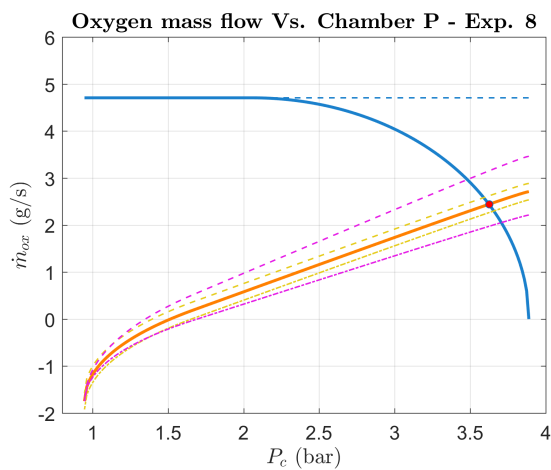


(a) Theoretical oxygen flow

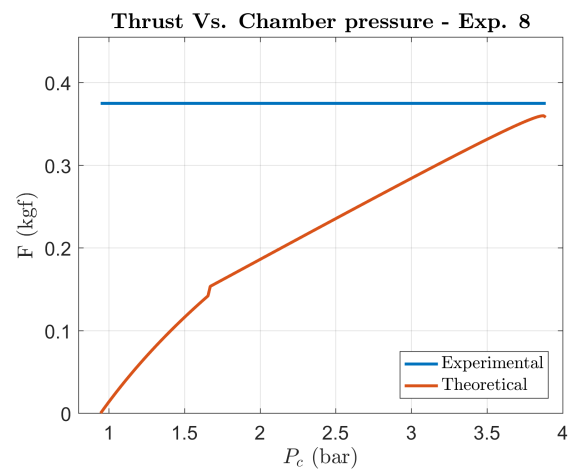


(b) Theoretical and real thrust

Figure 6.9: Experiment 7 results



(a) Theoretical oxygen flow



(b) Theoretical and real thrust

Figure 6.10: Experiment 8 results

EXPERIMENT	1	2	3	4	5	6	7	8
Steady regime?	Yes	Yes	No	No	Yes	No	Yes	Yes
$\dot{m}_{ox}(T_{mean})$ (g/s)	2.17	2.40	1.49	1.43	3.98	No sol.	2.57	2.44
$P_c(T_{mean})$ (bar)	1.04	1.69	3.38	3.40	2.70	-	1.57	3.62
$\dot{m}_{ox}$ range (g/s)	[2.15-2.17]	[2.19-2.59]	[1.10-2.03]	[0.62-2.36]	[3.67-4.26]	[-]	[2.43-2.69]	[2.05-2.97]
$P_c$ range (bar)	[1.01-1.07]	[1.52-1.81]	[3.28-3.42]	[3.22-3.48]	[2.40-2.91]	[-]	[1.41-1.70]	[3.48-3.71]
$P_{c,crit-h}$ (bar)	0.94	1.18	1.84	1.85	1.94	2.54	1.20	2.06
Choked orifice?	No	No	No	No	No	-	No	No
$P_{c,crit-n}$ (bar)	1.65	1.66	1.66	1.63	1.65	1.63	1.66	1.67
Choked nozzle?	No	Yes	Yes	Yes	Yes	-	No	Yes
$P_0$ (bar)	1.78	2.23	3.48	3.50	3.68	4.80	2.27	3.89

Table 6.1: Results obtained from the  $\dot{m}_{ox}$  Vs.  $P_c$  graph

With respect to table 6.1, the first part contains the data from the oxygen mass flow graph, whereas the second part contains useful pressure values to be commented in detail in the parametric study. The level of steadiness of said table has been extracted from Fig. 5.5 in the previous section.

First of all, regarding case 6, from the graph of the mass flow, it is visible that no solution is found. This indeed can be explained by the major unsteadiness of this case, for which the equation  $\dot{m}_T = \dot{m}_{ox} + \dot{m}_f$  is not valid. Hence, this experiment will not be further analyzed. Cases 3 and 4 are also unsteady but at a lower scale than case 6. Thus, one should be skeptical when analyzing these two tests with the 1D theoretical model. Finally, it is expected that the rest of the cases will adjust to the theoretical model given that they reach a reasonable steady regime.

In regard to the values of the total mass flow rate and chamber pressure, they have been obtained from the intersection of the orifice mass flow and the nozzle mass flow at the mean temperature of the range (1900K). The magnitude of these parameters seems to be reasonable, although a further analysis will be performed in the parametric study on the following subsection.

In relation to the mass flow and pressure ranges<sup>2</sup> have been determined from the intersection of the orifice mass flow with the nozzle mass flow at 1400 and 2400K, since the ranges given by the fuel mass flow uncertainty (yellow dashed lines) covered a shorter range of both mass flow and chamber pressure. One interesting aspect of these ranges is that, the higher the values of the pressure range, the wider the mass flow range is, which is in agreement with the shape of the curve of  $\dot{m}_{ox,N}$ . A deeper insight of the mean values and ranges will be provided in the following paragraphs.

Up to now, from table 6.1, the results of the theoretical 1D model have been presented. At this point, their comparison with the empirical data will be performed by means of a second table for the thrust graphs, 6.2. This table is as well subdivided in two parts: in the first one, the coordinates of the intersection point of the  $F$  Vs.  $P_c$  graph are presented; in the second part, the previous  $P_c$  coordinate will be fed back into the table of  $\dot{m}_{ox}$  Vs.  $P_c$  (6.1) to try to obtain an estimation of the chamber temperature, if this value is contained in the specified range.

EXPERIMENT	1	2	3	4	5	6	7	8
$F(T_{mean}) = F_{loadcell}$ (kgf)	0.13	0.33	0.33	0.64	0.70	0.47	0.33	0.38
$P_{c,thrust}$ (bar)	1.04	1.65	No intersection	3.08	3.34	-	1.66	No int.
$\dot{m}_{ox}$ from $P_{c,thrust}$ (g/s)	2.17	2.44	No intersection	2.80	2.62	-	2.48	No int.
$T_c$ from $P_{c,thrust}$ (K)	1900	1800	Not in range	<1400	>2400	-	2250	No int.

Table 6.2: Results obtained from the  $F$  Vs.  $P_c$  graph

On one hand, in cases 1, 2 and 7 the theoretical model is in agreement with the experimental data given

<sup>2</sup>The values of the ranges have been sorted in ascendant order in both cases. Nonetheless, notice that the smallest value of the pressure corresponds to the highest value of the mass flow rate and vice versa.

that  $P_{c,thrust}$  from table 6.2 is contained within the range of  $P_c$  shown in table 6.1. These experiments were expected to agree since they reach a fairly steady regime, and even more, the resulting chamber temperature lies within the specified range.

In relation to case 4, the curves intersect in both graphs although  $P_{c,thrust}$  from table 6.2 is below the range of  $P_c$  shown in table 6.1. This is due to the fact that test 4 was not steady and therefore a higher empirical thrust force would be expected for steady regime. Then the intersection in Fig. 6.6b would have occurred at a higher pressure, being then in agreement with graph 6.6a.

On the other hand, it was expected that cases 5 and 8 would also adjust to the theoretical model, and they do not.

Case 5 was performed with the same configuration as case 4 given the premature failure of the latter, and thus similar results would be expected. As anticipated above, for steady operation the theoretical thrust is higher and therefore, the intersection in Fig. 6.7b occurs at a higher pressure than in case 4. Nevertheless, the results of the theoretical oxygen mass flow in case 5 were surprising: according to experiment 4 the solution would have to occur at a pressure of approximately 3.5 bar, whereas graphic 6.7b shows the intersection at 2.7 bar. Checking the values of the fuel mass flow of these two experiments, it was discovered that  $\dot{m}_f = 7.35g/s$  for case 4, whereas  $\dot{m}_f = 3.04g/s$  for case 5. In comparison with the rest of the cases, the extreme value of case 4 seems to be caused by the combined action of the high level of unsteadiness<sup>3</sup> and the large chamber pressure. Nevertheless, considering the higher chamber pressure in case 5, the corresponding increment in the fuel mass flow seems too low. This led to the conclusion that there was some mistake in the annotation of the fuel mass data in case 5 in the lab, and that the solution of the oxygen flow would have to be close to the results of cases 4, around  $P_c \approx 3.5bar$ .

Given the configuration similarities and the analogous results, experiments 3 and 8, can be analyzed jointly. In none of the two cases, the theoretical and experimental thrust lines intersect. Nonetheless, the difference is very small and may be explained through several sources of error explained below. However, it must be mentioned that case 3 shows a higher degree of unsteadiness, and therefore the intersection of these line would have to occur at an even higher pressure chamber.

The fact that there is no intersection, implies that, for the given  $P_c$ , the measured thrust is higher than the theoretical. This could be caused by several assumptions adopted within the 1D model:

- Fuel mass is steady and independent on the pressure chamber, and its calculation implies a fairly arbitrary selection of the burning time.
- There is no pressure loss across the calibrated hole, nor along the propellant tube: no friction or concentrated losses are taken into account in the whole assembly duct.
- No specific analysis of the internal ballistics is being performed, i.e. internal fluid dynamics or heat transfer in the combustion boundary layer are ignored.
- The combustion reaction is assumed complete and lean, with no production of minor species. This may affect the exhaust gasses properties which are involved in the theoretical thrust calculation.
- Additionally, no time or space dependence is being considered, and the implications of taking an average value of the sensors output when the signal is not completely steady introduces a source of error.

These errors seem to be less significant when the chamber pressure is small, i.e. in cases 1, 2 and 7.

Moreover, we can consider other sources of error which may affect these results, such as the always existing instrument error (affecting the load cell, the pressure transducer and the Analog Discovery 2, mostly), correlation between the transducer reading and the stagnation pressure of the line, possible erosion of the calibrated orifice resulting in a higher throat diameter, calculation error in the zero voltage values, or the difference between the ambient pressure data obtained online and the real value at the lab room.

To sum up, the 1D theoretical model seems to correlate quite well with cases 1, 2 and 7 where the operation reached the steady state and the chamber pressure is relatively low (not choked or barely choked nozzle), whereas for the cases 3 and 8, where a higher chamber pressure is achieved, the theoretical model shows a smaller thrust than the measured value, a disagreement that can be explained by the multiple

---

<sup>3</sup>The inaccuracy of the calculation method of the burning time becomes more relevant for the unsteady cases

assumptions associated to the 1D model. Finally, case 6 was discarded given the multiple failures in the experiment, and in case 5 an incorrect data seems to cause faulty results, so case 4 was taken as a reference although it was not steady. From this reasoning, it can also be concluded that the 1D model provides a conservative analysis of the rocket given that the calculated thrust is smaller than the measured one.

## 6.3 Parametric studies

In this section a mutual comparison between the different experiments will be carried out with the goal of determining the effect of the fuel cartridge length, the nozzle throat diameter and the oxygen tank pressure setting. These comparisons will be based on the data presented in tables 6.1 and 6.2 from the previous subsection.

### 6.3.1 Fuel cartridge length

The data of the fuel mass flow rate and the O/F ratio for each experiment is available in the table 6.3. In said table, it is visible that the O/F ratio in all the cases is rather low, of the order of 1, except for the unsteady cases 3 and 4. This implies that the flow of oxygen through the inner PMMA tube is small and therefore, the combustion will take place mostly in the first section of the tube, remaining the last part unburned.

EXPERIMENT	1	2	3	4	5	6	7	8
$\dot{m}_f$ (g/s)	2.03	1.97	2.40	7.35	3.04	9.25	1.50	1.75
O/F ratio (-)	1.07	1.22	0.62	0.19	1.31	-	1.72	1.40

Table 6.3: Fuel mass flow and O/F ratio.

Indeed, this reasoning is justified by empirical evidence. After performing a firing with one of the long tubes, one could physically examine the fuel sample and notice that the thickness of the tube was significantly reduced near the entry end whereas the thickness at the exit end was mostly the same as in the new tube. Then, given that three firings were performed for each propellant tube, in the latest the tube would start to deform and melt around the low thickness section, as it can be seen in Fig. 6.11.

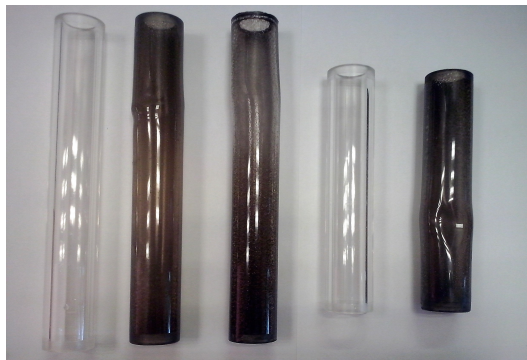


Figure 6.11: New and used propellant tubes. From left to right: new tube (210mm); used tube for experiments 1,2 and 3; used tube for experiments 4,5 and 6; new tube (150mm) and 7 and 8

According to this, it was expected that by reducing the fuel tube length from 210 to 150mm the performance of the rocket would not be almost affected. This, indeed can be corroborated by the comparison of experiments 2 and 7 in table 6.2. Between cases 3 and 8 though, there is a small difference, but it is due to the fact that case 3 is not steady, and therefore the thrust value for a steady operation would have been slightly higher, like in case 8.

From this results, one can conclude that the effect of the fuel length reduction is null in the thrust of



the rocket given the low O/F ratio. This is indeed beneficial in terms of material cost since the shorter tube implies a reduction of a 29% of material. Nevertheless, in higher O/F ratios are fulfilled in the future, the shorter fuel tube length could produce some degree of inefficiency, given that in that case the combustion will be more uniform across all the inner surface of the PMMA tube.

### 6.3.2 Nozzle throat diameter

As a first step, the second part of table 6.1 for the study of the sonic conditions at the calibrated orifice and the nozzle throat will be studied given its relevance for the nozzle parametric analysis.

From the comparison of the two critical chamber pressures (as given by the calibrated orifice and the nozzle) with the average  $P_c$  (for 1900K), one is able to state if the corresponding section of the rocket is choked or not. For the case of the calibrated orifice, the chamber pressure is the pressure downstream of said section, and therefore the orifice will be choked for  $P_c(T_{mean}) < P_{c,crit-h}$ . On the other hand, from the analysis at the nozzle, the chamber pressure is the value upstream the throat, hence, this section will be choked for  $P_c(T_{mean}) > P_{c,crit-n}$ .

As it can be seen from the table, in none of the cases the calibrated orifice is choked since the pressure ratio between the oxygen stagnation pressure upstream and the chamber pressure downstream is too small. This means that the oxygen flow will be dependent on the chamber pressure.

This is a unforeseen effect, since one should have expected that the oxygen stagnation pressure would be high enough for the orifice to be choked. Nevertheless, looking at the values of  $P_0$  included in table 6.1, it is concluded that the pressure drop along the gas line is surprising high (between a 50 and 75% of the tank pressure).

With respect to the sonic conditions at the nozzle, it is clearly visible that all the values of  $P_{c,crit-n}$  are very similar since the ambient pressure is so. Then, depending on the value of the chamber pressure, the nozzle throat will be choked or not.

In regard to the nozzle study, as aforementioned, it was decided to perform a first experiment with the previous graphite nozzle so as to have a reference point for the analysis, although it was clear that the throat was too large to reach sonic conditions. Then, for the rest of the experiment the stainless steel nozzles of 4 and 6 mm throat were used.

In the design process, the selection of the 6mm throat nozzle was believed to be very conservative, since the maximum nozzle diameter to reach sonic conditions given by the study was 7.5mm (for  $P_{amb}$ ). Nevertheless, when the pressure transducer was introduced, the assumption of a 17% pressure loss in the oxygen line was found to be completely inaccurate since the sensor readings revealed a loss between a 50 and a 75%. This implies a much lower chamber pressure, and consequently, a smaller nozzle throat would be needed to reach sonic conditions.

Again the results in this section will be based on the theoretical and empirical analysis in tables 6.1 and 6.2, even for the cases in which the 1D model do not totally agree with the experimental data since there is no available empirical information regarding the chamber pressure.

The parametric study of the nozzle could be performed from the comparison of cases 1, 2 and 3, nonetheless, given that cases 7 and 8 show a greater degree of steadiness and that it has been proven that the effect of the fuel cartridge is minimal, the comparison will be performed between the experiments 1, 7 and 8.<sup>4</sup>

From the comparison of cases 1 and 7 in table 6.2, it is easily visible that the 6mm nozzle produces an increase in the chamber pressure from 1.04 to 1.66bar with respect to the 9.5mm, given that a smaller throat section restricts the flow, and a larger pressure is reached upstream. In case 1, the nozzle is clearly not choked, nonetheless, in case 7, the nozzle is just in sonic conditions. Additionally, the oxygen mass flow increases from 2.17 to 2.48g/s. Then, as a consequence of the pressure and mass increase, the thrust force raises from 0.13 to 0.33kgf.

With respect to the comparison between cases 7 and 8, it leads to interesting results: on one hand, the chamber pressure raises from 1.66 to almost 4 bar, concluding that for the 4mm nozzle the throat is clearly choked. Nonetheless, the thrust force only increases from 0.33 to 0.38 kgf. This is in fact easily explained from the thrust equation (3.24) and from the definition of sonic conditions. On one hand, the value of the oxygen mass flow (2.48g/s) in case 7 is the maximum flow given at sonic conditions. For the

---

<sup>4</sup>Cases 4, 5 and 6 cannot be compared given the component failure in cases 4 and 6.

case 8, in which choking conditions are assumed to be held, the maximum mass flow in the hypothetical case of an intersection of the thrust curves would be fairly lower than 2.44g/s as given by table 6.1. Therefore, considering just the first term in eq. 3.24, case 7 would result in a higher thrust than case 8. Nonetheless, in case 8, there is a second contribution to the thrust force given by:  $(P_c - P_{amb}) \cdot A_t$ , where the component  $(P_c - P_{amb})$  is rather large, but  $A_t$  is very small. Finally, from a lower first contribution of the thrust and a unique positive contribution of the choked section, case 8 results in a slightly higher thrust value than case 7.

Therefore, the conclusions from this parametric study are significant since it has been determined that for a nominal relative tank pressure of 6 bar, the nozzle of 6mm turns out to be the upper limit of the throat diameter that results in choking conditions ( $P_c = P_{c,crit-n}$ ), and consequently any smaller throat section, i.e. the 4mm nozzle, is clearly choked. Nonetheless, the high reduction of the area leads to a smaller total mass flow that results in a low increase of the thrust.

### 6.3.3 Oxygen tank pressure setting

In the concerning parametric study, the availability of valid empirical results is significantly smaller given that two of the three firings performed at 9bar were frustrated due to the melting of the feeding gas tubes. Therefore, the discussion should be focused on the comparison between case 5, the only successful experiment at high pressure setting, and case 2, the corresponding case in terms of fuel tube length (210mm) and nozzle diameter throat (6mm) for a relative tank pressure of 6bar. However, as concluded in the previous section, it is believed that there is an incorrect measurement in case 5, and thus, case 4 (with the same configuration of fuel length, nozzle throat and tank pressure as case 5) will be chosen instead despite its unsteadiness.

From the mutual comparison of both experiments (2 and 4) in table 6.1, the stagnation chamber pressure rises from 1.65 to 3.08bar, as it can be expected. From graph 6.4b (case 2), as mentioned before, the chamber pressure is exactly in the limiting value of the nozzle critical pressure, whereas in case 4 (graph 6.6b), the nozzle is clearly choked and the chamber pressure is much larger than the critical. Consequently, no difference would be appreciated with respect to the first contribution of the theoretical thrust in eq. 3.24 given that both experiments were performed with the same nozzle, although the second contribution of said thrust ( $(P_c - P_{amb}) \cdot A_t$ ) is almost double in case 4, as it can be corroborated by the empirical thrust results presented in table 6.2.

In this case, the comparison has been made for the nozzle of 6mm given that no meaningful empirical data could be obtained from the configuration of 9bar tank setting and 4mm nozzle (experiment 6). From this discussion, it can be observed that the chamber pressure for the 9bar tank setting is considerably higher than for the 6bar tank setting. Consequently, one can argue that the failure of the gas tubes in experiment 6 that caused the spurious data can be explained by the combined action of the small throat section and the high tank setting that raised the chamber pressure high above choking conditions. Indeed, this can be corroborated from the empirical thrust reading, which relatively high (0.47kgf) even though the operation at that point was highly unsteady (i.e. the steady measure of the thrust would be significantly higher).

To sum up, by increasing the oxygen tank pressure setting, the oxygen mass flow will increase up to the maximum allowed at sonic conditions, and therefore this is the most effective manner of optimizing the thrust given that no secondary effects are present, unlike the case of the throat reduction.

From the three previous parametric studies, it is possible to confirm that the rocket would be able to withstand much larger chamber pressures and therefore produce a higher thrust provided that the pressure loss in the oxygen line is reduced and that the gas feeding tubes are reinforced to avoid failure.

## 6.4 Analysis of the regression rate

From Section 3, it was stated that for hybrid rockets the fuel regression rate was proportional to the oxidizer mass flow in a simplified model, according to equations 3.1 and 3.2. The corresponding data for each experiment is summarized in table 6.4.

EXPERIMENT	1	2	3	4	5	6	7	8
$r$ (mm/s)	0.14	0.13	0.16	0.49	0.20	0.62	0.13	0.16
$G_{ox}$ (g/(m <sup>2</sup> - s))	6.90	7.45	4.74	4.54	12.66	-	8.20	7.77

Table 6.4: Regression rate and oxygen flux.

Usually, the regression rate in hybrid rockets is of the order of a few mm/s. Given that the values of this prototype are one order of magnitude smaller, the performance is expected to be low, as it has been previously concluded from the low oxygen mass flow.

Additionally, the fact that the O/F ratio in mass terms is smaller than 5, implies that the prototype is not operating in the range of O/F values for which the approximation in the mentioned equations is valid. To obtain more meaningful results the experiment 4 will be ignored due to the nitrogen tube failure and case 5 will also be omitted due to the possible incorrect datum. Then, representation of experiments 1, 2, 3, 7 and 8, in the regression model is represented in Fig. 6.12.

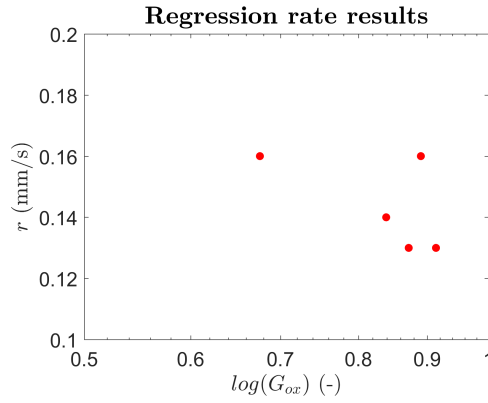


Figure 6.12: Results of the regression model

From said graph it is clearly visible that the data points do not follow a linear ascending behavior given that the O/F ratio is not high enough. Therefore, no feasible characterization of the rocket can be obtained from this simplified analysis.

# 7 Conclusions and future work

## 7.1 Conclusions

The results obtained in this research have been very conclusive thanks to the physical improvements performed to the prototype that have allowed a successful gathering of data.

The juxtaposition of the theoretical and empirical results permitted to obtain an estimation of the chamber pressure, a crucial parameter to achieve a basic rocket characterization.

First of all, regarding the experimental procedure, the only problem encountered was the recurrent failure of the nitrogen feeding tube near its connexion to the cold block of the rocket.

With respect to the isolated analysis of the experimental data, two major conclusions were obtained: on one hand, the operation of the device was highly unsteady with a few seconds of transient regime after ignition; on the other hand, the calibrated orifice on the cold block did not reach sonic conditions at any instant during the firing since the pressure loss along the oxygen line is extremely high.

Concerning the correlation between the theoretical and empirical results, it was concluded that, in general the one-dimensional model agreed quite acceptably with the experimental data, although the fitting was more precise for lower values of the chamber pressure. Indeed, the major uncertainty in the process was caused by the lack of empirical data that allowed an estimation of the chamber temperature. This forced to extend the analysis to a wide range of temperature values that increased significantly the uncertainty of the oxygen mass flow theoretical solution. Nonetheless, given that the dependence of the theoretical thrust on this value was minimal, for the cases in which the theoretical correlation for the thrust was acceptable, it was possible to obtain an estimation of the chamber temperature which lied within the previously specified range. As a final remark on the theoretical model, it is worth mentioning that the 1D model constitutes a conservative approach for the prototype modeling and design process given that the provided theoretical pressure is usually lower than the load cell reading.

Regarding the simple regression rate model, it was concluded that the simplifications of the complete model were not applicable given the low value of the O/F ratio.

The final conclusions are related to the three parametric studies performed on the basis of the experimental and theoretical results from the previous data juxtaposition.

- On one hand, given the low oxygen pressure to chamber pressure ratio, the oxygen mass flow was small. This resulted in fairly low values of O/F of around 1 (in mass base). As a consequence the combustion did not occur uniformly along the fuel tube length, but it was prominent in the entry extreme, leaving the exit end almost unburned. This ultimately led to conclude that a reduction of the fuel tube length would not affect the rocket performance and in turn would involve important material savings.
- On the other hand, regarding the nozzle throat, it was discovered that 6mm is the exact minimum throat diameter for the nozzle to reach sonic conditions. Lower values of the throat area would result in higher chamber pressures, although the increase in the thrust force would not be significant.
- Finally, a higher oxygen tank pressure setting is the most efficient way to increase the performance of the rocket: the increase in both the oxygen flow and chamber pressure results in choking conditions at the nozzle throat, which in turn would produce an important increase of the thrust (higher for larger throat sections).

From these individual parametric analysis, one is able to conclude that the rocket would be capable of achieving very good performances provided that the oxygen pressure at calibrated orifice is increased.

## 7.2 Future work

Based on the previous conclusions, several improvements are discussed here as suggestions for their future implementation.

In relation to the physical improvements of the prototype, in order to avoid the melting of the gas lines, a small run of the polyurethane tubes near the connexion to the cold block need to be replaced by stainless steel tubes so that heat is better dissipated. Another important issue is the extremely low oxygen pressure that reaches the rocket. This implies high efficiency losses and reducing the thrust capacity of the device, so it would be extremely advisable to modify the gas installation so as to reduce the pressure loss. If these two measures are fulfilled it is expected that the chamber pressure and consequently the thrust show a very significant increase.

Apart from this, given the corroded state of the post-combustion chamber (Piece 4), it would be convenient to replace it by a new piece.

In relation to the lack of experimental temperature data, it would be necessary to include a device or system to provide a measurement. A thermocouple would imply a difficult and delicate implementation, therefore a feasible solution could be the estimation of the temperature by spectrometry: the spectrometry would analyze the atomic spectral lines provided by the rocket exit flame in order to determine the composition of the exhaust gases that would allow to obtain a truthful measure of the combustion temperature. This process offers the advantage of avoiding any perforation of the rocket components, nevertheless, the installation of the required cameras may be problematic as the supporting structure could interfere.

In principle, this temperature data would allow a more precise calculation of the chamber pressure. Nonetheless, it could also be beneficial to introduce a pressure sensor inside the gas duct, most likely in the post-combustion chamber, whose reading could be compared with the results obtained in this project.

Regarding additional theoretical models, it would be convenient to perform a detail 2D analysis of the combustion process taking into account the heat transfer and addition of mass considering the time and space dependence, as well as to attempt to reach a more accurate estimation of the fuel flow rate.

Finally, at this point it would be interesting to develop a simple feasibility plan to modify the prototype so as to fulfill flight conditions. This can basically consist on a small study regarding the thrust that would be needed for lift-off with the current prototype, compare it with the empirical thrust, and study different materials to achieve a sufficient reduction of weight in the device, provided that the performance and integrity of the thruster are not affected.

# 8 Project budget and socioeconomic model

## 8.1 Project budget

The budget of the project is disaggregated in table 8.1.

ITEM	QUANTITY	UNITARY PRICE	SUBTOTAL (€)
<b>Pneumatic components</b>			
Pneumatic connectors	4 u	4.583 €/u	18.33
Pressure transducer	1 u	121.70€/u	121.70
<b>Structural material</b>			
Steel cable	10 m	1.418 €/m	14.18
Slings (steel cable)	10 u	0.573 €/u	5.73
Aluminum profiles	4 x 30 cm	8.50 €/m	10.27
<b>Material costs</b>			
Inox steel for nozzle parts	12 cm	160€/m	19.20
PMMA tubes	6 x 21 cm	8.80 €/m	11.09
	3 x 15 cm		3.96
	1 x 14 cm		1.23
<b>Workforce costs</b>			
Workshop technician	12 h	50.00 €/h	600
Technical engineer <sup>1</sup>	40 h	80.00 €/h	3200
<b>Facilities renting</b>			
Lab room renting <sup>2</sup>	7days x 5 h/day	200 €/5h	1400

Table 8.1: Project budget

The actual total budget of the project (without taking into account the hypothetical lab room renting and technical engineer costs) would be: **805.69€**.

A more realistic budget for the case in which it would have been necessary to rent the UC3M facilities and to remunerate a technical engineer to perform the experiments, the total project budget would have been: **5405.69€**.

It is also worth mentioning that the tooling, electric and gases costs (oxygen, nitrogen and propane) have been neglected.

Finally, it must be noticed that from the 6 PMMA long inner tubes fabricated, only 3 were consumed, whereas from the 3 short inner tubes only one was consumed.

## 8.2 Socioeconomic model

The hybrid rocket prototype presented in this project is a very useful tool to obtain a basic insight on hybrid rockets. The physical improvements of the device have allowed a more reliable operation and a fairly good characterization of the rocket.

In regard to a possible socioeconomic model, this improved rocket will have a direct positive impact on the UC3M community and in particular on the students of the Bachelor in Aerospace Engineering. The fact that there is a lab session addressing this prototype facilitates and improves the education of the future engineers which may become experts in this field.

In the longer-term, the results obtained in this and more complex tests could be gathered in a database, leading to a more deep and detailed analysis of the rocket performance. Ultimately, this good understanding of hybrid rockets could serve as a guide and be used for public or private entities with the objective of

performing large scale projects that otherwise would not be affordable.

Ultimately, as it is currently being investigated, hybrid rockets could have a bright future in the field of space transport which would allow to perform intra- or inter-planetary travels not only to the astronauts but also to civil clients.





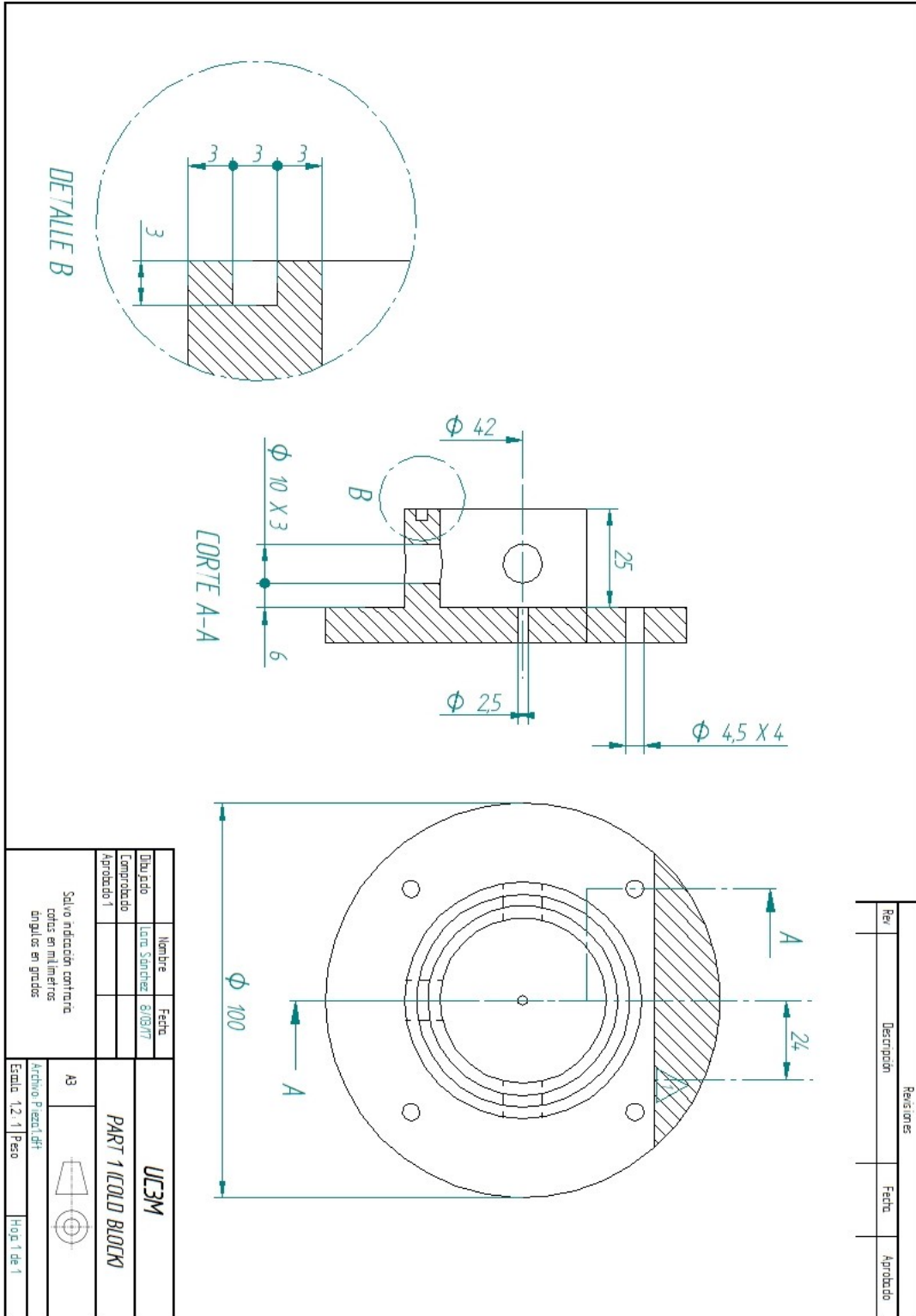
# Bibliography

- [1] G. P. Sutton & O. Biblarz, "Hybrid propellant rocket", in *Rocket propulsion elements*, 8<sup>th</sup> edition. Hoboken, N.J.:Wiley, 2010, pp. 594-621.
- [2] B. J. Cantwell, "Hybrid rockets", *Aircraft and rocket propulsion*, 13/05/2016. [Online] Retrieved from: [https://web.stanford.edu/~cantwell/AA283\\_Course\\_Material/AA283\\_Course\\_Notes/AA283\\_Aircraft\\_and\\_Rocket\\_Propulsion\\_Ch.11\\_BJ\\_Cantwell.pdf](https://web.stanford.edu/~cantwell/AA283_Course_Material/AA283_Course_Notes/AA283_Aircraft_and_Rocket_Propulsion_Ch.11_BJ_Cantwell.pdf)
- [3] C. Seisdedos, "Diseño y construcción de un motor cohete híbrido", Bachelor thesis, Aerospace Engineering Department, Leganés, Spain, 2013. [Online] Retrieved from: <https://e-archivo.uc3m.es/handle/10016/17879>
- [4] S. Esteban, "Design and construction of an upgraded hybrid rocket", Bachelor thesis, Aerospace Engineering Department, Leganés, Spain, 2016. [Online] Retrieved from: <https://e-archivo.uc3m.es/handle/10016/24213>
- [5] M. V. Fernandes & P. C. Greco, "Hybrid rocket motors propellants: a historical approach", presented in the 21<sup>th</sup> International Congress of Mechanical Engineering, Natal (Brazil), 24-28 October. [Online] Retrieved from: <http://www.abcm.org.br/anais/cobem/2011/PDF/046902.pdf>
- [6] T. Benson, "Brief history of rockets", *National Aeronautics and Space Administration*, 12/06/2014. [Online] Retrieved from: [https://www.grc.nasa.gov/www/k-12/TRC/Rockets/history\\_of\\_rockets.html](https://www.grc.nasa.gov/www/k-12/TRC/Rockets/history_of_rockets.html)
- [7] B. Dunbar, "A pictorial history of rockets", *National Aeronautics and Space Administration*, 16/06/2017. [Online] Retrieved from: [https://www.nasa.gov/pdf/153410main\\_Rockets\\_History.pdf](https://www.nasa.gov/pdf/153410main_Rockets_History.pdf)
- [8] M. La Vone, "Virgin Galactic, a brief history", *Space Safety Magazine*, 31/10/2014. [Online] Retrieved from: <http://www.spacesafetymagazine.com/space-disasters/virgin-galactic/virgin-galactic-brief-history/>
- [9] Virgin Galactic, "Update from Mojave: VSS Unity Loads Up for Latest Flight", *Unity test flight program updates*, 01/06/2017. [Online] Retrieved from: <http://www.virgingalactic.com/update-from-mojave-vss-unity-loads-up-for-latest-flight/>
- [10] S. R. Turns, "Appendix A: Selected thermodynamics properties of gases comprising the c-H-O-N system", in *An introduction to combustion: concepts and applications*, 2<sup>nd</sup> edition. New York, N.Y.: McGraw-Hill, 2000, pp. 621-647.
- [11] R. E. Lyon, S. M. Hackett & R. N. Walters, "Heats of Combustion of high-temperature polymers", Federal Aviation Administration, United States of America, Technical note, DOT/FAA/AR-TN97/8, 1998.
- [12] X. Zhang et al., "Effect of particle size distribution on PMMA dust flame propagation behaviors", *Powder technology*, Vol. 317, pp. 197-208, 2017.
- [13] D. Alibert, M. Coutin & B. Porterie, "Effect of oxygen concentration on the combustion of horizontally-oriented slabs of PMMA", *Fire Safety Journal*, (2017), DOI: 10.1016/j.firesaf.2017.03.051
- [14] A. Kacem et al., "A fully coupled fluid/solid model for open air combustion of horizontally-oriented PMMA samples", *Combustion and Flame*, Vol. 170, pp. 135-147, 2016.
- [15] T. Benson, "Titan Rocket Gallery", *National Aeronautics and Space Administration*, 12/06/2014. [Online] Retrieved from: <https://spaceflightssystemsgrc.nasa.gov/education/rocket/gallery/titan/titan1.html>

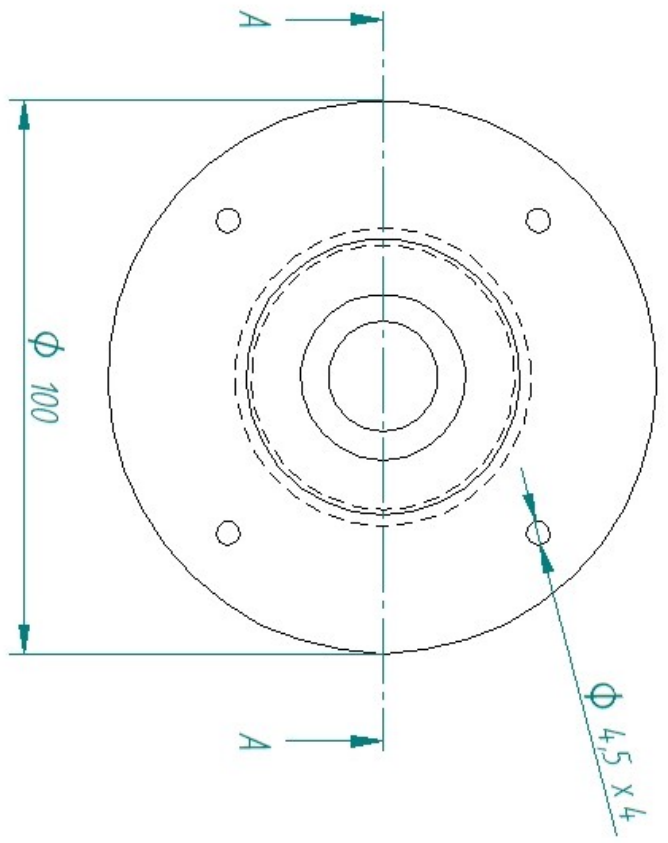
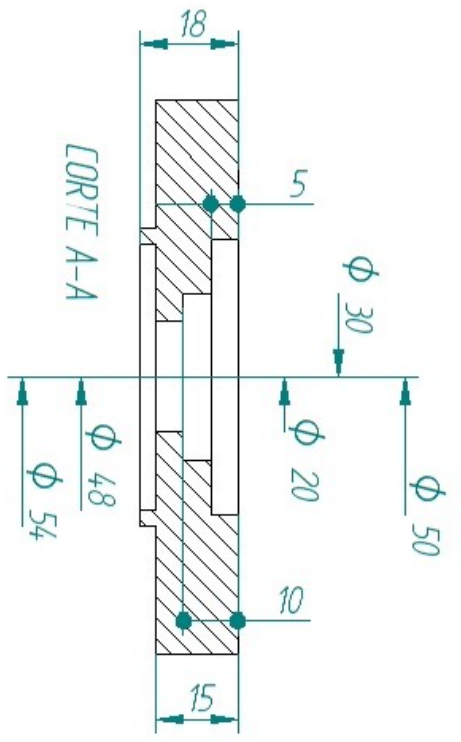
- [16] W. Langewiesche, "Everything You Need to Know About Flying Virgin Galactic", *Vanity Fair*, 01/04/2015. [Online] Retrieved from:  
<http://www.vanityfair.com/news/2015/03/what-is-it-like-to-fly-virgin-galactic>
- [17] N. Hall, "Solid Rocket Engine", *National Aeronautics and Space Administration*, 05/05/2015. [Online] Retrieved from:  
<https://www.grc.nasa.gov/www/k-12/airplane/srockth.html>
- [18] N. Hall, "Liquid Rocket Engine", *National Aeronautics and Space Administration*, 05/05/2015. [Online] Retrieved from:  
<https://www.grc.nasa.gov/www/k-12/airplane/lrockth.html>
- [19] C. Campbell-Knight, "Hybrid Rocket Motor Overview", *Space Safety Magazine*, 01/11/2014. [Online] Retrieved from:  
<http://www.spacesafetymagazine.com/aerospace-engineering/rocketry/hybrid-rockets-overview/>

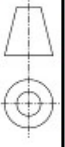
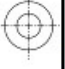
# Appendices

## Part plans

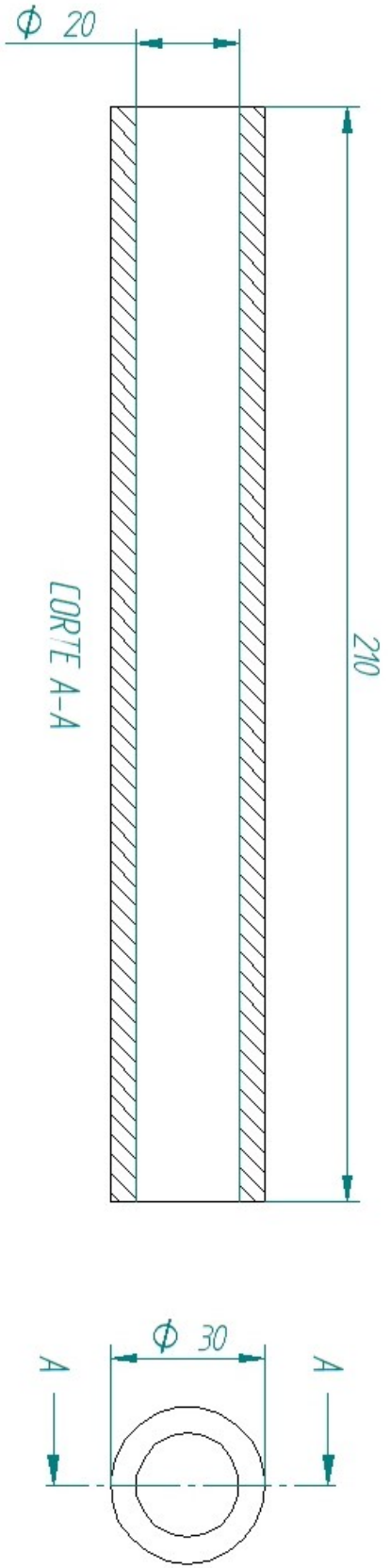


Revisiones			
Rev	Descripción	Fecha	Aprobado



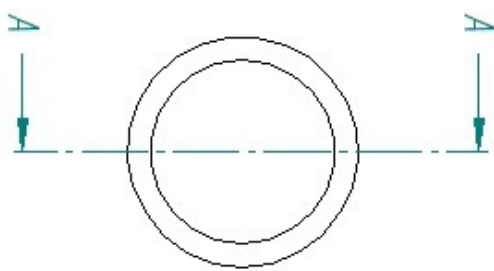
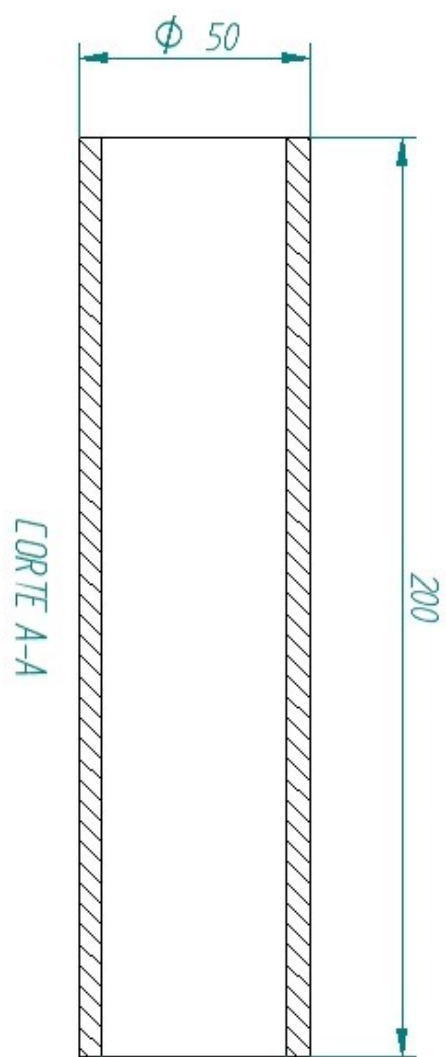
Nombre		Fecha		<b>ULCM</b> <b>PART 2 (COLD BLOCK)</b>	
Dibujado		8/08/17			
Comprobado					
Aprobado 1				A3 	
Salvo indicación contraria cotas en milímetros ángulos en grados				Archivo Piezo 2.dft Escala 1:2:1 Peso 	
				Hoj. 1 de 1	

Revisiones			
Rev	Descripción	Fecha	Aprobado



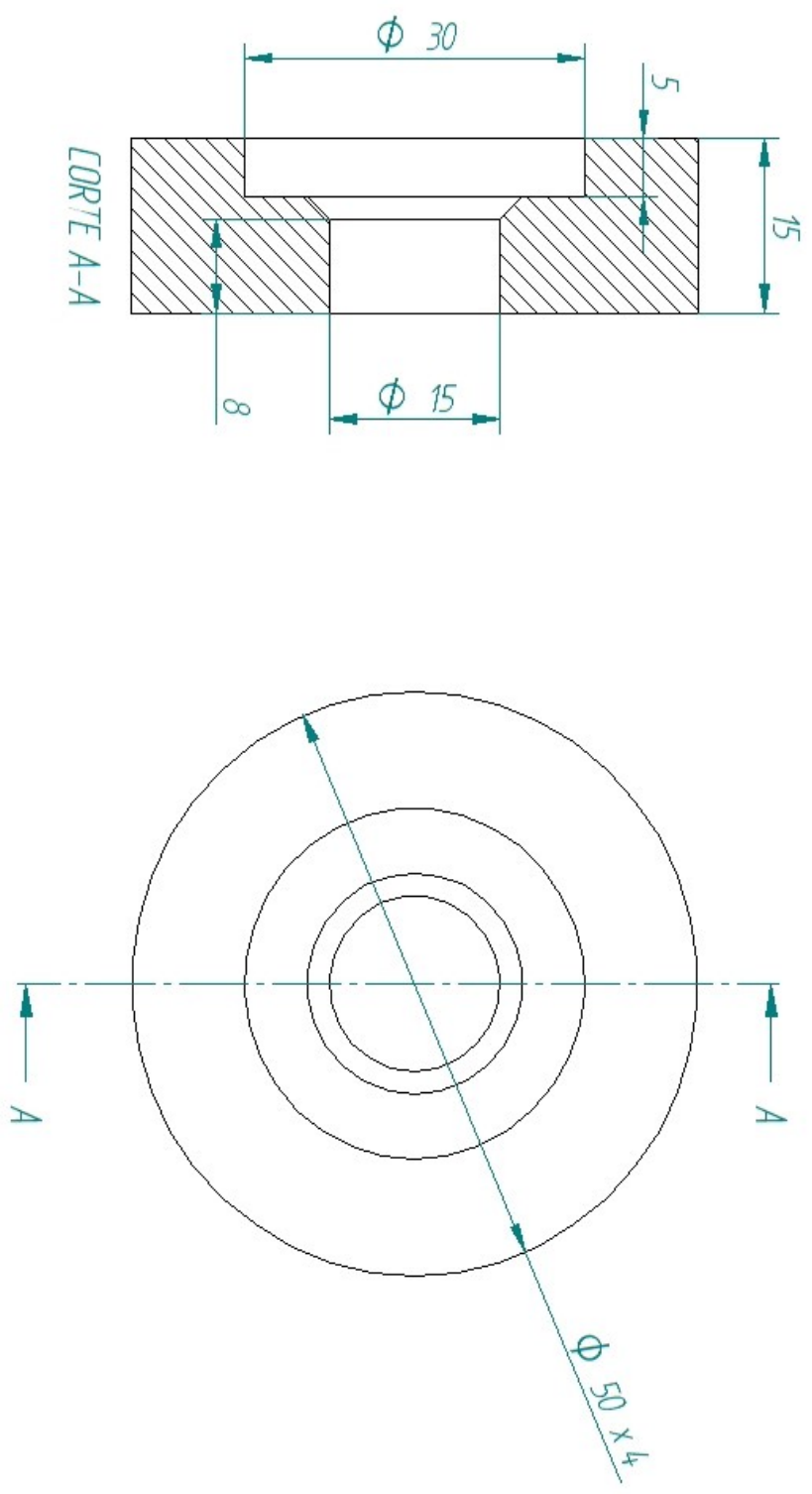
Nombre		Fecha		<b>UC3M</b>
Dibujado		7/09/17		
Comprobado				
Aprobado 1				<b>INNER TUBE</b>
Salvo indicación contraria cotas en milímetros ángulos en grados				A3
Archivo Inner_Tube.dft				
Escala 1:2				Peso
				Hoja 1 de 1

Revisions			
Rev	Description	Fecha	Aprobado



Nombre	Fecha	<b>UEM</b> <b>OUTER TUBE</b>
Dibujado Lara Sanchez 7/08/17		
Comprobado		
Aprobado 1		
Salvo indicación contraria todos en milímetros ángulos en grados		
A3		
Archivo: Outer_Tube.dwg	Escala 1:1	Peso
		Hoja 1 de 1

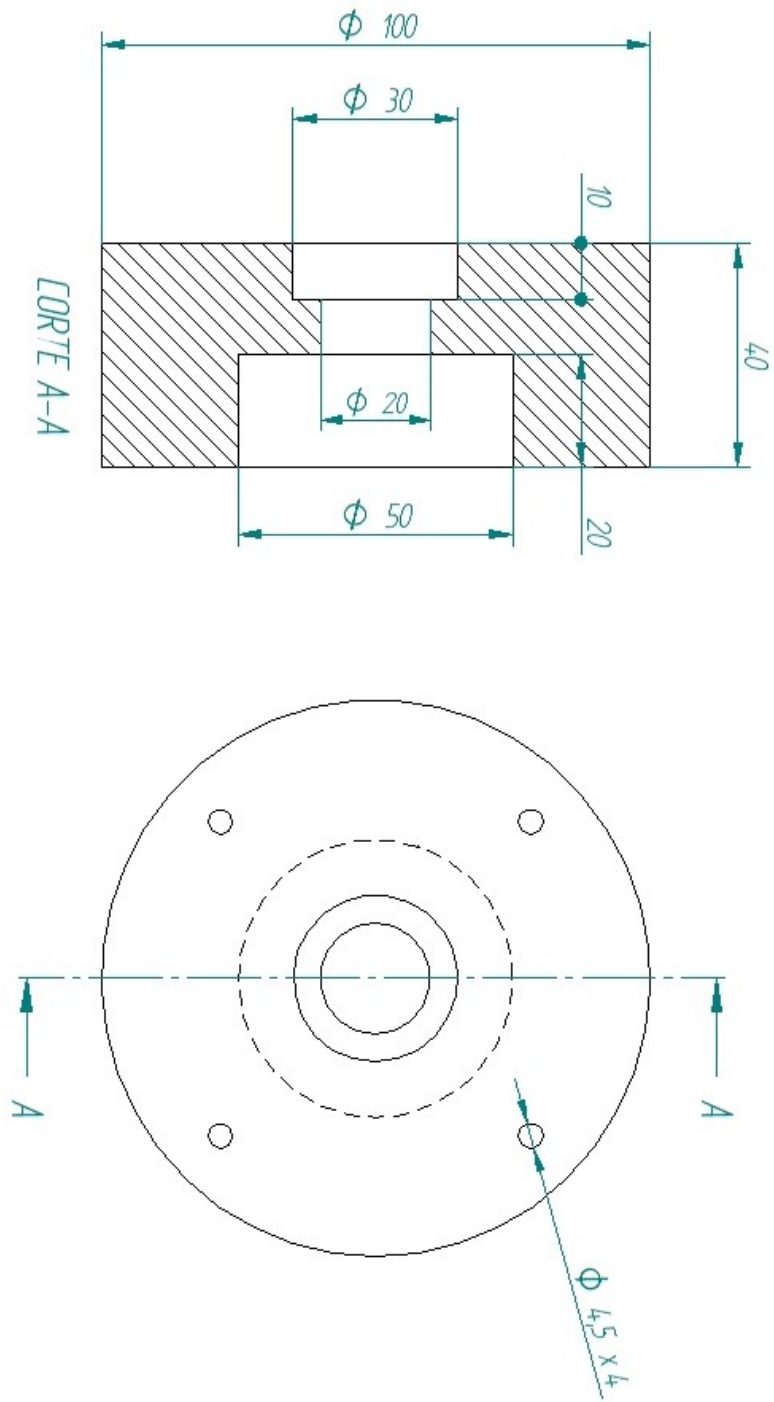
Revisiones			
Rev	Descripcion	Fecha	Aprobado



Nombre	Fecha	<b>UC3M</b>
Dibujado Lara Sanchez	9/09/17	
Comprobado		
Aprobado 1		
<b>GRAPHITE PART (HOT BLOCK)</b>		
A3	Archivo: Piezo_grafito.dft	
Escala 25:1	Peso	Hoja 1 de 1

Salvo indicación contraria  
cotas en milímetros  
ángulos en grados

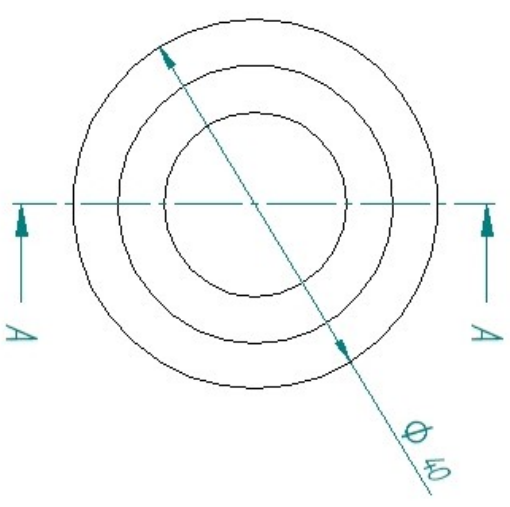
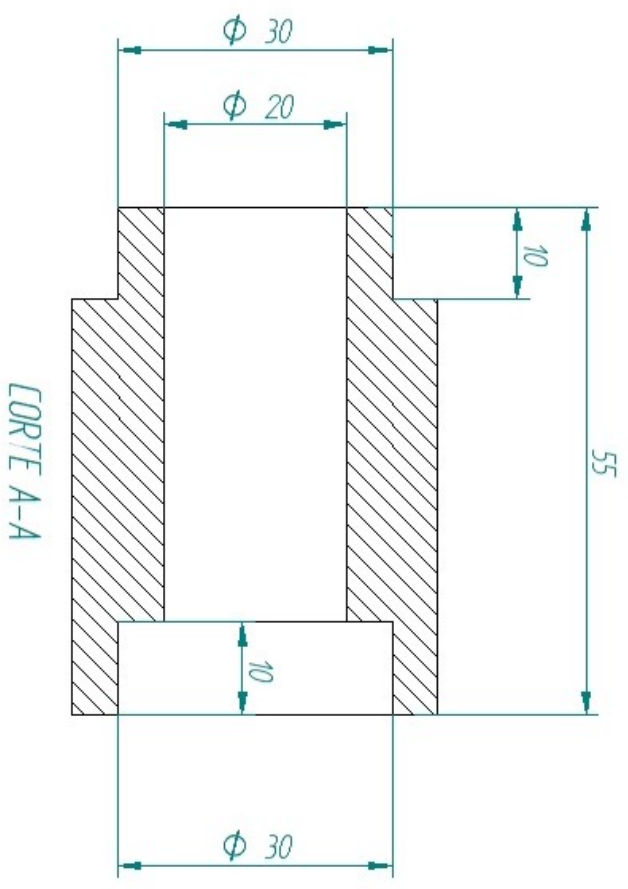
Revisiones			
Rev	Descripción	Fecha	Aprobado



Nombre	Fecha	<b>UC3M</b> <b>PART 3 (HOT BLOCK)</b>
Dibujado Lara Sanchez	8/09/17	
Comprobado		
Aprobado 1		
Salvo indicación contraria cotos en milímetros ángulos en grados		Archivo: Pienzo3.dft Escala: 1:2:1   Peco   Hoja 1 de 1

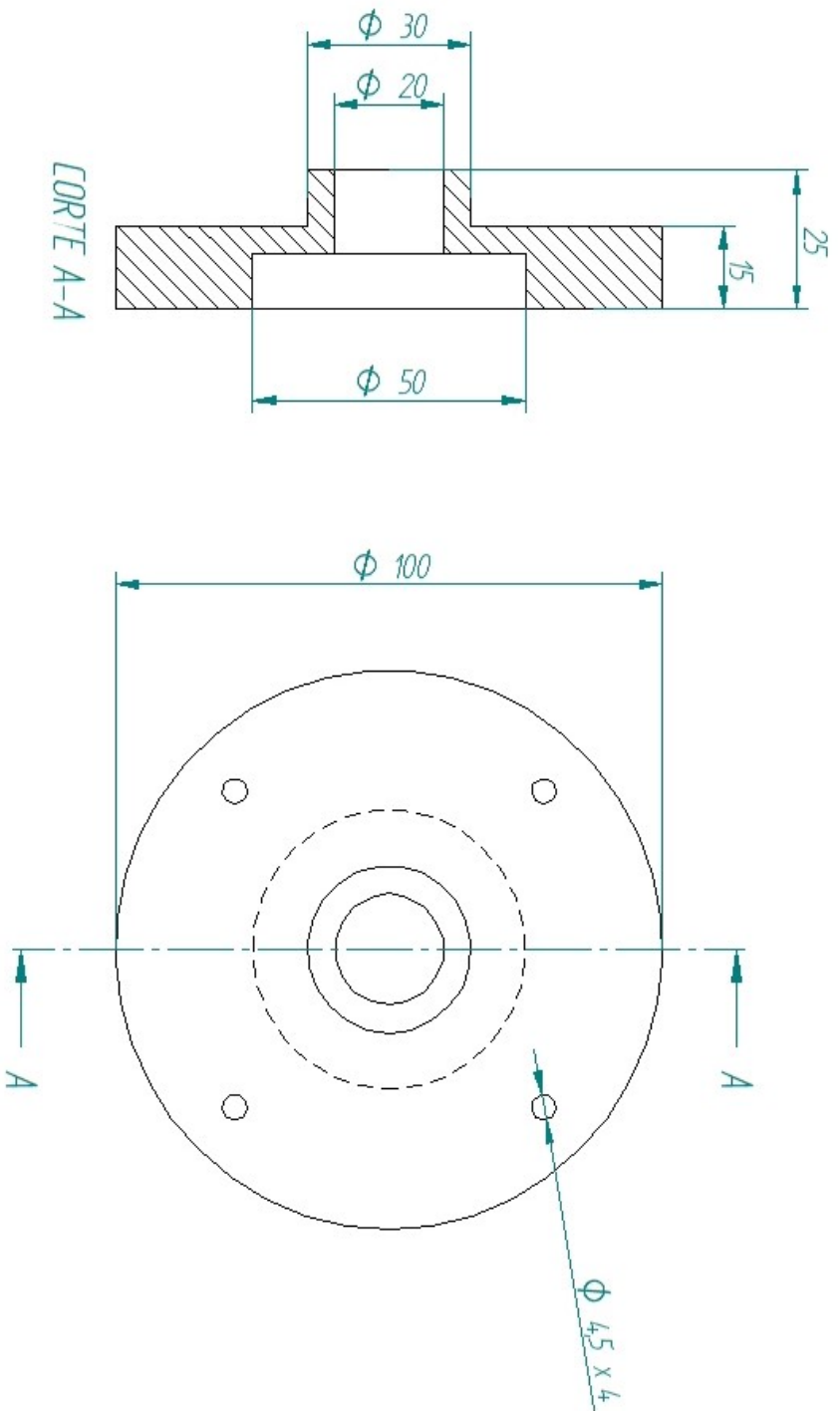


Revisiones			
Rev	Descripción	Fecha	Aprobado



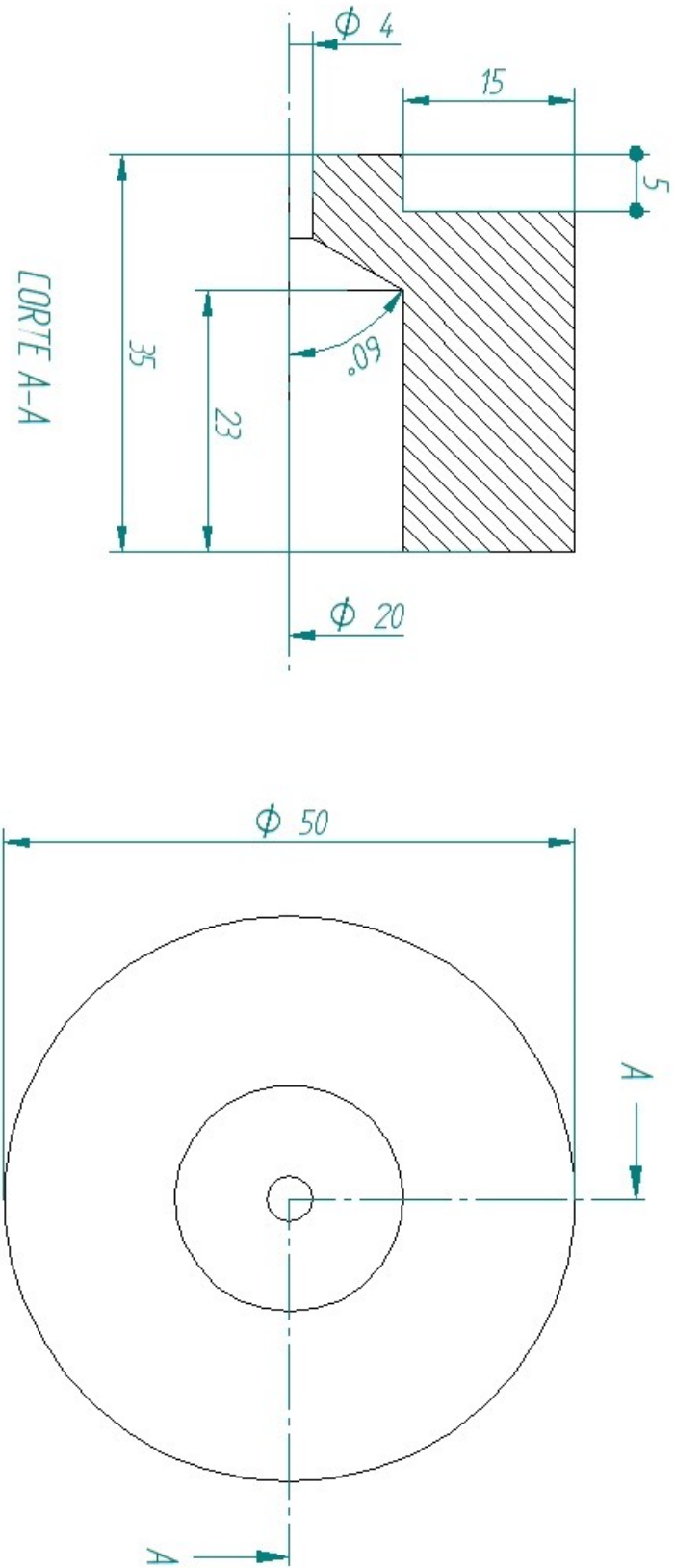
Nombre		Fecha		<b>ULCM</b>
Dibujado		9/08/17		
Comprobado				
Aprobado 1				POST-COMBUSTION CHAMBER
Salvo indicación contraria cotas en milímetros ángulos en grados				Archivo: Pieza.dft
A3		Escala 2:1		Peso
		Hojas 1 de 1		

Revisiones			
Rev	Descripción	Fecha	Aprobado



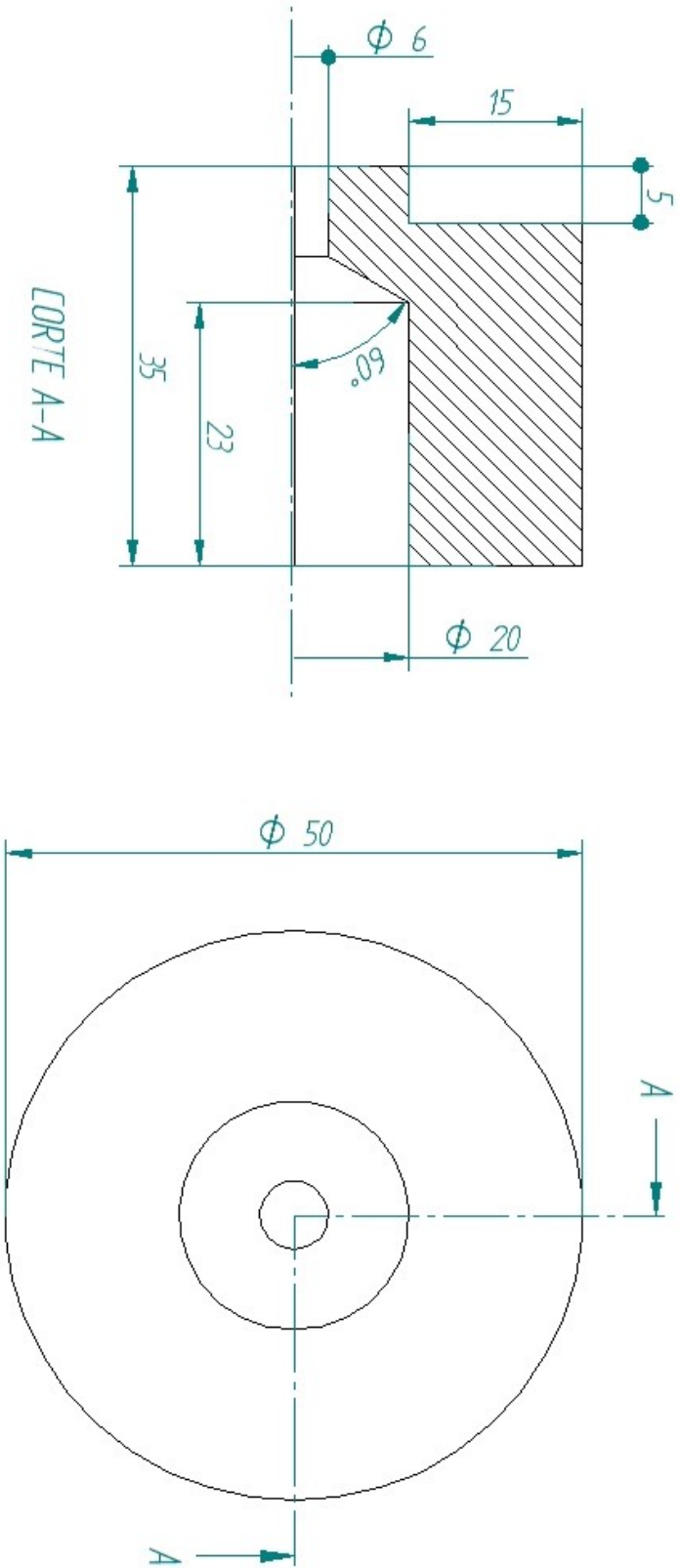
Nombre		Fecha	
Lara Sánchez		9/09/17	
Dibujado		Comprobado	
Aprobado 1			
<b>UC3M</b> <b>PART 5 (HOT BLOCN)</b>			
Salvo indicación contraria todas en milímetros ángulos en grados		A3	
Archivo: Piezas5.dft		Escala: 1:2:1	
Peso		Hoja: 1 de 1	

Revisiones			
Rev	Descripcion	Fecha	Aprobado



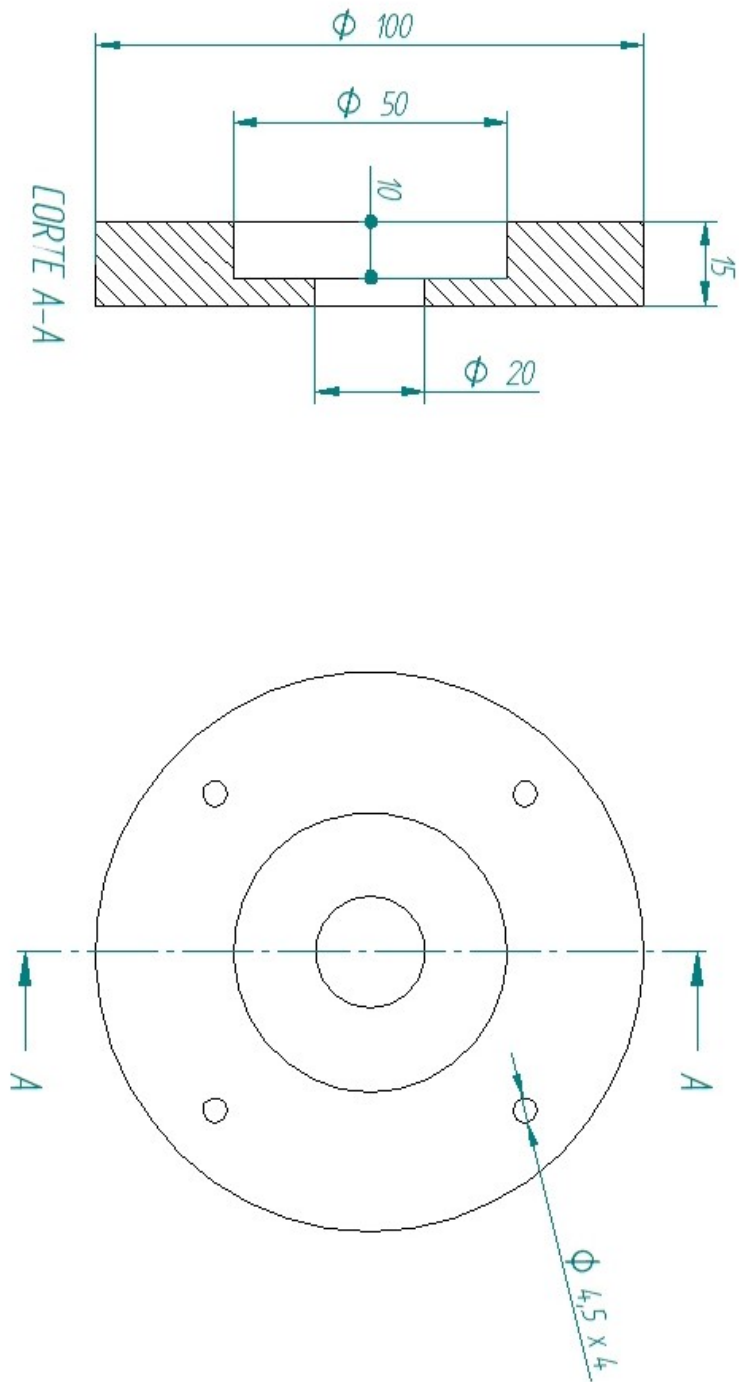
Nombre	Fecha	<b>UC3M</b>
Dibujado Lara Sanchez	18/03/17	
Comprobado		
Aprobado 1		<b>NOZZLE 4mm</b>
Salvo indicación contraria cotas en milímetros ángulos en grados		A3
Archivo: Nozzle_4mm.dft		
Escala 25:1	Peso	Hoja 1 de 1

Revisiones			
Rev	Descripción	Fecha	Aprobado



Nombre		Fecha		<b>UC3M</b> <b>Nozzle 6mm</b>	
Dibujado		16/03/17			
Comprobado					
Aprobado 1					
Salvo indicación contraria cotas en milímetros ángulos en grados					
A3		Archivo: Nozzle_6mm.dft Escala: 25 1   Peso		Hoja 1 de 1	

Revisiones			
Rev	Descripción	Fecha	Aprobado



Nombre		Fecha		<b>UC3M</b> <b>PART 6 (HOTBLOCO)</b>	
Dibujado		9/08/17			
Comprobado					
Aprobado 1				A3 	
Salvo indicación contraria cotas en milímetros ángulos en grados				Archivo: Pizarra 6.dft Escala: 1:2.4 Paso:	Hoja: 1 de 1

# Check list

## CHECK LIST

Nº experiment:

Date:

**NOTE:** If several consecutive firings are to be performed, steps from 10 to 14 (both inclusive) are only necessary for the first firing, and step 28, only for the last one.

Nº Step	Step description	Checked	Comments
1	Before mounting the thruster stack, weight the inner fuel cartridge and take note in the Data .txt file.		
2	Take note of the selected rocket configuration (cartridge length and the nozzle diameter) in the Data .txt file.		
3	Disassemble the previous configuration (if any) of the rocket while hooked (it is easier).		
4	Assemble the new configuration, placing graphite gaskets between every two steel pieces and at both ends of the inner PMMA cylinder.		
5	Tighten firmly the wing nuts using only the fingers, taking care of minimizing the torsion that the mounting rods may present.		
6	Check that the three gas lines quick-connections are correctly matched (N2-to-N2, fuel-to-fuel and O2-to-O2).		
7	Adjust the longitudinal position of the hooks along the aluminium profile: first, adjust the correspondent to the cold block in such a way that the rocket touches the load cell but the mounting rods do not interfere with the aluminium profile of the load cell; then, adjust the hot block hooks to level up the assembly with respect to the horizontal.		
8	Connect the glow plug to the power source: on the rocket end, the red terminal shall be connected to the glow plug and the black one to any of the metallic mounting rods of the rocket; on the opposed end, simply connect the terminals (red-to-red and black-to-black) to the power source.		
9	Check that there is no flammable object placed in the table below the rocket and close the door of the test room after leaving.		
10	Switch on the computer, connect the Analog Discovery 2 to the USB port and open the Waveforms software.		
11	Open the workspace saved as "Rocket_2017": Channel 1 of the oscilloscope corresponds to the pressure transducer voltage reading and Channel 2 to the load cell voltage reading.		
12	Open the gases tanks outside the building and set the pressure. An oxygen pressure of 6 bars is advisable. Take note in the Data .txt file.		
13	Take note of the temperature and atmospheric pressure (checked online) in the Data .txt file.		
14	To achieve a quick opening of the gas valves during operation, first open fully the regulators of the three gas lines while keeping the valves closed. Open the valves momentarily to verify that the three gases flow correctly. End this process by flushing the rocket with nitrogen.		
15	Switch on the power source to provide a 2.8 A current to the glow plug. Start at low voltage and increase it slowly to avoid damaging the glow plug.		

16	Switch on the voltage supply of the Analog Discovery 2 in the Waveforms ("Supplies" window >> ON). Make sure that 5 Volts supply is selected.		
17	Set up a video camera (cell phone camera) to record the firing.		
18	In Waveforms, press the "Record" button on the "Scope" window. This will record voltage samples for both oscilloscope channels during about 1 min.		
19	Open the oxygen valve slowly and fully. Then slowly allow some propane into the rocket until ignition occurs and then, immediately kill the propane flow.		
20	Switch off the glow plug. Keep the rocket running for no more than 10–15 sec.		
21	To stop the combustion, kill the oxygen flow and slowly, open fully the nitrogen valve. Vent for about 20 seconds to purge the burnt gases and speed up the cooling of the thruster.		
22	Switch off the video recording.		
23	By this time the recording process of the Analog Discovery 2 will be almost over. Wait until the recording automatically stops. Then, save the data: File >> Export >> Save. Name the file with the date and experiment number. Write the name of this file in the correspondent check list printed copy. Further export the data in a USB pen drive for its subsequent analysis.		
24	Enter the test room trying to minimize the exposure to the fumes.		
25	Once the metal pieces of the thruster have cooled down, disassemble the thruster while hooked (easier procedure), and take the inner fuel tube.		
26	Weight the fuel tube in the lab balance and take note in the Data .txt file. If in good condition, keep the tube for the next firing; otherwise, replace it with a new one.		
27	Repeat the full process for different combinations of fuel cartridge length, nozzle and oxygen supply pressure.		
28	Clean up and disconnect all the devices: switch off the Analog Discovery 2 voltage source, disconnect the device from the computer and switch off the latter, check that the glow plug power source is off, and close the gas system outside the building.		

**GLOBAL COMMENTS:**

## FC22 Compression Load Cell



- 10 – 100 lbf Ranges
- High Level or mV Outputs
- Interchangeable
- Compact Easy to Fixture Design
- CE Compliance

### DESCRIPTION

The FC22 is a medium compression force sensor that creates new markets previously unrealizable due to cost and performance constraints. The FC22 offers normalized zero and span for interchangeability and is thermally compensated for changes in zero and span with respect to temperature.

The FC22 incorporates MEAS' proprietary Microfused technology which employs micromachined silicon piezoresistive strain gages fused with high temperature glass to a high performance stainless steel substrate. Microfused technology eliminates age-sensitive organic epoxies used in traditional load cell designs providing excellent long term span and zero stability. The FC22 measures direct force and is therefore not subject to lead-die fatigue failure common with competitive designs which use a pressure capsule embedded within a silicone gel-filled cavity. Operating at very low strains, Microfused technology provides an essentially unlimited cycle life expectancy, superior resolution, and high over-range capabilities.

Cost-optimization of the FC22 brings your OEM product to life whether you need thousands or millions of load cells annually. Although the standard model is ideal for a wide range of applications, our dedicated design team at our Load Cell Engineering Center is ready to provide you with custom designs for your OEM applications.

Please refer to the FS20 for lower force applications or the FC23 for higher force applications.

### FEATURES

- Small Size
- Low Noise
- Robust: High Over-Range Capability
- High Reliability
- Low Deflection
- Essentially Unlimited Cycle Life Expectancy
- Low Off Center Errors
- Fast Response Time
- 10 to 100 lbf Ranges
- Reverse Polarity Protected

### APPLICATIONS

- Medical Infusion Pumps
- Robotics End-Effectors
- Variable Force Control
- Load and Compression Sensing
- Exercise Machines
- Pumps
- Contact Sensing
- Weighing
- Household Appliances



## FC22 Compression Load Cell

### STANDARD RANGES

Range	lbf
0 to 10	•
0 to 25	•
0 to 50	•
0 to 100	•

### PERFORMANCE SPECIFICATIONS

Supply Voltage: 5.0V, Ambient Temperature: 25°C (unless otherwise specified)

PARAMETERS	MIN	TYP	MAX	UNITS	NOTES
Span (Unamplified)	19	20	21	mV/V	1
Span (Amplified)	3.88	4.00	4.12	V	1
Zero Force Output (Unamplified)	-1	0	1	mV/V	1
Zero Force Output (Amplified)	0.3	0.5	0.7	V	1
Accuracy (non linearity, hysteresis, and repeatability)		±1		%Span	2
Output Resistance (Unamplified)		2.2		kΩ	
Input Resistance (Unamplified)		3		kΩ	
Temperature Error – Zero	-1.25		1.25	%Span	3
Temperature Error – Span	-1.25		1.25	%Span	3
Long Term Stability (1 year)		±1		%Span	
Maximum Overload			2.5X	Rated	
Compensated Temperature	0		50	°C	
Operating Temperature	-40		+85	°C	
Storage Temperature	-40		+85	°C	
Excitation Voltage (Unamplified)			5	Vdc	
Excitation Voltage (Amplified)	3.3		5	Vdc	
Isolation Resistance (250Vdc)	50			MΩ	
Deflection at Rated Load			0.05	mm	
Humidity	0		90	%RH	
Weight		18.41		grams	

For custom configurations, consult factory.

#### Notes

1. Ratiometric to supply.
2. Best fit straight line.
3. Maximum temperature error over compensated range with respect to 25°C.

### CE Compliance

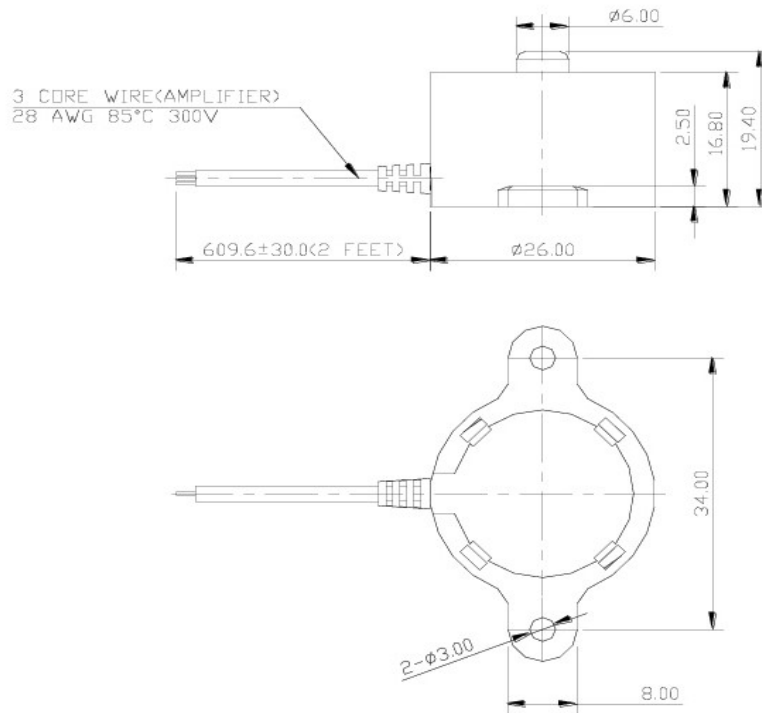
IEC61000-4-2 [4 kV/ 4kV (Air/Contact)]

IEC61000-4-3 (3 V/m)

IEC55022 Class A

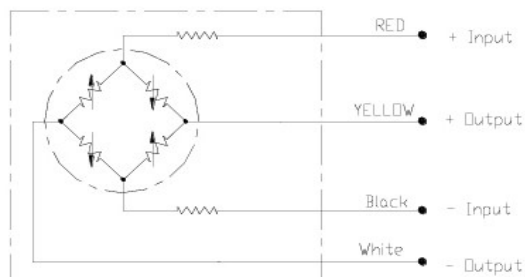
# FC22 Compression Load Cell

## DIMENSIONS

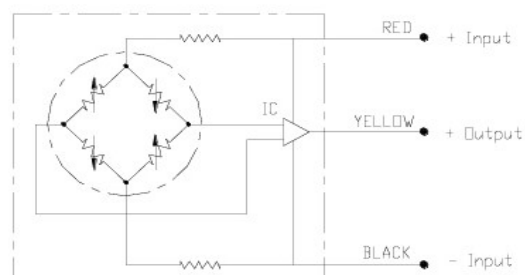


## CONNECTIONS

Millivolt Bridge Version



High Level Amplified Output



## FC22 Compression Load Cell

### ORDERING INFORMATION

FC22	3	-	1	0000	-	0010	-	L
<b>Model</b>	<b>Output</b>	<b>-</b>	<b>Connection</b>	<b>Specials</b>	<b>-</b>	<b>Force Range (lbf)</b>	<b>Multiplier</b>	<b>Units</b>
<b>FC22</b>	0 = Uncompensated 1 = 20mV 3 = 0.5 – 4.5V	<b>-</b>	1 = 2ft Cable	0000	<b>-</b>	<b>0010</b> <b>0025</b> <b>0050</b> <b>0100</b>	- = None	L = lbf

#### NORTH AMERICA

Measurement Specialties  
45738 Northport Loop West  
Fremont, CA 94538  
Tel: 1-800-767-1888  
Fax: 1-510-498-1578  
Sales: [pfg.cs.amer@meas-spec.com](mailto:pfg.cs.amer@meas-spec.com)

#### EUROPE

Measurement Specialties  
(Europe), Ltd.  
26 Rue des Dames  
78340 Les Clayes-sous-Bois, France  
Tel: +33 (0) 130 79 33 00  
Fax: +33 (0) 134 81 03 59  
Sales: [pfg.cs.emea@meas-spec.com](mailto:pfg.cs.emea@meas-spec.com)

#### ASIA

Measurement Specialties  
(China), Ltd.  
No. 26 Langshan Road  
Shenzhen High-Tech Park (North)  
Nanshan District, Shenzhen 518057  
China  
Tel: +86 755 3330 5088  
Fax: +86 755 3330 5099  
Sales: [pfg.cs.asia@meas-spec.com](mailto:pfg.cs.asia@meas-spec.com)

The information in this sheet has been carefully reviewed and is believed to be accurate; however, no responsibility is assumed for inaccuracies. Furthermore, this information does not convey to the purchaser of such devices any license under the patent rights to the manufacturer. Measurement Specialties, Inc. reserves the right to make changes without further notice to any product herein. Measurement Specialties, Inc. makes no warranty, representation or guarantee regarding the suitability of its product for any particular purpose, nor does Measurement Specialties, Inc. assume any liability arising out of the application or use of any product or circuit and specifically disclaims any and all liability, including without limitation consequential or incidental damages. Typical parameters can and do vary in different applications. All operating parameters must be validated for each customer application by customer's technical experts. Measurement Specialties, Inc. does not convey any license under its patent rights nor the rights of others.

### Heavy Duty Pressure Transducers

MLH Series, 6 bar to 550 bar | 50 psi to 8000 psi

008118

Issue 8

Datasheet



#### DESCRIPTION

The MLH Series Heavy Duty Pressure Transducers combine Application Specific Integrated Circuit (ASIC) technology with a media-isolated, metal diaphragm design. This digitally compensated transducer offers value and performance, making it a suitable pressure sensing solution for demanding applications. Fully temperature compensated, calibrated and amplified, the MLH Series is available in pressure ranges of 6 bar to 550 bar | 50 psi to 8,000 psi. The MLH Series provides  $\pm 0.25\%$  full scale accuracy Best Fit Straight Line (BFSL) and a TEB (Total Error Band) as low as 2% over a temperature range of  $-40\text{ }^{\circ}\text{C}$  to  $125\text{ }^{\circ}\text{C}$  [ $-40\text{ }^{\circ}\text{F}$  to  $257\text{ }^{\circ}\text{F}$ ]. Industry standard electrical connectors and pressure ports are offered for enhanced reliability and user flexibility.

The MLH Series has six standard output options:

- A. 0.5 Vdc to 4.5 Vdc ratiometric from 5 Vdc excitation
- B. 4 mA to 20 mA
- C. 1 Vdc to 6 Vdc regulated
- D. 0.25 Vdc to 10.25 Vdc regulated
- E. 0.5 Vdc to 4.5 Vdc regulated
- G. 1 Vdc to 5 Vdc regulated

#### FEATURES

- All metal wetted parts allow for potential use in wide variety of fluid applications
- No internal elastomeric seals mean no O-ring compatibility issues
- Amplified outputs reduce the need to purchase external amplifiers
- Input reverse voltage protection guards against mis-wiring
- Less than 2 ms response time provides more accurate, high speed measurement
- Rated IP65 or better for protection from most harsh environments

#### POTENTIAL APPLICATIONS

- Industrial: Compressors, cylinder tank pressure, HVAC, hydraulics, oil and gas, refrigeration, water distribution
- Transportation: Multiple applications including braking and alternative fuels
- Medical: Anesthesia delivery machines, blood analyzers, chemistry analyzers, gas chromatography, oxygen concentrators, and ventilators

#### PORTFOLIO

The MLH Series joins the PX3 Series, PX2 Series, SPT Series, 13 mm Series and 19 mm Series heavy duty pressure transducers.

# Heavy Duty Pressure Transducers

MLH Series, 6 bar to 550 bar | 50 psi to 8000 psi

**Table 1. Pressure Range Specifications<sup>1</sup> (At 25 °C [77 °F] and at rated excitation unless otherwise specified.)**

bar			psi		
Operating Pressure	Proof Pressure	Burst Pressure	Operating Pressure	Proof Pressure	Burst Pressure
6	18	60	50	150	500
10	30	100	100	300	1000
16	48	160	150	450	1500
25	75	250	200	600	2000
40	80	400	250	750	2500
60	120	600	300	900	3000
100	200	1000	500	1500	5000
160	320	1600	1000	2000	10000
250	500	2068	2000	4000	20000
350	700	2068	3000	6000	30000
500	750	2068	5000	7500	30000
550	825	2068	8000	12000	30000

<sup>1</sup> Comparable metric units follow same proof and burst specifications.

**Table 2. Electrical Specifications**

Characteristic	Output Signal					
	Ratiometric (A)	Current (B)	Regulated (C)	Regulated (D)	Regulated (E)	Regulated (G)
Zero output	0.5 Vdc	4 mA	1 Vdc	0.25 Vdc	0.5 Vdc	1 Vdc
Full scale span (FSS)	4 Vdc (0.5 Vdc to 4.5 Vdc)	16 mA (4 mA to 20 mA)	5 Vdc (1 Vdc to 6 Vdc)	10 Vdc (0.25 Vdc to 10.25 Vdc)	4 Vdc (0.5 Vdc to 4.5 Vdc)	4 Vdc (1 Vdc to 5 Vdc)
Excitation	5 Vdc (6 Vdc max.) <sup>1</sup>	9.5 Vdc to 30 Vdc <sup>2</sup>	8 Vdc to 30 Vdc <sup>2</sup>	14 Vdc to 30 Vdc <sup>2</sup>	7 Vdc to 30 Vdc <sup>2</sup>	8 Vdc to 30 Vdc <sup>2</sup>
Supply current	4 mA typ., 8 mA max.	N/A	5 mA typ., 17 mA max.	5 mA typ., 17 mA max.	5 mA typ., 17 mA max.	5 mA typ., 17 mA max.
Source (nominal)	1 mA	N/A	1 mA	1 mA	1 mA	1 mA
Sink (nominal)	1 mA at zero output	N/A	1 mA at zero output	1 mA at zero output	1 mA at zero output	1 mA at zero output
Supply rejection ratio	90 dB	90 dB	90 dB	90 dB	90 dB	90 dB
Output impedance	25 Ohm max.	N/A	25 Ohm max.	25 Ohm max.	25 Ohm max.	25 Ohm max.

<sup>1</sup> Maintains ratiometricity at 5 ± 0.25 Vdc excitation. Product can tolerate 6 Vdc excitation without damage.

<sup>2</sup> See Figures 1 and 2 for more information regarding maximum excitation voltage vs. operating temperature.



# Heavy Duty Pressure Transducers

MLH Series, 6 bar to 550 bar | 50 psi to 8000 psi

**Table 3. Environmental and Mechanical Specifications**

Characteristic	Parameter
Material in contact with media: port diaphragm	stainless steel 304L Haynes 214 alloy
Housing material	black plastic – Amodel AS-4133 HS – PPA
Weight (typical for Metri-Pack 150 and 1/8 NPT pressure port types)	57.0 g [2.0 oz]
Shock	100 g peak [11 ms]
Vibration	MIL-STD-810C, Figure 514.2-5, Curve AK, Table 514.2-V, Random Vibration Test (overall g rms = 20.7 min.)
Compensated and operating temperature range: 0.5 Vdc to 4.5 Vdc ratiometric output all regulated and 4 mA to 20 mA outputs	-40 °C to 125 °C [-40 °F to 257 °F] -40 °C to 125 °C [-40 °F to 257 °F] (See Figures 1 and 2 for operating area details.)
Storage temperature range	-40 °C to 125 °C [-40 °F to 257 °F]
Approvals	RoHS, CE, UL Component Recognition for USA and Canada: File No. E258956

**Table 4. Performance Specifications (At 25 °C [77 °F] and under unless otherwise noted.)**

Characteristic	Parameter
Response time	<2 ms
Accuracy <sup>1</sup> : ≥100 psi ≤100 psi	±0.25 %FSS ±0.50 %FSS
Total Error Band <sup>2</sup> :	
Gage:	
<300 psig	±3 %FSS
≥300 psig	±2 %FSS
Sealed gage:	
≥300 psis	±2 %FSS
<u>without L, M, P</u> electrical connector types:	
100 psis to 299 psis (-40 °C to 85 °C [-40 °F to 185 °F])	±3 %FSS
100 psis to 299 psis (>85 °C to 125 °C [>185 °F to 257 °F])	±10 %FSS
≥300 psis (-40 °C to 125 °C [-40 °F to 257 °F])	±2 %FSS
<u>with L, M, P</u> electrical connector types:	
100 psis to 299 psis (-40 °C to 65 °C [-40 °F to 149 °F])	±10 %FSS
100 psis to 299 psis (>65 °C to 125 °C [>149 °F to 257 °F])	±15 %FSS
≥300 psis (-40 °C to 65 °C [-40 °F to 149 °F])	±5 %FSS
≥300 psis (>65 °C to 125 °C [>149 °F to 257 °F])	±15 %FSS

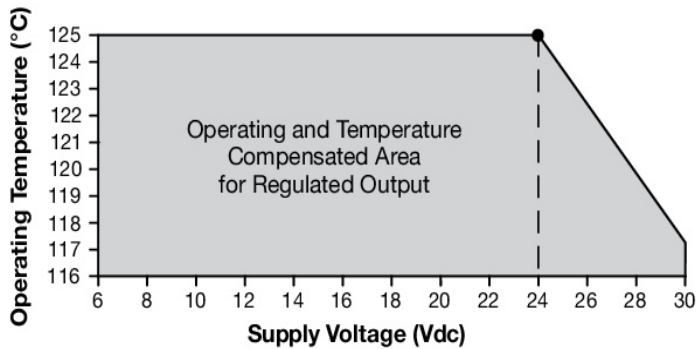
<sup>1</sup> Includes pressure non-linearity (BFSL), pressure hysteresis and non-repeatability. Thermal errors are not included.

<sup>2</sup> Includes zero error, span error, thermal effect on zero, thermal effect on span, thermal hysteresis, pressure-non-linearity, pressure hysteresis and non-repeatability.

# Heavy Duty Pressure Transducers

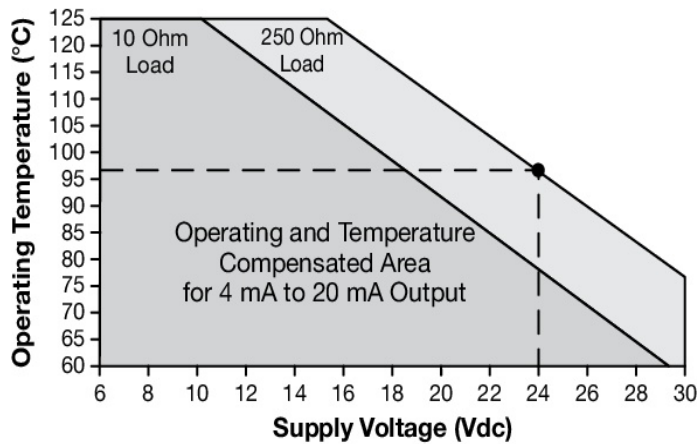
MLH Series, 6 bar to 550 bar | 50 psi to 8000 psi

Figure 1. Operating and Temperature Compensation for All Regulated Output Options



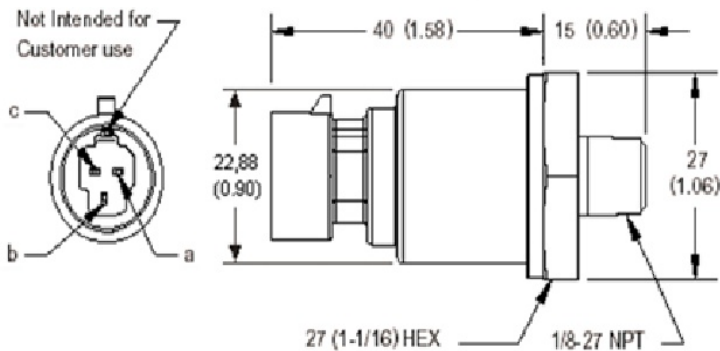
Note: Dot indicates the maximum operating temperature of 125 °C [257 °F] with a 24 V supply.

Figure 2. Operating and Temperature Compensation for 4 mA to 20 mA Output



Note: The operating area is extended with a 250 Ohm resistor. Higher loads extend the operating area. Dot indicates the maximum operating temperature when using a 24 V supply and a 250 Ohm resistor.

Figure 3. Example Mounting Dimensions (Electrical Termination "B" Shown. For reference only. mm/(in.))



### Pin/Wire Colors

Pin	Voltage	Current
a	+ excitation	+ excitation
b	output	- excitation
c	common	no connection

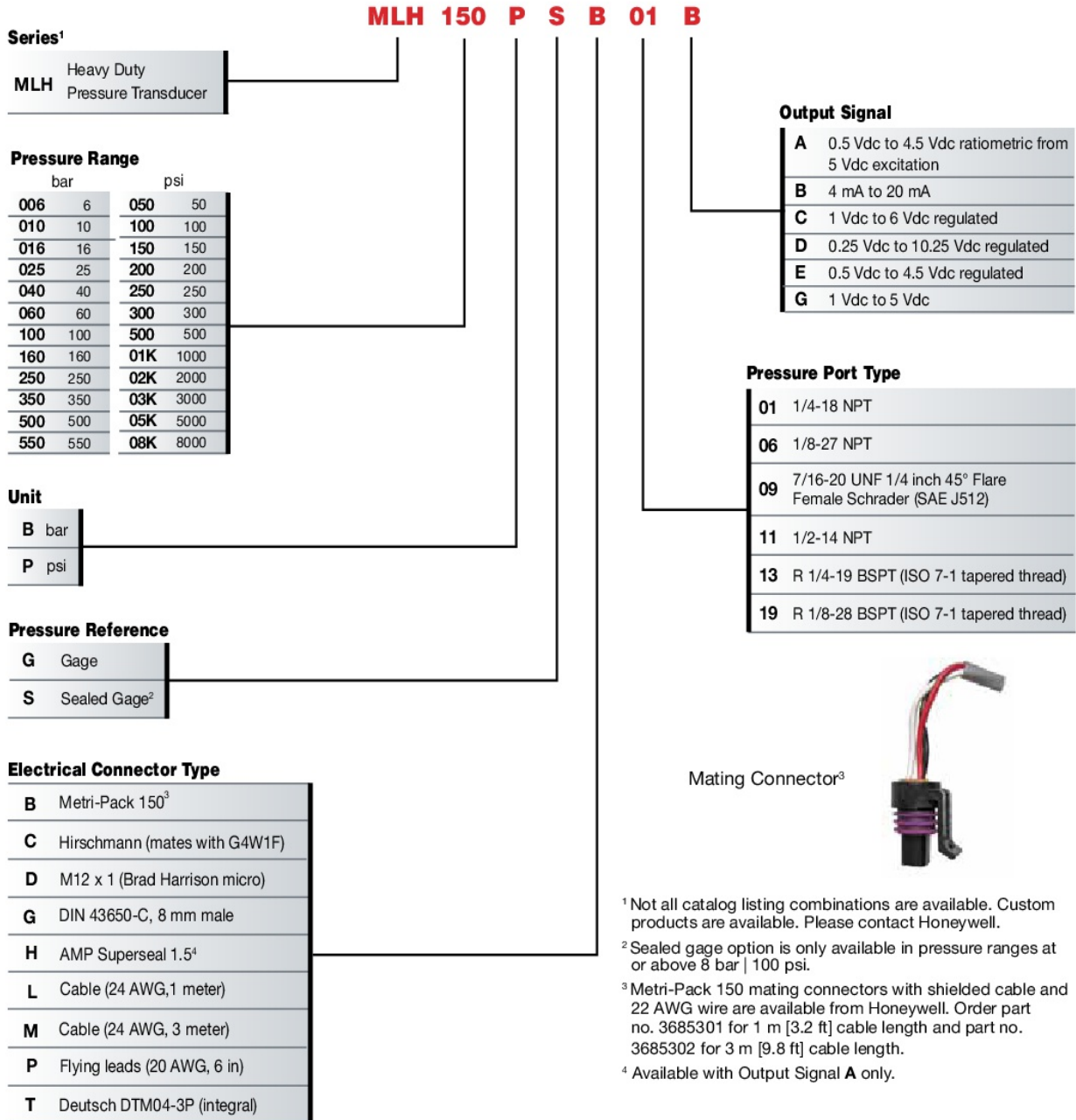
A variety of pressure ports and electrical termination connection options are available. Refer to the Figure 4 for possible combinations. Contact your Honeywell representative for details.

# Heavy Duty Pressure Transducers

MLH Series, 6 bar to 550 bar | 50 psi to 8000 psi

Figure 4. Nomenclature and Order Guide

For example, **MLH150PSB01B** defines an MLH Series Heavy Duty Pressure Transducer, 150 psi pressure range, sealed gage pressure reference, Metri-Pack 150 electrical connector type, 1/4-18 NPT pressure port type, 4 mA to 20 mA output.



<sup>1</sup> Not all catalog listing combinations are available. Custom products are available. Please contact Honeywell.

<sup>2</sup> Sealed gage option is only available in pressure ranges at or above 8 bar | 100 psi.

<sup>3</sup> Metri-Pack 150 mating connectors with shielded cable and 22 AWG wire are available from Honeywell. Order part no. 3685301 for 1 m [3.2 ft] cable length and part no. 3685302 for 3 m [9.8 ft] cable length.

<sup>4</sup> Available with Output Signal **A** only.



#### ADDITIONAL INFORMATION

The following associated literature is available on the Honeywell web site at [sensing.honeywell.com](http://sensing.honeywell.com):

- Product line guide
- Product range guide
- Product installation instructions

#### **⚠ WARNING** **PERSONAL INJURY**

DO NOT USE these products as safety or emergency stop devices or in any other application where failure of the product could result in personal injury.

**Failure to comply with these instructions could result in death or serious injury.**

#### **⚠ WARNING** **MISUSE OF DOCUMENTATION**

- The information presented in this datasheet is for reference only. Do not use this document as a product installation guide.
- Complete installation, operation, and maintenance information is provided in the instructions supplied with each product.

**Failure to comply with these instructions could result in death or serious injury.**

#### **Warranty/Remedy**

Honeywell warrants goods of its manufacture as being free of defective materials and faulty workmanship during the applicable warranty period. Honeywell's standard product warranty applies unless agreed to otherwise by Honeywell in writing; please refer to your order acknowledgement or consult your local sales office for specific warranty details. If warranted goods are returned to Honeywell during the period of coverage, Honeywell will repair or replace, at its option, without charge those items that Honeywell, in its sole discretion, finds defective. **The foregoing is buyer's sole remedy and is in lieu of all other warranties, expressed or implied, including those of merchantability and fitness for a particular purpose. In no event shall Honeywell be liable for consequential, special, or indirect damages.**

While Honeywell may provide application assistance personally, through our literature and the Honeywell web site, it is buyer's sole responsibility to determine the suitability of the product in the application.

Specifications may change without notice. The information we supply is believed to be accurate and reliable as of this writing. However, Honeywell assumes no responsibility for its use.

#### **For more information**

To learn more about Honeywell's sensing and switching products, call 1.800.537.6945, visit [sensing.honeywell.com](http://sensing.honeywell.com), or e-mail inquiries to [info.sc@honeywell.com](mailto:info.sc@honeywell.com)

#### **Honeywell Safety and Productivity Solutions**

9680 Old Bailes Road  
Fort Mill, SC 29707  
[www.honeywell.com](http://www.honeywell.com)

008118-8-EN IL50  
October 2016  
© 2016 Honeywell International Inc. All rights reserved.

# Honeywell

## Installation Instructions for the MLH Series Pressure Sensors

ISSUE 2  
50010132

### **WARNING**

#### **PERSONAL INJURY**

DO NOT USE these products as safety or emergency stop devices or in any other application where failure of the product could result in personal injury.

**Failure to comply with these instructions could result in death or serious injury.**

### **GENERAL INFORMATION**

Sensors with pressure ranges less than 300 psi are vented to the atmosphere through a case vent hole that is protected with a vapor inhibiting material.

### **PRESSURE OVERLOADS**

#### **CAUTION**

##### **PRODUCT DAMAGE**

- Do not exceed the pressure overload rating.

**Failure to comply with these instructions may result in reduced life, or electrical failure.**

The MLH Series pressure sensors will withstand high overloads; however, if the overload rating is exceeded, the life of the MLH Series may be reduced and electrical failure may occur. Both static and dynamic overloads must be considered, particularly in hydraulic system applications. Hydraulic pressure fluctuations can have very high and very fast peak pressures, as in a water hammer effect.

An oscilloscope is recommended for determining if high-pressure transients exist in a system. If system pressure pulses are expected, choose a sensor with a pressure rating high enough to allow continuous operation at the highest expected pressure spikes.

A pressure 'snubber' may be used to reduce the peak pressure applied to the sensor. Snubbers may be obtained from the Mott Corp., Farmington, CT, USA (860) 747-6333. Catalog #4100-1/8-SS is recommended.

### **MEDIA COMPATIBILITY**

#### **CAUTION**

##### **PRODUCT DAMAGE**

- Use non-abrasive, chemically compatible media to prevent damage to diaphragm or port materials.

**Failure to comply with these instructions may result in product failure.**

The MLH Series pressure port and diaphragm is an assembly of Haynes 214 alloy (or equivalent) and 304 stainless steel.

### **INSTALLATION**

#### **CAUTION**

##### **PRODUCT DAMAGE**

- Use a hex wrench for installation. Never apply torque to the connector housing or the body of the sensor.
- Do not subject the sensor to high temperatures from soldering, brazing, or welding of the system plumbing or operating environments above the specified maximum temperature.

**Failure to comply with these instructions may result in product damage.**

Ratiometric voltage and mV output devices require a regulated 5.0 Vdc supply. All other versions can use an unregulated supply within the ranges noted under the excitation specifications. The power supply should be off while wiring.

### **ELECTROMAGNETIC ENERGY/NOISE**

#### **CAUTION**

##### **PRODUCT DAMAGE/ERRATIC OPERATION**

- Do not use in areas where electromagnetic energy may affect sensor operation.

**Failure to comply with these instructions may result in improper operation and/or product failure.**

The MLH Series has been rated for high immunity to electrical noise; however, care should be taken when used around high voltage sources that emit high levels of radiated electromagnetic energy like variable frequency motor drives, solenoids, radio transmitters and engine ignition systems. The use of shielded cable and grounding of pressure port is also recommended.

### **BENCH TEST**

For incoming inspection or sensor failure evaluation, connect the sensor to a dc voltage supply (off). The supply voltage should be set within the range specified for the model. Based on the sensors specified output, connect the output lead(s) to a digital dc or mA meter. With no pressure on the sensor, turn on the power supply and read the output signal on the voltmeter. The reading should correspond to the specification indicated for null offset. If not, check the connections, wire color code and the setting of the power supply.

### **WIRING INSTRUCTIONS**

The wiring code for electrical connection is shown in Tables 2 and 3.

When using a connector, the use of the correct size wire is important to ensure environmental sealing. Fill all holes in the connector seal even if only two leads are used. Honeywell recommends using a crimping tool for crimping wires to the connector pins. Contact the individual connector manufacturer for mating connector wiring.

**TABLE 1. SPECIFICATIONS**

Parameter	Excitation	Signal Output
Ratiometric	5.0 Vdc ±0.25 Vdc	0.5 Vdc to 4.5 Vdc
Regulated	7.0 Vdc to 35 Vdc	0.5 Vdc to 4.5 Vdc
	8.0 Vdc to 35 Vdc	1.0 Vdc to 6.0 Vdc
	14.0 Vdc to 35 Vdc	0.25 Vdc to 10.25 Vdc
	7.0 Vdc to 30 Vdc	1 Vdc to 5 Vdc
Unamplified output	5.0 Vdc	0 mV to 50 mV
Current output	9.5 Vdc to 35 Vdc	4 mA to 20 mA with 25 Vdc excitation
Compensated operating and storage temperature	-40 °C to 125 °C [-40 °F to 257 °F]	
Weight	57 g [2 oz]	

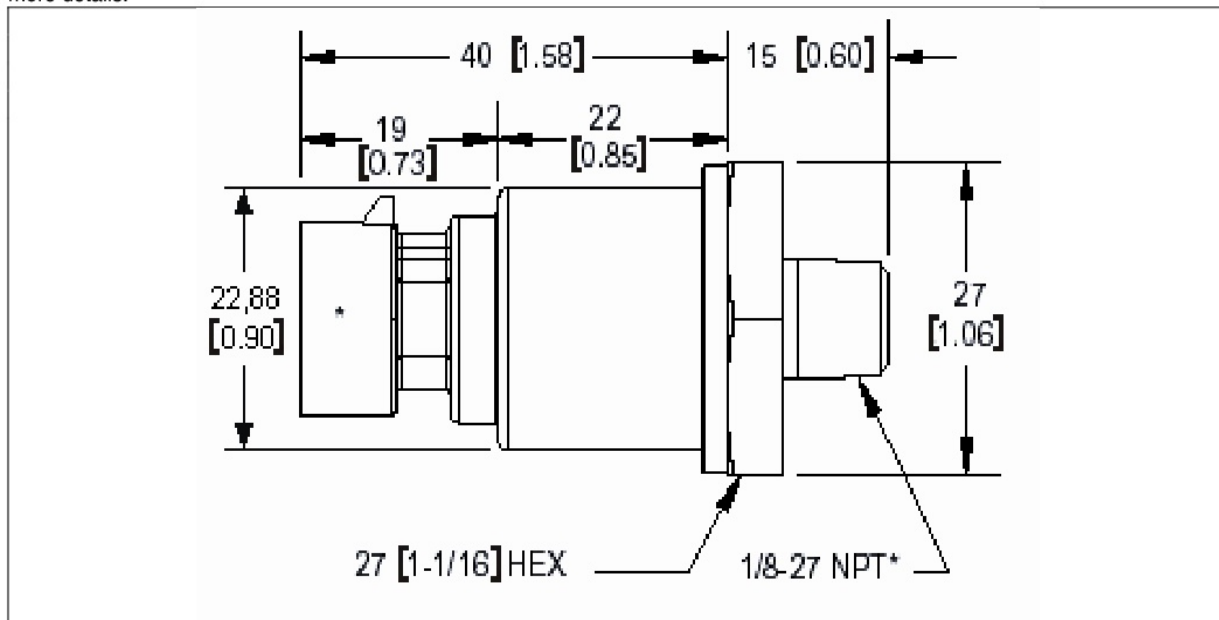
**TABLE 2. PRESSURE RANGES**

Units	psiG	psiG	psiG	psiG	psiG	psiS	psiS	psiS	psiS	psiS	psiS	psiS
Pressure	50	100	150	200	250	300	500	1000	2000	3000	5000	8000
Proof pressure	150	300	450	600	750	900	1500	2000	4000	6000	7500	12000
Burst pressure	500	1000	1500	2000	2500	3000	5000	10000	20000	30000	30000	30000

Units	barG	barG	barG	barS	barS	barS	barS	barS	barS	barS	barS	barS
Pressure	6	10	16	25	40	60	100	160	250	350	500	550
Proof pressure	18	30	48	75	80	120	200	320	500	700	750	825
Burst pressure	60	100	160	250	400	600	1000	1600	2068	2068	2068	2068

**FIGURE 1. MOUNTING DIMENSIONS (For reference only. mm [in.]**




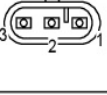

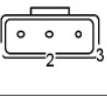
A variety of pressure port and electrical termination connection options is available. Contact your Honeywell representative for more details.





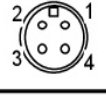
# MLH Series Pressure Sensors

Issue 2 50010132

**TABLE 3. VOLTAGE AND CURRENT OUTPUT MODELS WITH PIN ASSIGNMENTS**

Data Sheet Code	Connector Name	Sensor Back View	VOLTAGE OUTPUT (3-WIRE) MODELS				CURRENT OUTPUT (2-WIRE) MODELS			
			Pin Assignments				Pin Assignments			
			A	B	C	D	A	B	C	D
			1	2	3	4	1	2	3	4
B	Packard Metripack		+ Excitation	Output	Common	—	+ Excitation	- Excitation (return)	N/C	
C	Hirschmann G4W		N/C	Output	Common	+ Excitation	N/C	N/C	- Excitation (return)	+ Excitation
G	Din 43650 form C		+ Excitation	Common	N/C	Output	+ Excitation	- Excitation (return)	N/C	N/C
H	AMP 1.4 Superseal		Common	Output	+ Excitation	—	N/C	- Excitation (return)	+ Excitation	—
L, M or P	Cable Lead	Red = A White = B Black = C	+ Excitation	Output	Common	—	+ Excitation	- Excitation (return)	N/C	—
D	M12-1 Brad Harrison		+ Excitation	Common	Output	N/C	+ Excitation	- Excitation (return)	N/C	N/C
T	Deutsch DTM04-3P		+ Excitation	Common	Output	—	+ Excitation	- Excitation (return)	N/C	—

**TABLE 4. MILLIVOLT OUTPUT MODELS WITH PIN ASSIGNMENTS**

Data Sheet Code	Connector Name	Sensor Back View	(4-WIRE) MODELS			
			Pin Assignments			
			A	B	C	D
			1	2	3	4
C	Hirschmann G4W		+ Signal	- Excitation	- Signal	+ Excitation
G	Din 43650 form C		+ Excitation	- Signal	+ Signal	- Excitation
L, M or P	Cable Lead	Red = A Green = B Black = C White = D	+ Excitation	+ Output	Common	- Output
D	M12-1 Brad Harrison		+ Signal	- Excitation	- Signal	+ Excitation

# MLH Series Pressure Sensors

Issue 2 50010132

## WARRANTY/REMEDY

Honeywell warrants goods of its manufacture as being free of defective materials and faulty workmanship. Honeywell's standard product warranty applies unless agreed to otherwise by Honeywell in writing; please refer to your order acknowledgement or consult your local sales office for specific warranty details. If warranted goods are returned to Honeywell during the period of coverage, Honeywell will repair or replace, at its option, without charge those items it finds defective. **The foregoing is buyer's sole remedy and is in lieu of all other warranties, expressed or implied, including those of merchantability and fitness for a particular purpose. In no event shall Honeywell be liable for consequential, special, or indirect damages.**

While we provide application assistance personally, through our literature and the Honeywell web site, it is up to the customer to determine the suitability of the product in the application.

Specifications may change without notice. The information we supply is believed to be accurate and reliable as of this printing. However, we assume no responsibility for its use.

## SALES AND SERVICE

Honeywell serves its customers through a worldwide network of sales offices, representatives and distributors. For application assistance, current specifications, pricing or name of the nearest Authorized Distributor, contact your local sales office or:

**E-mail:** [info.sc@honeywell.com](mailto:info.sc@honeywell.com)

**Internet:** [www.honeywell.com/sensing](http://www.honeywell.com/sensing)

### Phone and Fax:

Asia Pacific	+65 6355-2828
	+65 6445-3033 Fax
Europe	+44 (0) 1698 481481
	+44 (0) 1698 481676 Fax
Latin America	+1-305-805-8188
	+1-305-883-8257 Fax
USA/Canada	+1-800-537-6945
	+1-815-235-6847
	+1-815-235-6545 Fax

## Automation and Control Solutions

Sensing and Control

Honeywell

1985 Douglas Drive North

Minneapolis, MN 55422

[www.honeywell.com/sensing](http://www.honeywell.com/sensing)

50010132-2-EN IL50 GLO Printed in USA  
October 2006  
Copyright © 2006 Honeywell International Inc. All rights reserved.

# Honeywell